

Wetting and Surface Freezing Transitions at the
Liquid-Vapour Interface of Ga-based Alloys:
STM, XPS and AES Study.

Zur Erlangung des akademischen Grades eines
DOKTORS DER NATURWISSENSCHAFTEN

(Dr. rer. nat.)

der Fakultät für Chemie und Biowissenschaften der
Universität Karlsruhe (TH)
angenommene

DISSERTATION

von

Dipl.-Chem. Alexander Issanin
aus St. Petersburg, Russische Föderation

Dekan: Prof. Dr. H. Puchta
Referent: Prof. Dr. W. Freyland
Korreferent: PD Dr. P. Weiss
Tag der mündlichen Prüfung: 17.07.2006

Content

List of acronyms

Abstract	1
Zusammenfassung	3
1. Introduction	5
2. Interfacial phenomena	9
2.1 Wetting transition	9
2.2 Surface freezing transition	12
3. Applied methods	17
3.1 Electron spectroscopy	17
3.1.1 Basic principles of XPS, AES and UPS	17
3.1.2 Radiation sources and electron detection in electron spectroscopy	20
3.1.3 Quantification with XPS and AES	24
3.1.4 Depth profiling	29
3.2 Scanning tunneling microscopy	32
3.2.1 Theoretical concept	32
3.2.2 Measurement modes	34
4. Experimental detail, data analysis and error discussion	37
4.1 Preparation of samples; measurement cell	37
4.2 Overview of the Omicron UHV unit including XPS, AES, UPS and STM techniques	42
4.3 Electron spectra measurements	45
4.4 STM image acquisition	47
4.5 Error analysis	50

5. Results	53
5.1 Wetting films in Ga-Bi and Ga-Pb systems	53
5.1.1 Ga-Bi	53
5.1.2 Ga-Pb	58
5.2 Surface freezing films in the Ga-Bi system	61
5.2.1 Homogeneity of the SF films – results from AES	61
5.2.2 Thickness of the SF films	64
5.2.3 Surface topography of the strongly undercooled films	69
5.3 Surface freezing films in the Ga-Pb system	71
5.3.1 Thickness and homogeneity of SF films in the Ga-Pb system	71
5.3.2 Evolution of the SF films in Ga-Pb system	73
5.3.3 Surface topography of the strongly undercooled films	75
5.4 Tip-induced surface modification and nanostructuring	76
6. Discussion	81
6.1 Modelling of thickness, coverage and chemical composition for the surface freezing films in the Ga-Pb system	81
6.1.1. Surface freezing films without defects	81
6.1.2 Surface freezing films with defects in the Ga-Pb system	89
6.2 Mechanism of the tip-induced nanostructuring	94
Appendix A	97
Appendix B	104
Manufacturer list	105
References	106
Acknowledgements	112

List of acronyms in alphabetical order

AES	-	Auger Electron Spectroscopy
BE	-	Binding Energy
CAE	-	Constant Analyzer Energy (mode)
CCD	-	Charge-Coupled Device
CRR	-	Constant Retard Ration (mode)
DC	-	Direct Current
EA	-	Electron Energy Analyzer
ES	-	Electron Spectroscopy
FEL	-	Fast Entry Lock
HSA	-	HemiSpherical electron energy Analyzer
IMFP	-	Inelastic Mean Free Path
(k)cts/s		(kilo)counts per second
KE	-	Kinetic Energy
ML	-	MonoLayer
SF	-	Surface Freezing
SFF	-	Surface Freezing Film
SHG	-	Second Harmonic Generation
STM	-	Scanning Tunneling Microscopy
STS	-	Scanning Tunneling Spectroscopy
UHV	-	Ultra High Vacuum ($< 10^{-9}$ mbar)
UPS	-	Ultraviolet Photoelectron Spectroscopy
WF	-	Wetting Film
XPS	-	X-ray Photoelectron Spectroscopy

Abstract

The main focus of this study is to investigate the interfacial behaviour in liquid Ga-Bi and Ga-Pb alloys in a wide temperature range. For this purpose methods of X-ray photoelectron spectroscopy (XPS), Auger electron spectroscopy (AES) and scanning tunnelling microscopy (STM) were mainly utilized. The systems under consideration can be characterized by an ultra-thin wetting film for temperatures above the surface freezing point. In general, a surface active component, which has a lower value of the surface tension, segregates at the liquid-vapour interface and thus decreases the overall surface energy of the system. The quantitative characterization of this phenomenon is essential from both a theoretical and experimental point of view. The dependences of the wetting film thickness on temperature and bulk concentration of the surface active component have been studied. The results are in good agreement with model calculations, which predict the increase of the wetting film thickness with decreasing temperature.

A surface phase transition characterized by the formation of a surface freezing (SF) film was studied in both Ga-Bi and Ga-Pb systems. Samples with different concentrations of the surface active component between eutectic and monotectic points were investigated. The formation of the SF films on cooling was systematically observed at temperatures above the corresponding temperature of the bulk liquidus line, according to the bulk phase diagram. Thickness and homogeneity of the SF films were investigated in detail. The behaviour of the SF films in the Ga-Bi and Ga-Pb systems has been found to be similar, showing however some differences. The distinguishable features comprise the stability of the films after formation and the magnitude of the Ga signal in the XPS spectra. The latter feature i.e. the higher intensity of the Ga peak for the Ga-Pb system can be interpreted either as a smaller thickness of the corresponding SF films, or as higher concentration of Ga in the film. Overlayer (or slab) models with constant or variable composition of the film were applied for the quantitative interpretation of the results from the electron spectroscopy. Assuming a homogeneous film of pure Pb a thickness of the SF film in Ga-Pb system of ~ 20 Å is estimated for temperatures slightly below the surface freezing temperature. In the case of Ga-Bi this thickness seems to be above 100 Å.

For the first time the instability of the SF films in Ga-Pb systems was observed at constant temperature and at slow (< 3 K/h) cooling rates. The formation of the islands of

the liquid phase and other defects was detected with a CCD-camera. When islands form a further increase of the Ga-signal in the XPS spectra is observed. For a quantitative description of the system with defects a modification of the overlayer model is proposed, which takes into account an incomplete coverage of the surface with a SF film.

Additional information about the atomic structure of the films quenched to room temperature was obtained from STM measurements. These measurements reveal extraordinary large, atomically flat terraces, which were found to be much larger in comparison to those typically found in pure materials (Bi and Pb). An analysis of the interatomic distances from the STM images with atomic resolution demonstrates that the utmost surface layers consists of the pure surface active component with a basal trigonal plane (0001) in the case of Bi and a hexagonally orientated (111) plane for Pb.

Zusammenfassung

Hauptzielsetzung dieser Arbeit war, die Grenzflächeneigenschaften von flüssigen Ga-Bi und Ga-Pb Legierungen in einem breiten Temperaturintervall aufzuklären. Hierzu wurden die Methoden der Röntgen-Photoelektronen Spektroskopie (XPS), Auger-Elektronen Spektroskopie (AES) sowie Rastertunnelmikroskopie (STM) eingesetzt. Die gemeinsame charakteristische Eigenschaft von den untersuchten Systemen ist die Bildung von ultradünnen Benetzungsfilmen bei Temperaturen oberhalb des Oberflächenerstarrungspunktes. Dabei gilt allgemein, dass die Komponente mit kleiner Oberflächenspannung sich an der flüssig-dampf Grenzfläche konzentriert, so dass die totale Oberflächenenergie des Systems abgesenkt wird. Die quantitative Charakterisierung dieses Phänomens ist wichtig sowohl vom theoretischen Standpunkt als auch für den Experimentator. Die Abhängigkeit der Dicke der Benetzungsfilme von Temperatur und Konzentration der oberflächenaktiven Komponente im Volumen wurde bei Annäherung an die Liquiduskurve untersucht. Die Ergebnisse stimmen mit Modellrechnungen überein, die einen leichten Anstieg der Filmdicke mit abnehmender Temperatur voraussagen.

Die Bildung von Oberflächenerstarrungsfilmen wurde in beiden Systemen, Ga-Bi und Ga-Pb, analysiert, wobei die untersuchten Konzentrationen den Bereich zwischen den eutektischen und den monotektischen Zusammensetzungen abdecken. Die Abweichung der Oberflächenerstarrungstemperatur von der entsprechenden Liquidustemperatur, die aus den Phasendiagrammen entnommen wurde, kann systematisch nachgewiesen werden. Dicke und Homogenität der Filme wurden ausführlich erforscht. Das Verhalten der Filme in Ga-Bi und Ga-Pb Systemen wurde als ähnlich charakterisiert, jedoch wurden einige quantitative Differenzen beobachtet. Die Unterschiede liegen vor allem in der Stabilität der Filme und in der Größe des Ga-Signals im XPS Spektrum. Die höhere Intensität des Ga-Peaks in Ga-Pb kann entweder als kleinere Dicke des entsprechenden Oberflächenerstarrungsfilmes oder als höhere Ga Konzentration im Film interpretiert werden. Schichtmodelle mit konstanter oder variabler Filmzusammensetzung wurden für die quantitative Darstellung der Ergebnisse aus der Elektronen Spektroskopie verwendet. Unter den Annahmen, dass der Film homogen ist und aus reinem Pb besteht, wird ein Wert von $\sim 20 \text{ \AA}$ für die Dicke des erstarrten Filmes in der unmittelbaren Nähe unterhalb

des Oberflächenerstarrungspunktes gefunden. In Ga-Bi dagegen scheinen die Filme mehr als 100 Å dick zu sein.

Zum ersten Mal wurde eine Instabilität der erstarrten Filme in Ga-Pb beobachtet. Dies geschieht, wenn die flüssigen Legierungen bei konstanter Temperatur gehalten oder langsam (< 3 K/Stunde) abgekühlt werden. Die Bildung von Inseln und anderen Defekten, die aus der flüssigen Phase bestehen, wurden mithilfe einer CCD-Kamera aufgezeichnet. Solche Transformationen führen zum Anstieg des Ga-Signals im XPS Spektrum. Für die quantitative Beschreibung der Oberfläche mit Inseln wurde das Schichtmodell modifiziert, um die nicht vollständige Bedeckung der Oberfläche zu berücksichtigen.

Zusätzliche Information über die atomare Struktur der festen Filme, die bis Raumtemperatur abgekühlt worden sind, konnte mit STM Messungen gewonnen werden. Diese Experimente zeigten, dass die Oberfläche aus sehr großen und atomar flachen Terrassen besteht, die viel größer sind als die, die man üblicherweise in reinen Metallen (Bi und Pb) erhält. Die Analyse der STM-Bilder mit atomarer Auflösung weist darauf hin, dass die äußersten Grenzschichten aus reinem Bi (basale trigonale (0001)-Orientierung) oder Pb (hexagonale (111)-Orientierung) bestehen.

Chapter 1.

1. Introduction

Surfaces and interfaces start to play a crucial role when dimensions of the objects under consideration are decreased. The availability of the methods and instruments which can cope with objects on the nanometre scale gives rise for such disciplines as nanoscience and nanotechnology. The number of publications in this field has dramatically increased in the last 15 years [1, 2]. Some fundamental problems such as phase formation and phase transition in reduced dimensions (2D) are not completely studied as yet. Both experimental and theoretical efforts help to understand these phenomena in details.

The phenomena of surface melting [3, 4] and roughening phase transitions, both of which are characterized by the suppression of long-range order interactions near the free interface, are common meanwhile. In this case the surface phase is less ordered than the bulk phase. This phenomenon has been studied for a variety of metals and molecular crystals [5-7]. In particular it has been studied thoroughly on ice [8-12].

In contrast to the surface melting, the situation where a highly ordered surface phase is in equilibrium with a less ordered bulk and vapour is rather rare [13]. This phenomenon is referred to as surface freezing (SF). It has been studied so far mainly for alkanes both experimentally and theoretically [14].

Understanding of the phenomena of surface freezing and surface melting is very important not only from the theoretical point of view. They influence many everyday processes. For example, interfacial melting may promote the sintering of solid particles

and the flow of glaciers [15]. The inverse process of interfacial freezing is likely to influence viscoelastic properties of lubricating films and the properties of liquids flowing through ultra-narrow restrictions [16, 17].

The majority of the reported evidences of the SF transition have been observed in long-chain alkanes (C_nH_{2n+2} with $14 < n < 50$) and their mixtures [18-21]. It was found that a solid monolayer is formed on the surface of the solid in a small temperature interval above the bulk solid-liquid transition. The monolayer consists of hexagonally oriented, stretched (*trans*-configuration) alkane chains which are oriented normal, or slightly tilted with respect to the normal, to the surface. Only a single solid monolayer exists in the temperature range between the surface and bulk freezing points and no evidence for the gradual growth of the surface ordered phase approaching the temperature of the bulk transition has been found.

Besides alkanes, SF transitions have been observed so far in liquid crystals [22-25], alcohols [26-30], diols [31], semi-fluorinated alkanes [32] and mixtures of those substances [33]. All these systems contain relatively large, long-chain molecules.

The surface freezing phenomenon in metallic systems, characterized by short-range screened Coulomb interactions, has not been studied so intensively in comparison to the previously mentioned systems. Confirmation for the SF transition was reported so far only for three systems¹: Ga-Bi [34], Ga-Pb [35] and Ga-Tl [36]. The first two systems have been investigated in our group by means of SHG and plasma generation methods [34, 37, 38], surface light scattering [39, 40] as well as by ellipsometry [36, 41]. The SF transition was detected for the entire range of concentrations between the respective eutectic and monotectic points. All three methods are very sensitive for the structural changes on the surface. Precise temperature measurements reveal that the appearance of the solid-like film can be observed several degrees above the solid-liquid coexistence line. This systematic difference between the temperatures of surface and bulk freezing amounts $\sim 12K$ for the composition near to the eutectic point in the Ga-Bi system and decreases for the higher Bi concentrations [34].

These experimental studies certainly help to understand many aspects of the SF phenomenon, but a number of questions remain open. For instance, there is no quantitative information about the thickness and chemical composition of the SF films in

¹ There are also some experimental evidences of the SF transition for the Au-Si system. It was intensively investigated in the group of P. Pershan using X-ray reflectivity and grazing incidence diffraction experiments [42].

the systems mentioned above. The dependence of the film thickness on temperature and cooling rate as well as the thermodynamic stability of the SF films are unknown. The aim of this study is to solve some of these problems.

Basic description of the X-ray photoelectron spectroscopy (XPS) – the primary technique of this work – is given in Ch. 3.1.1 and 3.1.2. This method is used widely in the surface science. Besides high surface sensitivity XPS has another important advantage: the information about chemical composition of the utmost surface layers is directly available from the XPS spectra. In case when the surface is covered by a film, determination of its thickness requires a model of the interface. The overlayer (or slab) model describing the system as a homogeneous, uniformly thick film, consisting of pure Bi or Pb, which covers the bulk (pure Ga), is given in Ch. 3.1.3. This model appeared to be appropriate for wetting films, while the model with variable chemical composition of the film has been successfully applied for surface freezing films in the Ga-Pb system. The discussion in Ch. 6.1 provides a comparison of different models.

Chapter 2.

Interfacial phenomena

2.1 Wetting transition

The simplest illustration of wetting phenomenon is that a liquid droplet on a solid substrate (Fig. 2.1) Depending on the nature of the droplet and substrate, temperature and other parameters of the system one can distinguish three possible wetting states:

- 1) $\Theta = 180^\circ$ - complete drying (non-wet state): liquid does not cover substrate at all.
- 2) $0^\circ < \Theta < 180^\circ$ - partial wetting: substrate is partially covered by liquid. The less the angle Θ , the more is the contact area liquid-substrate.
- 3) $\Theta = 0^\circ$ - complete wetting: substrate is totally covered by liquid film.

The balance of forces shown in the Fig. 2.1b can be expressed by the Young's equation:

$$\cos \Theta = \frac{\sigma_{solid-vapour} - \sigma_{solid-liquid}}{\sigma_{liquid-vapour}} \quad (2.1)$$

where σ is the surface free energy and Θ is the contact angle. Variation of the thermodynamic conditions of the system results in changes of the wetting state, for example, from partial to complete wetting. This transformation is known as a wetting transition. Complete wetting is characterized by a uniformly distributed liquid film, which

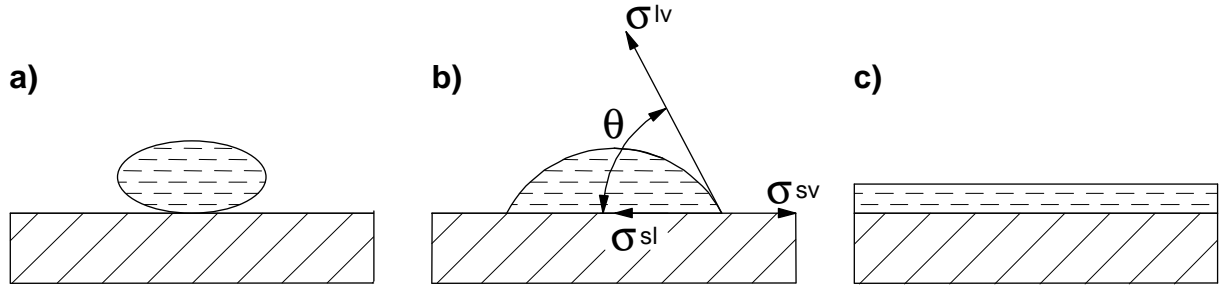


Fig. 2.1 Possible states of wetting for a liquid droplet on a solid substrate: (a) complete drying, $\Theta = 180^\circ$, (b) partial wetting $0^\circ \leq \Theta \leq 180^\circ$, forces in equilibrium are shown with arrows, (c) complete wetting $\Theta = 0^\circ$.

covers the substrate¹. In order to estimate the thickness of the wetting film we first consider a binary liquid mixture exhibiting a miscibility gap with an upper critical point (see also [43]). The bulk phase diagram of such a system is shown in Fig. 2.2. It is necessary to introduce the variable of surface adsorption (or surface excess), which is defined as:

$$\Gamma_i \equiv \frac{N_i^{total} - N_i^{bulk}}{A} \quad (2.2)$$

where N_i is the number of atoms of sort i , A is the area. $\Gamma > 0$ for a surface active component. The theory then predicts the behaviour of the surface adsorption as function of temperature T or chemical potential $\Delta\mu$. Two paths are of particular interest:

- 1) Path Nr. 1. Temperature is increased along the coexistence line (Fig. 2.2, inset 1). For $T < T_w$ Γ_A increases continuously and diverges at T_w this is called a *critical wetting transition*. The second possible scenario is characterized by finite (low) Γ_A for all $T < T_w$. Then at $T = T_w$ it jumps to infinity (for infinitely large systems). The phenomenon is called a *first order wetting transition*.
- 2) Path Nr. 2. Concentration of component A is increased at constant temperature. In this case Γ_A undergoes a discontinuous but finite (microscopic) change when it crosses the prewetting line and then diverges continuously at the coexistence curve. This is known as a *complete wetting transition*.

¹ The theory can be also applied to the liquid substrate with minimal restriction: the shape of the interface will be deformed under influence of the gravity force for the non-wet and partially wet states. Complete wetting for the liquid substrate is similar to the solid one – the interface appears to be flat.

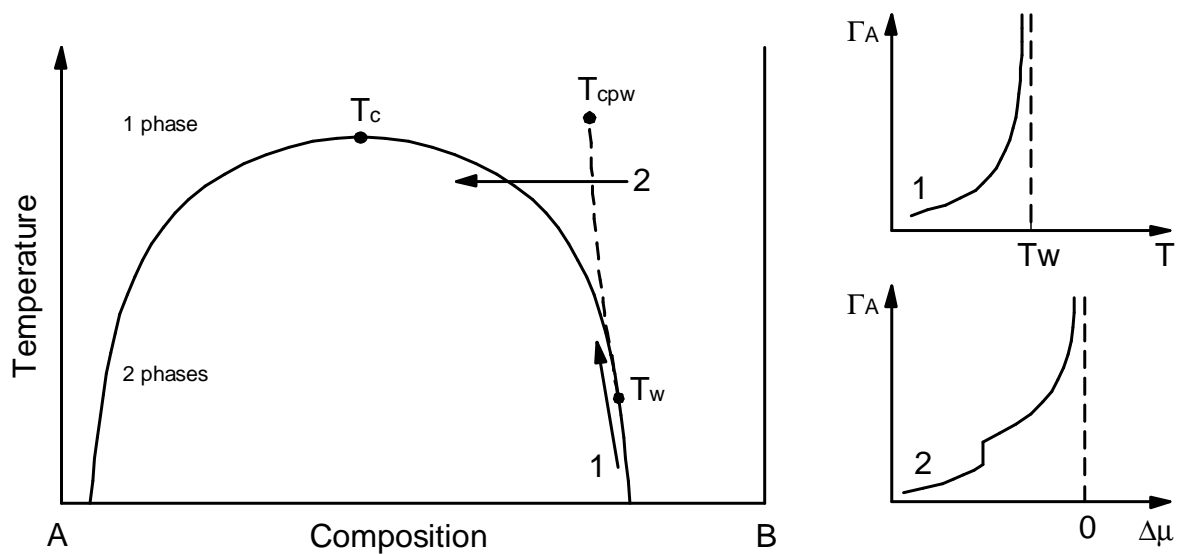


Fig. 2.2 Schematic phase diagram of a binary liquid mixture with a miscibility gap. Prewetting line (dashed) joins wetting (T_w) and critical prewetting (T_{cpw}) points. Two paths of changing the wetting behaviour and surface excess Γ_A are considered: 1. – behaviour of Γ_A along the coexistence line at increasing temperature. It represents a first order wetting transition. 2. – behaviour of Γ_A approaching coexistence line at constant temperature and different chemical potentials, which is related to concentration. $\Delta\mu$ is the chemical potential difference with respect to that at coexistence.

Both described phenomena – divergence of the surface excess Γ_A at a first order and a complete wetting transition – imply for an infinitely large system formation of infinitely thick wetting films since the surface excess Γ_A can be assumed to be proportional to the wetting film thickness. For real systems this means that macroscopically thick films are formed. Thin wetting films that correspond to low values of Γ_A are of special interest for this study.

For a quantitative description of the films various theoretical approaches of statistical thermodynamics have been developed [44-46]. Understanding of wetting phenomena was considerably advanced by the so-called van der Waals theory. A central role in this theory plays the effective interfacial potential Ω^{eff} , which is derived from grand canonical potential Ω . The attractive parts of the interactions are treated in mean-field approximation, so that one obtains the following expression for two coexisting phases α and β in contact with substrate γ [44]:

$$\Omega^{\text{eff}}(d, T, \mu) = \sigma_{\alpha\beta} + \sigma_{\alpha\gamma} + d\Delta\mu - \omega(d) \quad (2.3)$$

where $\Delta\mu$ is the deviation of the chemical potential relative to that at coexistence, $\sigma_{\alpha\beta}$ and $\sigma_{\alpha\gamma}$ are the surface free energies (β denotes the non-wetting phase). The term $\omega(d)$ describes the correction of the surface energies due to the finite thickness of the wetting film, whereby the gravitational influence can be neglected. For different types of liquids the expression for $\omega(d)$ is different. According to Israelachvili [47] for the van der Waals type liquid $\omega(d) = -H/d^2$, where H is the Hamaker constant. Then minimizing Ω^{eff} the equilibrium thickness of the wetting film is:

$$d_0 = \left(\frac{2H}{\Delta\mu} \right)^{1/3} \quad (2.4)$$

In case of exponentially decaying short-range interactions (Yukawa liquid) the term $\omega(d)$ can be approximated by $\omega(d) = -\sigma_0 \exp(-\lambda d)$ [48] and the corresponding wetting films have a logarithmic divergence at coexistence ($\Delta\mu = 0$) according to:

$$d_0 = \frac{1}{\lambda} \ln \left(\frac{\lambda \sigma_0}{\Delta\mu} \right) \quad (2.5)$$

where $1/\lambda$ is the screening length. This theory does not take into account factors that usually affect real systems under investigation such as diffusion, heat transfer and other kinetic effects.

2.2 Surface freezing transition

In comparison to wetting transitions it is more difficult to describe the surface freezing (SF) transition using a simple model. This interfacial phenomenon is not studied yet in detail despite of a considerable high number of publications concerning this issue during the last years [17, 49, 50].

Describing the SF transition it is sometimes useful to consider it together with the surface melting phenomenon. Generally speaking, the fact that the free energy of atoms on the surface differs from that of the atoms in the bulk is a driving force for both

interfacial phenomena. Surface melting can be considered to be a special case of “wetting”, namely wetting of the solid by its own melt. By analogy, SF is “wetting” of the liquid by its own solid. An important issue is whether or not the thickness of the frozen films diverges as the bulk melting temperature is approached.

Schematically the SF transition is shown in the Fig. 2.3. The thermodynamic quantity that governs the freezing or non-freezing behaviour of the surface assuming macroscopically thick films is the surface free energy σ [51]:

$$\Delta\sigma^* = \sigma_{\text{liquid-vapour}} - \sigma_{\text{solid-vapour}} - \sigma_{\text{solid-liquid}} \quad (2.6)$$

A positive value of $\Delta\sigma^*$ predicts complete surface freezing, whereas a negative one predicts non-freezing. However this conclusion can be strictly applied for macroscopically thick films, where the corresponding surface energies are defined and no correction term $\omega(d)$ is necessary (see also Ch. 2.1). An estimate of $\Delta\sigma^*$ for metallic systems based on semi-empirical values for the interfacial energies yields for the most elements negative values [51]. This means that complete SF of metals above melting temperature is unlikely. Monte Carlo simulations for metallic liquids [52, 53] indicate a layer-wise ordering of the atoms at the surface that rapidly decays with increasing depth. Recent X-ray reflectivity studies have also revealed a decaying oscillatory density profile at the free surface of metals with high surface tension like Ga [54] and Hg [55]. Another

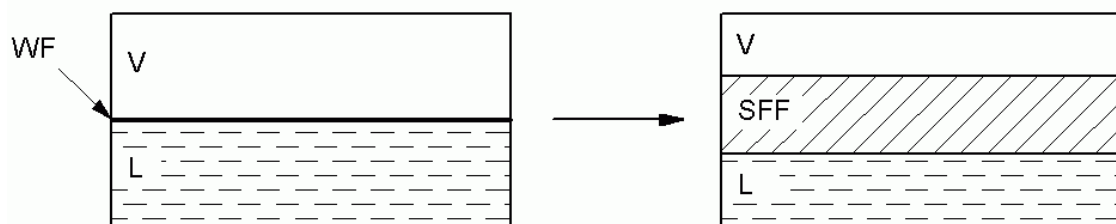


Fig. 2.3 Schematic illustration of the surface freezing transition. The top monolayer of the liquid becomes ordered at a temperature a few degrees above the bulk melting point, while the bulk liquid remains disordered. For alkanes the thickness of 1ML remains constant as the temperature is lowered toward and even below the bulk melting point without triggering bulk crystallization. Surface freezing requires the sum of the solid-vapour and the solid-liquid interfacial energies to be smaller than that for the liquid-vapour interface.

example of the interfacial ordering (freezing) was demonstrated for the liquid Ga, which was brought into contact with solid hard wall (diamond) [56].

Combining eq. (2.6), with Young's equation (2.1) and taking into account that $\Delta\sigma^* > 0$ for the SF transition the following expression for the contact angle Θ can be obtained:

$$\cos\Theta = \frac{\sigma_{sv} - \sigma_{sl}}{\sigma_{lv}} < \frac{\sigma_{sv} + \sigma_{sl}}{\sigma_{lv}} < 1 \quad (2.7)$$

(since σ is always positive). This suggests that surface freezing is associated with dewetting [49]. The contact angle of the solid with its own melt is finite (it is also the case for incomplete surface melting [57]); this condition is further enhanced for the SF

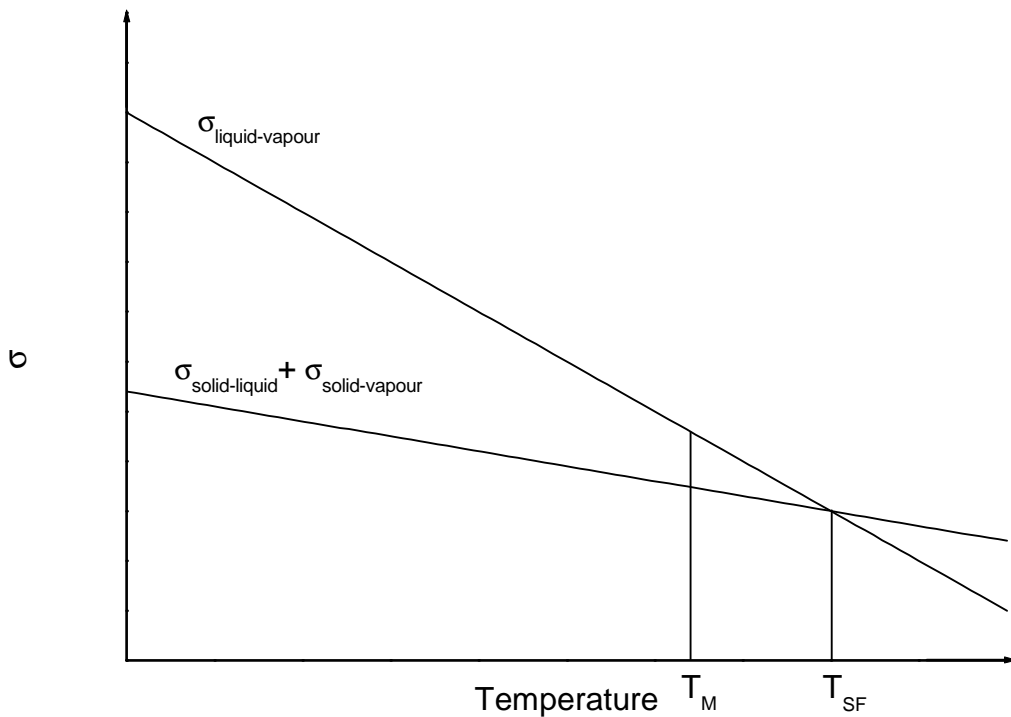


Fig. 2.4 Temperature dependence of the surface tension in the vicinity of the bulk melting point T_m . The liquid-vapour below the SF point (T_{SF}) is linear extrapolation of the slope from temperatures above T_{SF} , where the liquid state of the surface is thermodynamically stable. Surface solid can coexist with the melted surface at $T = T_{SF}$ like macroscopic solid and liquid phase coexist at $T = T_m$. The slope of the $\sigma_{lv}(T)$ and $(\sigma_{lv} + \sigma_{sv})(T)$ functions varies for different kind of systems: this figure corresponds to metallic systems, whereas for n -alkanes the slope of the $(\sigma_{lv} + \sigma_{sv})(T)$ becomes negative.

case). Consideration of the temperature dependence of the surface tension shows that there should be a lower limit to the contact angle allowed in a system that exhibits SF. Assuming that the interfacial energies of either side of the SF film can be expressed in terms of macroscopic $\sigma_{\text{solid-vapour}}$ and $\sigma_{\text{solid-liquid}}$, the lower bound follows by equating $\sigma_{\text{solid-liquid}}$ to zero.

The liquid-vapour interfacial energy is shown in Fig. 2.4. For the region below SF temperature the $\sigma_{\text{liquid-vapour}}$ is a linear extrapolation of the line, having a negative slope from the higher temperatures [58]. The study of the surface tension for this metastable region for *n*-alkanes demonstrated that the SF transition can occur either below or above the bulk melting point [58]. It has been also shown that macroscopic interfacial energies for either side of the frozen film can be used as a first order approximation, because it explains an experimentally observed value of the contact angle for *n*-alkane droplet on the silica [49, 59].

The following theory of SF of *n*-alkanes has been proposed by Tkachenko and Rabin [14]: Surface monolayer is entropically stabilized by fluctuations along the axis of the normally oriented chain-like molecules. Stabilization against bulk freezing is reached through entropic repulsion between adjacent solid layers. Though designed to explain the surface behaviour of *n*-alkanes, the model suggests that the phenomenon might be a general feature of straight chain-like molecules of intermediate molecular weight. The model appears to be controversial since some parameters associated with the interfacial energies in the calculation do not agree with the experimental values [60].

A mechanism of the SF film formation in binary alloys has been proposed by Freyland et al. [61]. Wetting film on the liquid-vapour interface slightly above the liquidus line is considered as undercooled Bi or Pb liquid film, because the temperature of the system in this case is well below the corresponding freezing temperature of the bulk Bi or Pb. At a given undercooling $\Delta T = T_m(\text{bulk}) - T_{SF}$ freezing of the film may be triggered if its thickness d reaches the size of a critical nucleus, R_c . If a homogeneous nucleation is assumed and a critical nuclei radius is expressed as follows:

$$R_c = \frac{2\sigma_{\text{liquid-solid}}}{n\Delta\mu} \quad (2.8)$$

one can estimate $R_c \sim 1\text{nm}$ for $\Delta T = 200\text{K}$. Taking into account, that $n\Delta\mu$ is proportional to the undercooling ΔT , one expect a growth of the SF film when a bulk Bi or Pb

concentration is increased approaching the monotectic point. A kinetic of the SF film formation is predicted to be fast, since the energy barrier is zero at complete wetting.

Summarizing the available information about SF transition one can conclude that both experimental and theoretical efforts are essential for the further understanding of this phenomenon.

Chapter 3.

Applied methods

3.1 Electron spectroscopy

3.1.1 Basic principles of XPS, AES and UPS

If the surface of some material undergoes a radiation of photons or electrons of sufficient energy it starts to emit its own electrons. For the case of photons this phenomenon is known as photoeffect, whereas the interaction caused by high-energy electrons with the electronic shell of atoms is denoted as Auger-effect. The energy of incident photons or electrons must be greater than the binding energy of the ejected electrons in the material under investigation. The analysis of the kinetic energy distribution of electrons allows important information about the electronic structure of the substrate. For example, chemical composition, oxidation state, electronic structure and many other properties can be determined by means of electron spectroscopy (ES). In this study it was mainly utilized for purposes of quantitative chemical analysis.

Generally ES is divided into three broad areas, depending on the source used for excitation of the sample. The first one is Auger electron spectroscopy (AES) employing an electron beam, whose interaction with sample results in emission of Auger electrons. The second one is X-ray photoelectron spectroscopy (XPS); it utilizes X-rays producing both Auger- and photoelectrons. The third one operating with ultraviolet radiation is known as ultraviolet photoelectron spectroscopy (UPS). Ejection of electrons followed by

its detection is a common feature of all three techniques mentioned above. This appears to be a great advantage which allows one to combine those methods in one experimental setup. Let's consider the physical processes that take place in AES, XPS and UPS in detail.

The changes in the electronic structure in the case of the Auger-effect are shown in Fig 3.1c. The incident electron with energy of typically 1-10keV ejects one of core electrons of the shell producing a hole (level K in the scheme). This results in the decay of an electron from a higher energy orbital (E_{L1}). The excess energy released by the latter process is transferred to an electron on the third orbital ($E_{L2,3}$), forcing it to be ejected. This last electron is detected when passing the energy analyzer.

There can be different combinations of neighbouring electron levels taking part in Auger-processes, especially for large atoms. The kinetic energy of Auger electrons determined with the electron detector can be written as

$$E_{Auger} = E_1 - E_2 - E_3 - U_{eff} \quad (3.1)$$

where E_1 , E_2 and E_3 are the energies of the three electrons, involved in the process and U_{eff} is the extra energy required to remove an electron from a double ionized atom. One can notice that the energy of incident electron is not included in the expression (3.1). This means, that the registered kinetic energy of the corresponding Auger peak remains constant even if the energy of the primary beam is changed.

The process of electron emission in the case of XPS and UPS is shown schematically in Fig 3.1a and 3.1b. The energy balance is described with following relationship:

$$E_k = h\nu - E_b - W \quad (3.2)$$

where $h\nu$ is the photon energy; E_b and E_k are the binding energy of the electron in the atom and the kinetic energy of emitted electron respectively; W is work function of detector. Binding energy of the electron in atom is specific for every element and electronic shell. This allows to determine the chemical composition of the surface.

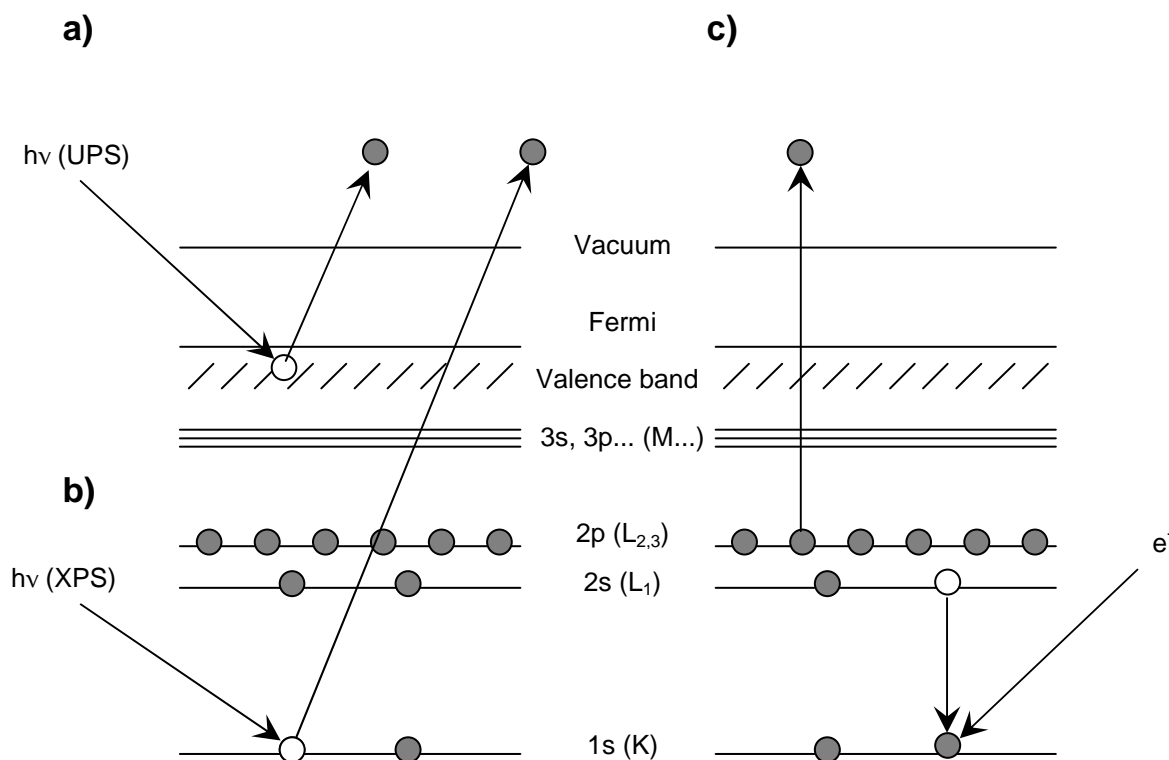


Fig. 3.1 Schematic diagram of the processes of an electron emission. Electrons are depicted as filled circles. The interactions of the atom with UV-radiation (a), X-rays (b) and electron beam (Auger effect) (c) are shown.

Those photoelectrons, which are excited and escape without energy loss, contribute to characteristic peaks in the spectrum. Here is a brief description of the nomenclature of XPS and Auger transitions. The following notation is used in XPS: nl_k , where n is the principal quantum number; l corresponds to the orbital quantum number (for $l=0,1,2,3$ – s,p,d,f are used); k is the absolute value of the sum of l and spin quantum number, which can accept values of either $+1/2$ or $-1/2$. The AES notation has the general form A_b , where A is a capital letter K,L,M etc., which is used instead of the principal quantum number n ; b varied from 1 to $(2l_{\max}+1)$. The entire AES label has three notations, for example KL_1L_3 , because three electrons are involved in the Auger transition. Since the exact information about these electrons is not available (or not important), small indices are often omitted.

Usually, together with the main transition peak a number of signals with lower intensity are to be found in ES spectra. These peaks, known as satellites, reflect minor processes of electronic shell relaxation and other secondary effects. Their position in the spectrum is shifted in positive or negative direction of the kinetic energy scale in

comparison to the main peak. The perturbations which give rise to these peaks are just mentioned here without further description (for detailed information see [62]). These small peaks can have different origins, e.g. *chemical shift* (not all atoms of element X have same oxidation state, e.g. core electrons, emitted from positively charged ions have lower kinetic energy in comparison to neutral atoms); *bulk* and *surface plasmon* excitation (the outgoing electron excites collective oscillation in the conduction band; this is found for metallic surfaces); “*shake-up*” effect (interaction of the outgoing electron with conduction band states; if the electron in the conduction band does not gain some energy, but it is completely ejected, this is referred to as “*shake off*” effect); *multiplet splitting signals* (arise from different spin distribution of the electrons in the band structure). These features may contain important information about the surface. For example, in this study the absence of impurities on the surface (like oxides) has been checked by means of XPS: the spectrum of an oxidized surface has oxygen peaks as well as shifted peaks of the metals.

Besides XPS and AES satellites, which appear because of the above processes in the sample, so-called “ghosts” are sometimes found in XPS spectra. They originate from impurities in the X-ray source. Through the oxidation of the anode material (see next chapter) or misalignments inside the source, the outgoing X-ray radiation may have some noise lines besides the main one. In this case the kinetic energy of the peaks, which additionally appear in the spectrum, differs from the energy of the main peaks.

UPS as well as XPS uses the principle of the photoeffect. The difference is that the energy of photons in the case of UPS is some two orders of magnitude lower than the energy of X-rays. Therefore it is possible to excite electrons only in the valence band. UPS is used to study the electronic structure of molecular compounds, to determine the electron work function etc. In this study the band structure of interfacial bismuth has been determined with the help of UPS.

3.1.2 Radiation sources and electron detection in electron spectroscopy

As a source of X-rays the twin anode X-ray tube was applied. Thermally emitted electrons accelerated by a voltage up to 15kV interact with the anode material, emitting X-ray radiation. It consists of an intense narrow line accompanied by weak radiation with higher wavelength. The origin of the first feature is X-ray fluorescence, while the second

one (known as Bremsstrahlung) results from the inelastic interaction of high energy electrons with the positively charged atomic nucleus. The energy of the X-ray fluorescence line depends on the material of the anode: in our case it was 1253.6 eV for Al and 1486.6 eV for Mg (in both elements $K\alpha$ transition occurs). In principle such a combination of anodes provides the possibility of depth profiling due to different kinetic energies of the outgoing electrons.

The electron beam for AES is generated using an electron gun. A hairpin-shaped tungsten filament heated by electric current serves as electron source. Besides the filament, the electron gun has a number of electrostatic lenses which are used to accelerate the electrons, to focus the electron beam and to deflect it. Thus it is possible to generate a stable, mono-energetic and bright electron beam of narrow cross-section ($<1\text{mm}^2$).

Ultraviolet radiation for UPS is generated by means of a gas discharge tube. With the help of fine a leak valve the pressure of helium of some 10^{-2} mbar can be achieved. The discharge zone is connected to the analysis chamber, so a very effective differential pumping system is required keep the pressure in the UHV region. The radiation emitted by HeI (21.2eV) and HeII (40.8eV) transitions is applied in this study.

To analyze the kinetic energy of electrons emitted from the sample, the HemiSpherical electron energy Analyzer (HSA) (Fig. 3.2) was utilized. It consists of a pair of concentric hemispherical electrodes, between which there is a gap for the electrons to pass (1); a sequence of electrostatic lenses (5) is mounted in the tube (2), shielded by the material with high magnetic permeability (μ -metal) from the Earth's magnetic field. The lenses are used to vary the area on the surface of the sample to be analyzed, to change the acceptance criteria concerning the angle distribution of analyzed electrons and to retard the electrons with high kinetic energy, which allows to increase the analyzer resolution. The battery of electron multipliers (channeltrons ®) (3) is located on the other side of the hemispherical cap. The electron flux can be additionally regulated by means of entrance and exit slits (4).

A potential difference is applied across the two hemispherical electrodes, with the outer one being more negative than the inner one. Only those electrons, which possess energy given by

$$E = -e\Delta V \left(\frac{R_1 R_2}{R_1^2 - R_2^2} \right) \quad (3.3)$$

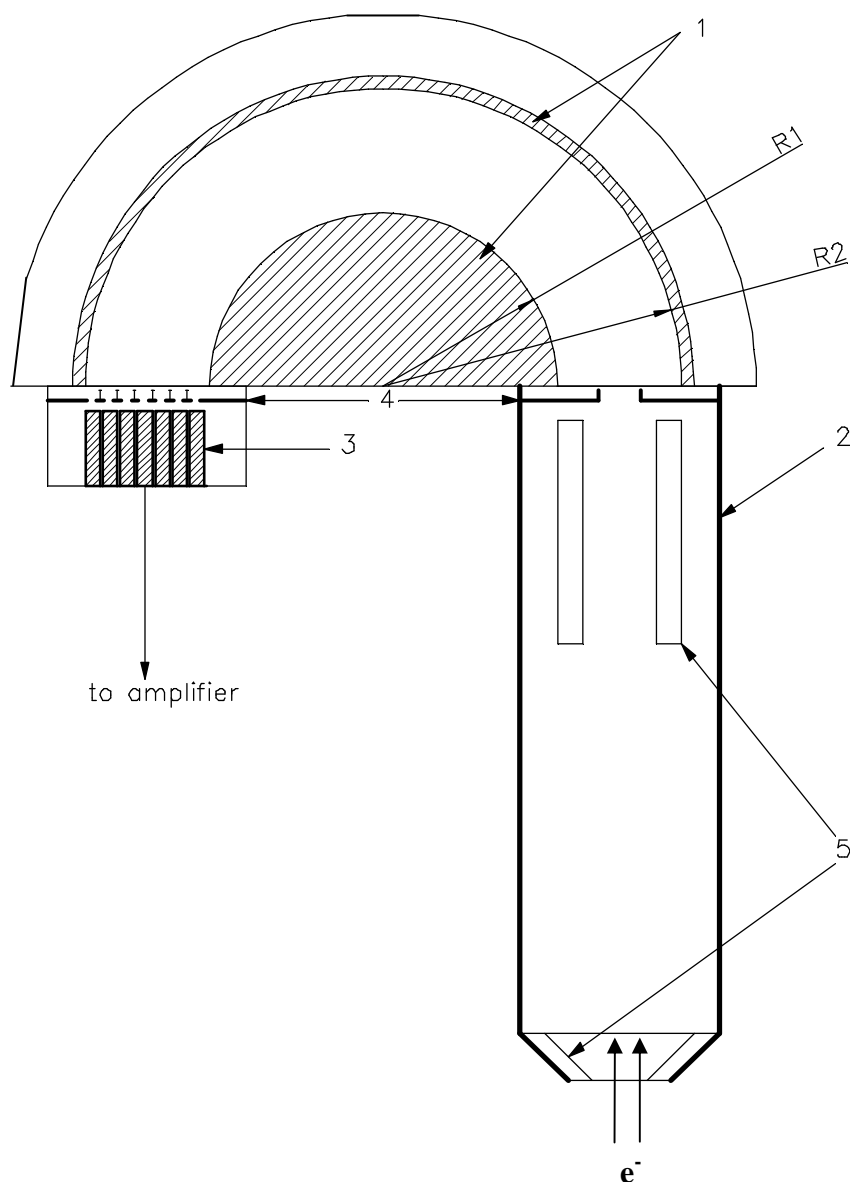


Fig. 3.2 Scheme of the hemispherical electron analyzer (HSA). 1 – two hemispherical electrodes with the radii R_1 and R_2 , 2 – entrance tube shielded from any external magnetic field, 3 – battery of 7 channeltrons, which are used to detect the electrons, 4 – slits used to control electron flux, 5 – electrostatic lenses focus and retard the electrons. Electrons enter the analyzer from below and pass through the electrostatic lenses (5) and the gap between electrodes (1) followed by the detection in the channeltrons (3).

at the entrance of the analyzer's cap will reach the detector. Here E is the kinetic energy of the electrons, e is the charge of electron, ΔV is the potential difference between hemispheres, R_1 and R_2 are the radii of inner and outer hemispheres respectively) One can notice that the kinetic energy is directly proportional to the applied potential difference.

The electrons with much higher (lower) energy in comparison to the value given by expression (3.3) have larger (smaller) radius of the trajectory and collide with walls of hemispheres. But if the difference in kinetic energy is not large, those electrons can also reach the output plane of the analyser. Several channeltrons on the output plane are arranged radially so that each of them can detect electrons with different kinetic energy $E \pm \delta E$. The entire sensitivity of the instrument is increased by a factor equal to the number of channeltrons.

Two operating modi are available for HSA: Constant Analyser Energy mode (CAE) and Constant Retard Ratio mode (CRR). In the CAE mode the electrons are accelerated or retarded to some user defined value (known as pass energy) with the help of electrostatic lenses before they enter the hemispherical cap. The difference of the hemisphere potentials remains constant throughout the energy range. In the CRR mode the electrons entering the analyser are retarded to a constant fraction of their original kinetic energy so that the ratio of electron kinetic energy to the analyser pass energy is kept constant for the whole spectrum. In order to achieve analysis in the CRR mode, the hemispheres potential difference is increased with growing kinetic energy. The retard ratio is defined as

$$k = \frac{E_{kinetic} - \varphi_a}{E_{pass}} \approx \frac{E_{kinetic}}{E_{pass}} \quad (3.4)$$

where φ_a is the work function of the analyser. The resolution and the sensitivity are different for the CAE and CRR modi. The CAE mode is preferred if one wants to achieve a constant resolution throughout the whole kinetic energy range; the sensitivity, however, is inversely proportional to the kinetic energy. In the CRR mode both parameters are proportional to the pass energy (and therefore kinetic energy); sensitivity is reduced at lower kinetic energy. At the higher kinetic energy in the CRR mode the resolution can be improved by increase of the retard ratio. The analysed sample area and the distribution of acceptor emission angle remains almost constant in the CRR mode or they vary slightly with the kinetic energy in CAE mode. The CAE mode is usually applied for the acquisition of XPS spectra and for the quantitative analysis. The CRR mode is more suitable for AES with lower kinetic energy of emitted electrons.

The single electron multiplier or channeltron consists of a spiral-shaped glass tube with a conical entrance at one end and a metal anode output plate at the other. A material, which coats the internal walls of channeltrons, emits several secondary electrons being hit by a primary electron with kinetic energy greater than the work function of the channeltron. Those secondary electrons are accelerated within the tube and then, colliding with the walls, they produce additional electrons progressively so that the electrical signal can be detected at the output plate.

3.1.3 Quantification with XPS and AES

XPS and AES are known to be powerful tools for quantitative chemical analysis. The incident X-ray radiation and high-energy electrons are able to penetrate and to ionize the material of the sample well deep ($>10^3\text{\AA}$). But only a small fraction of the electrons expelled in such a way can leave the material without energy loss. The main source of

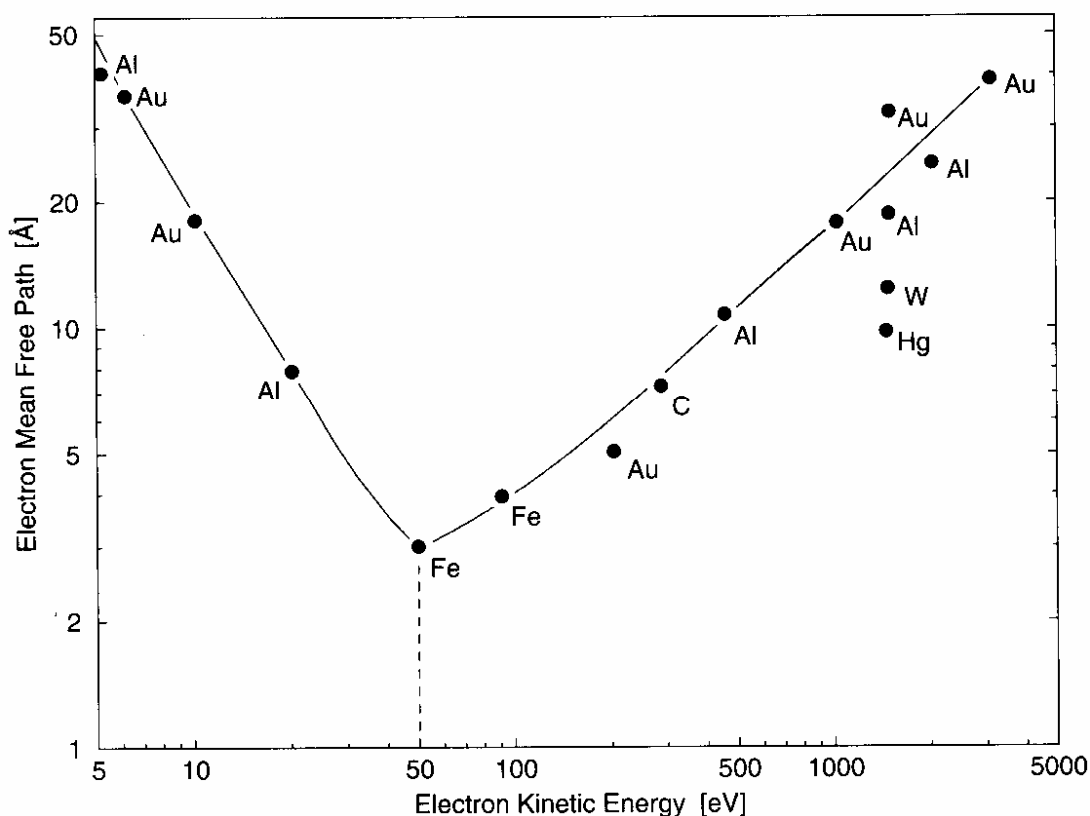


Fig. 3.3 The dependence of the electron inelastic mean free path (IMFP) λ on the emitted electron energy for different elements [64].

energy losses comes from the interactions of the outgoing electrons with surrounding atoms. The deeper the ionisation centre, the greater the probability of inelastic scattering. Therefore only those electrons, which originate from the outermost surface layers will escape elastically from the material and can be subsequently detected. This makes ES an extremely surface sensitive technique. The average escape depth, which is also known as Inelastic Mean Free Path (IMFP) or Effective Attenuation Length (EAL) requires special consideration.

First of all, the IMFP of the emitted electrons depends on their kinetic energy as is shown in Fig.3.3. A so-called universal curve describes IMFP for most of the chemical elements. It has a minimum around 20-50 eV, this region of kinetic energy corresponds to the maximum of surface sensitivity of ES. The increase of IMFP on the left of the minimum can be explained by taking into account the decrease of energetically allowed scattering processes. With growing kinetic energy the impact cross-section will shrink, so that the IMFP will be greater.

Considering the intensity (I) of a photoelectron peak from a homogeneous solid, it can be expressed in simplified form as [63]:

$$I_A = J \cdot \rho \cdot \sigma \cdot K \cdot \lambda \quad (3.5)$$

where J is the photon flux, ρ is density of atoms of sort A in the investigated material, σ is the cross-section for the electron production (which depends on the element and energy being considered), K is a term which covers all instrumental factors, like transmission, analyser settings, efficiency of the detector or stray magnetic fields, affecting the transmission of low-energy electrons and λ is the IMFP. The intensity is usually measured as integrated area under the peak in an ES spectrum. For a preliminary evaluation the height of the peak can be taken instead of its area.

In order to increase the precision of the intensity determination an appropriate method of background subtraction is required. The options are simple linear cut or improved S-shaped background subtraction, which is also known as Shirley method [65]. The equation 3.5 can be theoretically used for direct quantification (so-called first principles approach). A more usual way of quantification implies experimental determination of sensitivity, which includes the terms σ , K and λ . They are incorporated in

the intensity (I_0^A) acquired from the sample with thickness $d \gg \lambda$, consisting of pure element A, which has the same size and shape as the samples under investigation.

For quantified description of electron scattering in the material the modified Lambert-Beer law can be applied:

$$\ln \frac{I_0}{I} = \varepsilon \cdot d \quad (3.6)$$

The ε can be substituted with $1/\lambda$:

$$I = I_0 \cdot \exp\left(\frac{-d}{\lambda}\right) \quad (3.7)$$

where I is the intensity of electrons emitted from all depths, greater than d , normal to the surface, I_0 is the intensity from infinitely thick, uniform substrate, ε is the extinction coefficient, $\lambda = \text{IMFP}$. The distribution of the number of escaped electrons as a function of the depth, at which they are emitted, is shown on the Fig. 3.4.

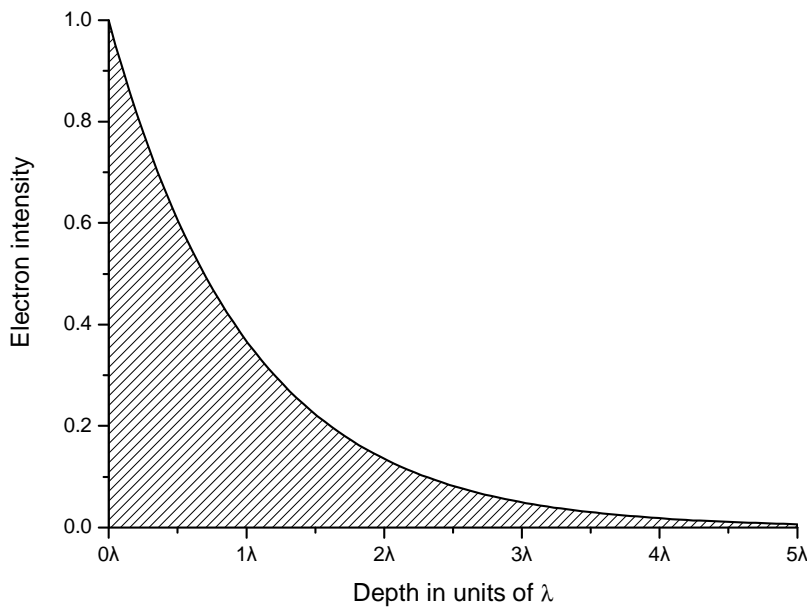


Fig. 3.4 The distribution of the number of escaped electrons as a function of the depth, at which they are emitted. Approx. 95% of the entire signal for homogeneous, one-component material originates from the depths $0 > d > 3\lambda$.

One can see that some 65% of the entire signal in the detected XPS (or AES) peak come from the depth less than λ , some 20% come from the slab between λ and 2λ , ~10% from $2\lambda < d < 3\lambda$ and less than 5% of the signal originate from the substrate with $d > 3\lambda$. Taking into account the typical values for λ of 10-30Å one can ensure once again the ultimate surface sensitivity of ES.

Usually not only those electrons, which are emitted normally to the surface can be detected, but also those, which are emitted at some angle θ , different from 90° . Then expression (3.7) becomes:

$$I = I_0 \cdot \exp\left(\frac{-d}{\lambda \cdot \cos \theta}\right) \quad (3.8)$$

Here the surface sensitivity is increased and the effective analytical depth is decreased with decreasing θ .

We can consider the more complicated case of a non-uniform substrate containing several chemical elements (or their compounds). If the signal of an atom occurs in the XPS or AES spectrum, it is unfortunately impossible to define immediately the position (= the depth) of this atom in the sample. It can be located at the first monolayer at the surface or at the fifth one – with 95% probability it is not deeper than 3λ . Therefore additional consideration of the sample nature is required like, for example, increase of the concentration of surface active component in the first monolayer. In other words the problem can be solved if it is possible to construct a feasible model.

A simple and at the same time appropriate model for XPS data analysis, which is used in this study to describe surface freezing in a two-component metallic system is the so-called overlayer model (Fig 3.5; other notations are slab- and three phases model). The model implies that the bulk alloy is covered by a thin overlayer film. Let us assume that the overlayer consists of pure component A. So the intensity of the A peak in the spectrum is expressed as follows:

$$I^A = I_0^A \left(1 - \exp\left(\frac{-d_A}{\lambda_A \cdot \cos \theta}\right) \right) \quad (3.9)$$

where d is overlayer thickness; I_0^A is the intensity measured from an infinitely thick substrate, consisting of pure A; $\lambda_A = \lambda(E_A)$ is the IMFP for the electrons, emitted from A, which have the kinetic energy, characteristic for the considered transition. From the bulk, consisting of pure element B, the intensity I^B is described as:

$$I^B = I_0^B \cdot \exp\left(\frac{-d_A}{\lambda'_A \cdot \cos\theta}\right) \quad (3.10)$$

where $\lambda'_A = \lambda(E_B)$ is IMFP at the kinetic energy of the B peak in pure A (in order to reach the detector, the electrons emitted in the bulk must go through the overlayer, consisting of A). One can see that if the overlayer thickness d_A is much greater than λ'_A , the signal from the bulk will be completely attenuated in the overlayer. So this model can be directly applied only for systems with relative modest overlayer thickness.

All variables in expressions (3.9) and (3.10) except of d can be either measured (I_0^A , I_0^B , I^A , I^B , θ) or found in literature or databases (λ_A , λ'_A). Therefore, the overlayer thickness d can be calculated.

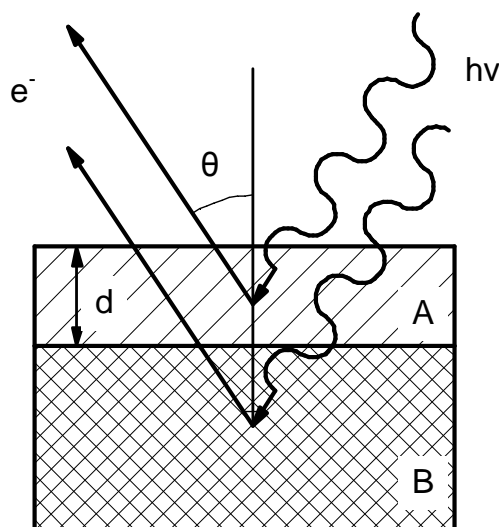


Fig. 3.5 Scheme of the overlayer (or slab) model used for the characterization of thin films in this study. The film consists of one component A, the bulk is the pure component B. X-rays penetrate the film and the top of the bulk emitting electrons. The probability, that the electron will be detected without energy loss, depends on the length of its trajectory in material. The higher the IMFP, the deeper emitted electrons can be detected.

One can extend the overlayer model for the case when the overlayer and/or the bulk become homogeneous mixtures of A and B with different concentrations. In this case the expressions for I^A and I^B would be more complicated because they result from the combination of (3.9) and (3.10):

$$I^A = I_0^A \cdot \left(x_o^A \cdot \left(1 - \exp\left(\frac{-d_A}{\lambda_{E_A} \cdot \cos\theta}\right) \right) + x_b^A \cdot \exp\left(\frac{-d_A}{\lambda_{E_A} \cdot \cos\theta}\right) \right) \quad (3.11)$$

$$I^B = I_0^B \cdot \left((1 - x_o^A) \cdot \left(1 - \exp\left(\frac{-d_A}{\lambda'_{E_B} \cdot \cos\theta}\right) \right) + (1 - x_b^A) \cdot \exp\left(\frac{-d_A}{\lambda'_{E_B} \cdot \cos\theta}\right) \right) \quad (3.12)$$

Here x_b^A and x_o^A are mole fractions of A in the bulk and in the overlayer respectively. As it is well known, at fixed kinetic energy the value of λ does not depend much on the kind of material. So it can be estimated very good also for mixtures [62].

For the quantitative analysis of AES data the equations derived above can be applied only with the correction for backscattering electrons:

$$I = I_0(1 + r(E_A)) \cdot \exp\left(\frac{-d}{\lambda(E_A)}\right) \quad (3.13)$$

where $r(E_A)$ is the backscattering factor, see also [62]. For rough estimation this additional term can be neglected.

3.1.4 Depth profiling

The task of depth profiling is to describe the distribution of different chemical elements in the material under investigation. A very important assumption here is that the sample is homogeneous in lateral direction i.e. the gradient of the concentration of all components in X and Y directions (Z is normal to the surface) is zero. This assumption is not always valid, but it can simplify the description of the system and interpretation of experimental results.

The theory reported in the last chapter can be applied for the solution of the depth profiling problem if the system under investigation has rather simple structure like a thin

homogeneous overlayer. The thickness of the overlayer cannot be measured reliable if it becomes much larger in comparison to IMFP. The situation will be even more complicated if the system has more than one overlayer or the distribution of chemical elements in them is unknown. In this case one can receive the information about the system by stepwise removal of atoms from the surface. This can be done e.g. by means of sputtering of the surface by noble gases ions, the same procedure as used for cleaning of samples in vacuum.

The method mentioned above is visualized on Fig. (3.6). The data collected during a depth profiling experiment are the intensities of the detected elements I as a function of sputtering time t . This so-called “measured sputtering profile” is to be converted into the original distribution of concentration C with depth z , $C = C(z)$. First the sputtering time scale must be calibrated in terms of mean eroded depth, $z = z(t)$, then the XPS or AES signals must be calibrated in terms of local concentrations $C = C(I)$. So the measured concentration profile

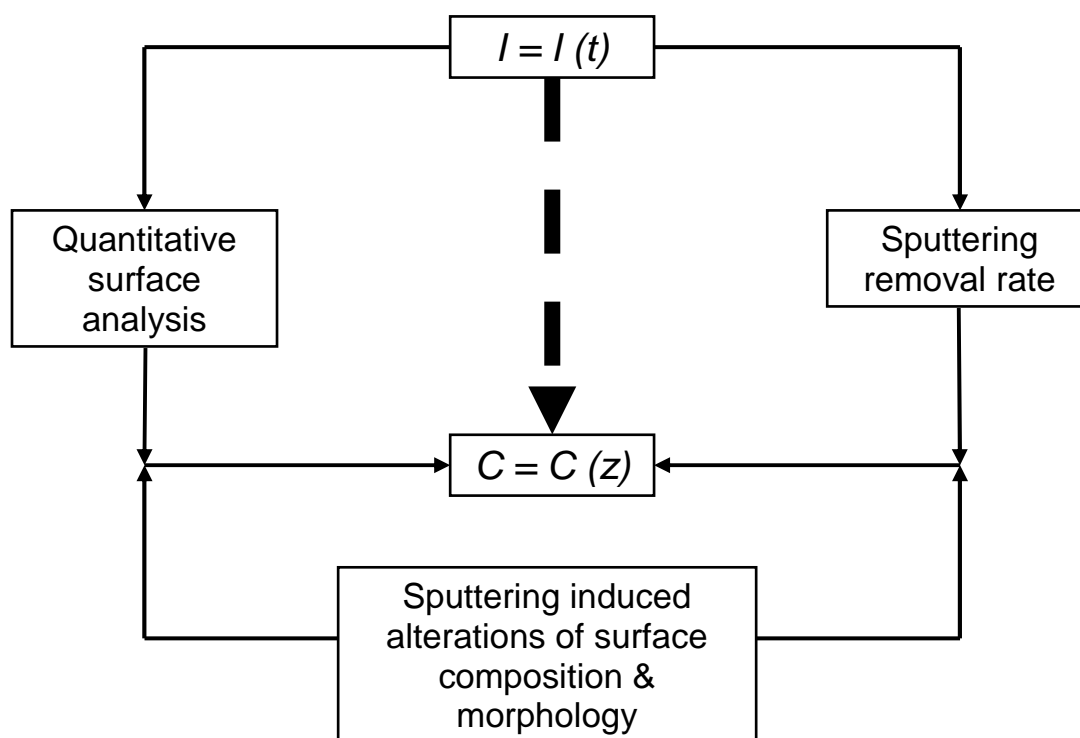


Fig. 3.6 Principles of sputtering profile evaluation: conversion of a measured sputtering profile $I = I(t)$, to a true concentration profile $C = C(z)$.

will correspond to the original “true” profile. However, the sputtering is not always a homogeneous process, i.e. the atoms will not be removed from the surface ideally, layer-by-layer. Phenomena such as preferential sputtering or topographical profile distortions as well as changes of the IMFP must be taken into account in a second step in order to reveal the true original profile $C = C(z)$. A deviation between the measured profile and the true one can be described by depth resolution [62].

The velocity of surface erosion $z = z(t)$ can be either obtained in calibration experiments with a sample containing an overlayer of known chemical composition and thickness, or calculated with the following formula:

$$z(t) = \int_0^t \frac{M}{\rho \cdot N_A \cdot e} S \cdot j_p dt \quad (3.13)$$

where M = molar mass, ρ = density, N_A = Avogadro number, e = electron charge; S = sputtering yield (atoms/ion), j_p = primary ion current density. The detected XPS intensity for element i can be generally expressed as:

$$I^i = \frac{I_0^i}{\lambda^i} \int_0^\infty C^i(z) \cdot \exp\left(\frac{-z}{\lambda^i}\right) dz \quad (3.14)$$

I_0^i here is the intensity from infinitely thick sample. The solution for an arbitrary profile is given by:

$$C^i(z) = \left(\frac{I^i}{I_0^i}\right) - \frac{d(I^i / I_0^i)}{dz} \cdot \lambda^i \quad (3.15)$$

In practice a cyclic procedure consisting of XPS (or AES) measurement followed by scattering during definite time is applied.

An important restriction of the described depth profiling method is that the investigated material must be stable in time. This is almost always the case for solid systems without chemical reactions. Such a method cannot be used directly for study of surface freezing phenomena, where the bulk remains liquid. Another limitation is that this method is invasive by nature (in comparison to non-invasive XPS or AES).

3.2 Scanning tunneling microscopy

3.2.1 Theoretical concept

Scanning tunneling microscopy (STM) and spectroscopy (STS) use the electron tunneling effect; this can be described only with the help of quantum mechanics. The tunneling effect is defined by the transition of an electron between two states, which are separated by potential barrier; the energy of the electron here is not sufficient to overcome the barrier according to classical mechanics. The height and the width of the barrier affect the probability of the transition. This effect is utilized in tunneling microscope, which was invented in 1982 by Binnig, Rohrer and Gerber [66]. A sharp metal needle (so-called tunneling tip) is placed very close to the surface of an electrically conductive material in this device. Despite of the absence of direct electrical contact, a weak, but measurable electrical current, resulting from electron tunneling, can be detected if the voltage is applied between the tip and the surface. The tip can be driven by piezoelectric device in three dimensions and its position is known precisely; in this way a topographical map of the surface under investigation can be obtained.

Qualitatively the tunneling effect is illustrated on Fig. 3.7. The electron, which has wavefunction ψ , comes from the left (only one dimension is considered). The amplitude of the oscillations falls exponentially within the barrier (shaded area, left), because the

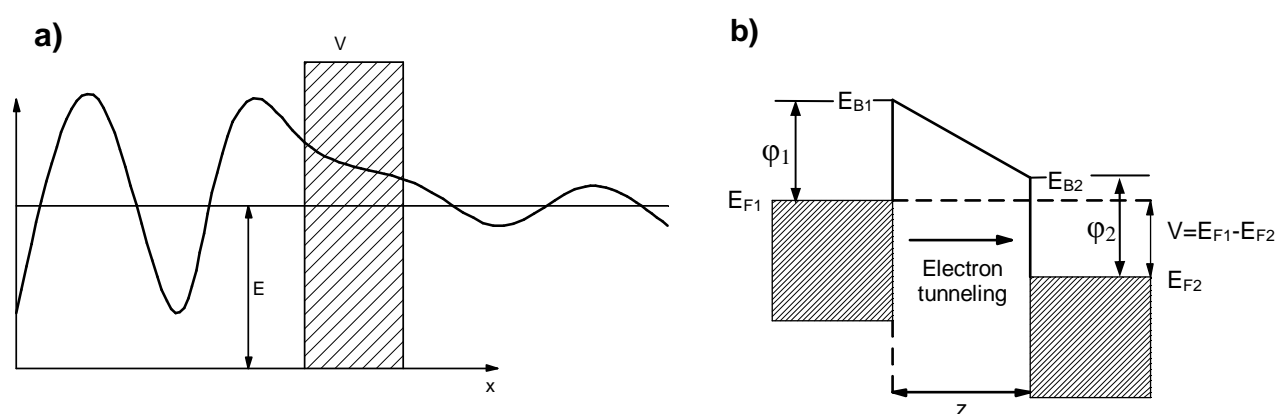


Fig. 3.7 Illustration of tunneling effect: decrease of the wavefunction (a) and energy diagram for the metal-metal STM junction (b), E_F – Fermi level, E_B – height of barrier, z – distance between tip and sample, V – applied bias voltage, ϕ – workfunction; $\phi_1 \neq \phi_2$ in general.

energy of an electron E is lower than the height of the barrier V . If the barrier has finite thickness then ψ will not go to zero on the right side and oscillations will continue. This means that the probability to find an electron on the other side of the barrier is not zero – the electron can tunnel through the barrier.

In order to describe the tunneling effect quantitatively one has to consider the three dimensional theory in detail. The fluctuation theory for tunnel contact, developed originally by Barden [67] and improved by Tersoff and Hamann [68], gives the following expression for the tunnel current:

$$I = e \cdot \left(\frac{2\pi}{\hbar} \right) \sum_{i,f} (f(E_f) - f(E_i)) |M_{if}|^2 \delta(E_f + V - E_i) \quad (3.16)$$

Here ψ_i and ψ_f are the wavefunctions of the initial and final state of the electron under consideration, M_{if} is the tunnelling matrix element between initial and final states, E_i and E_f are the corresponding energies respectively, $f(E)$ is Fermi-Dirac distribution, V is the height of potential barrier and e the is charge of electron. The initial state of the electron can be its state in the tip and the final one is in the surface if the negative potential is applied to the tip (and vice versa depending on the bias voltage applied). The wavefunctions are defined for the tip and the surface when they are considered separately i.e. without tunneling transition. They can describe the tunneling transition properly only if the distance between both parts of the entire system is large (and applied potential difference is low). If it is not the case and the interaction between the tip and the surface are significant, one cannot use two independent wavefunctions ψ_i and ψ_f to describe the system. The expression for the tunneling current can be simplified if we assume that: 1) the apex of the tunneling tip has an ideal spherical shape; 2) only s-wavefunctions of the atoms in the tip take part in the electron transition. Then it takes the form [68]:

$$I = \frac{32\pi^3 e^2 V \varphi^2 D_i(E_F) R^2}{\hbar k^4} \exp(2\kappa R) \sum_f |\psi_f|^2 \delta(E_f - E_F) \quad (3.17)$$

where D_i is the density of states for the tip, E_F is Fermi energy, R is the radius of the apex, d is the distance between apex and surface and $\kappa = \hbar^{-1}(2m\varphi)^{1/2}$ is the minimum inverse decay length for the wave functions in vacuum (φ is the work function). The last exponent

represents the local density of states on the surface at the Fermi level at the point closest to the apex. So it is shown that the probability of the tunnel transition depends on the distance between the tip and substrate exponentially.

Not all assumptions of the model described above are completely correct for the real STM experiment. For example, an image with atomic resolution cannot be explained if the electrons are transferred only through s-electrons. But the model, which takes into account p, d and f-orbitals, is much more complicated and it will not be considered here. For detailed information the reviews [69-71] are available.

3.2.2 Measurement modes

As one can see from equation (3.17) the tunneling current depends mainly on the distance between the tip and the surface; the density of states of both tip and substrate plays a secondary role. If we assume that the distribution of the electronic density of states in the tip is continuous, the picture resulting from an STM experiment will represent the electronic density of the surface. For objects in the micro- and nanometer scale this picture corresponds to the geometrical shape very well. This means that the usual interpretation of STM images as topographic maps is correct for most cases.

There are two ordinary methods of acquisition of STM images. They are shown schematically in Fig. 3.8. The first one is known as constant current mode: the feedback electronics of the microscope keeps the tunneling current constant during the scan of the surface in X- and Y-directions. In order to reach that, the vertical position (Z) of the tip is continuously adjusted. The Z-coordinate is recorded as a function of X and Y and these data are used to construct the STM image. The tunneling current can be kept constant if the scan speed is not high, because the reaction time of the feedback electronics is not infinitely short.

The second possibility is the constant height mode. Here the vertical position of the tip is not changed and the tunneling current will be recorded. One obtains a similar image as a result. This method is not used often because of one important restriction: the surface must be very flat, in order not to short circuit during the scan. The tip will be damaged with high probability in the case of direct mechanical contact with the surface.

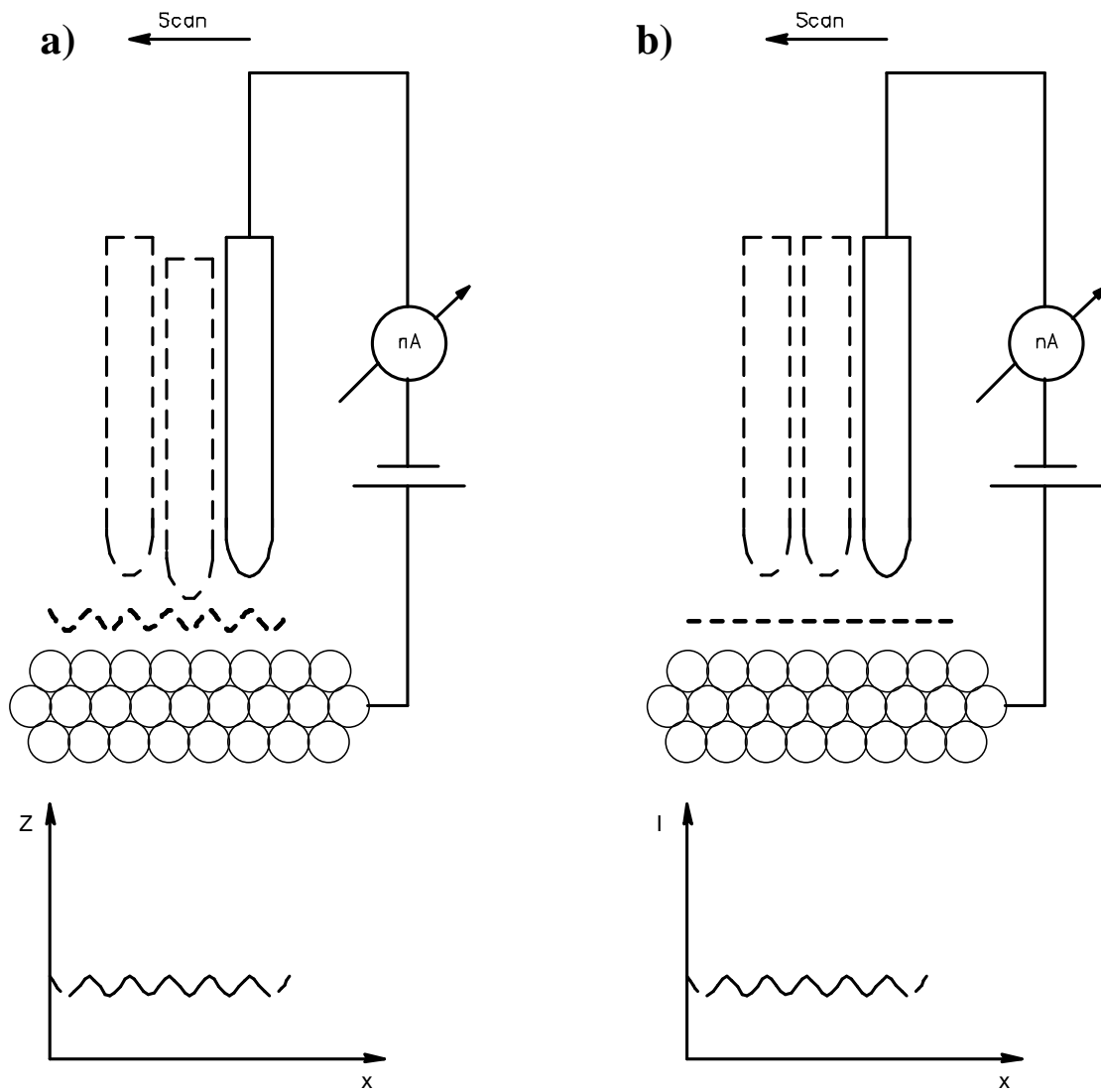


Fig. 3.6 Two modi used in scanning tunneling microscopy: a) constant current mode; b) constant height mode.

The advantages of the constant height mode are higher scan speed and better quality of images on an atomic scale.

Chapter 4.

Experimental detail, data analysis and error discussion

4.1 Preparation of samples; measurement cell

The reliable measurements of the properties of SF films require special accuracy on every step of experiment beginning with the sample preparation. Only very pure components are suitable for the manufacturing of the alloys, because most of the impurities have a tendency to be concentrated on the surface. Therefore only pure metals i.e. Ga, Bi and Pb (99,9999% purchased from Alfa Chemicals) were used in this study. The purities of the main components refer only to metallic impurities but not to oxides and hydroxides, so a primary purification was required. For Ga this was done by slow flowing of the liquid metal through a glass capillary. The oxide impurities, which have a lower surface tension, remain on the surface and stick to the glass wall. The procedure was performed in a special glow-box, filled with Ar and isolated from the atmosphere (concentration of O₂ and H₂O is about 1ppm). In the case of Bi and Pb, which have greater melting temperatures, a similar procedure was done in a quartz vessel under vacuum ($p \approx 10^{-5}$ mbar). The metals were placed in a glass syringe and heated by means of high-frequency induction furnace up to the melting point. Then they flowed into the container, mounted below, and solidified there. Afterwards the metals were transferred into the glow-box. The pure components, prepared in such a way, can be stored in Ar atmosphere for a longer time without significant oxidation.

For the preparation of the alloy the required amount of liquid Ga was placed into the crucible (see below) with the help of a glass syringe. Then the exact mass of Ga was

determined by means of weighting (precision $\pm 0.0001\text{g}$). The mass of Bi or Pb was calculated for the desired concentration; small pieces can be cleaved with the help of pincers – they were to be weighted and added to liquid Ga. The crucible was cooled down to approx. -20°C in order to solidify the metal and transferred on air into the chamber for the subsequent cleaning of the surface. This step was necessary to remove large visible particles of impurities, which appear in spite of all precautions, described above.

The cleaning chamber was equipped with a resistance furnace, which was able to heat the sample up to 500°C , an Ar sputter-gun and a wobble-stick manipulator with an electrically heated tungsten wire. The pumping system of the cleaning chamber, consisting of roughing pump and turbomolecular pump, allows to achieve a pressure of 10^{-7} mbar within 24 hours without complicated and time-consuming bakeout. Such a vacuum can be also obtained faster with the help of a liquid nitrogen trap. After reaching of the vacuum level mentioned above the sample was heated up to some 250°C and held at this temperature during 1.5 - 2 hours in order to dissolve Bi (or Pb) in Ga completely.

The cleaning of the sample was started by bombardment of the surface with accelerated Ar^+ ions, generated in a sputter-gun. A typical ion current consisted of 25-35 μA . A few minutes of sputtering were enough to break the oxide layer, which originally covered the whole surface, into many small particles. It was not possible to achieve complete removal of all impurities in such a way in reasonable time and without evaporation of too much of metal.

In the second step the tungsten wire (from Goodfellow) was employed. The U-shaped wire ($\varnothing=0.5\text{mm}$) was first annealed at about 1500°C . Then its temperature was reduced to some 400°C and the wire was brought in touch with the metal in the crucible. After the wetting of the wire by the alloy part of the impurities stick to the wire. This effect is described in the work of [72]. The optimal temperature and the shape of the wire were found experimentally. Afterwards, the manipulator with wire was moved to the cylindrical extension of the main chamber. This extension can be separated from the main chamber by means of vertically driven shields. The temperature of the wire was increased to $\sim 1500^\circ\text{C}$ for some 5 seconds to allow complete evaporation of the material collected on the wire. This procedure was repeated several times until total removal of visible particles. Additional visual check of the surface was performed with a CCD-camera with 5x zoom. When the surface seemed to be absolutely clean the heating and the sputter-gun were shut down, followed by cooling of the sample. In order to minimize the oxidation of the metal during subsequent transportation to the Omicron apparatus the alloy must be

solid in order to reduce the solubility of impurities. For Ga-Bi system the alloy solidified at room temperature, whereas Ga-Pb alloys required some -20°C for solidification due to supercooling. This was reached by cooling of the cleaning chamber vessel with liquid nitrogen. The transportation of the sample to the Omicron apparatus on air took about 5 minutes. The sample was placed into the entry-lock, evacuated during ≈ 40 min. and transferred in the preparation chamber (see description of the Omicron apparatus below). The last step was the sputtering of the sample in the preparation chamber. A few monolayers of oxidized material were removed together with molecules of adsorbed gases.

The quality of the surface was finally checked with XPS. Usually no signals with exception of the elements of the alloy were found in the spectrum.

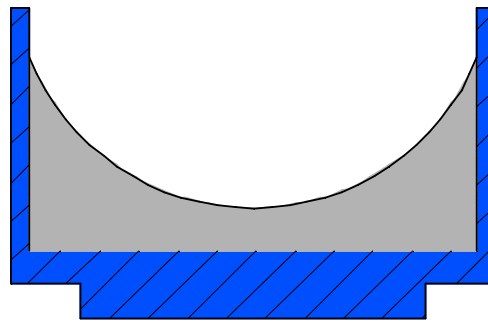
During the experiments that took sometimes more than one month the elementary composition of the surface was regularly checked. It was shown that the concentration of adsorbed oxygen (as main impurity) increases with time even under UHV condition (10^{-10} mbar). When the signal of oxygen was significantly higher than the noise level and/or visible impurities appeared, a new cleaning procedure after transfer to the cleaning chamber was performed.

A series of samples were prepared for some auxiliary experiments. Since they were solid there was no need of cleaning with tungsten wire. A quartz plate (10x10 mm, 1 mm thick) covered by uniform Au layer (thickness 200-300 nm, Berliner Glass) was placed in a quartz tube; a small container, filled with pure Bi was placed nearby. The subsequent evacuation of the tube and heating of the container resulted in the evaporation of Bi followed by its precipitation on the Au layer. The distance between the Bi container and plate was large enough to allow uniform coverage of the plate. Then this plate was fixed in a sample holder and used in depth profiling experiments after cleaning of the surface with sputter-gun. For the calibration and fine focusing of the Auger electron gun the plate was prepared in a similar way: it was covered by a mask with stripes and squares of known dimensions. After removal of the mask only a part of the surface was covered by a Bi layer.

Also a steel plate covered with magnesium oxide (prepared by holding the plate above burning Mg on air) was used for fluorescence in the electron beam. Samples with solid Ga, Bi and Pb were prepared by pressing of corresponding metals into the cavity in the sample plate.

Two types of crucibles made of molybdenum were used in this study (see Fig. 4.1). The first one has a simple cylindrical shape (height = 7 mm, inner diameter = 13 mm, outer diameter = 14 mm). The relatively small size of the crucible was determined by the dimensions of the sample holders of the Omicron chamber. The amount of alloy placed inside the crucible was about 40% of its total volume (this corresponds to a cylinder of 3 mm height for the hypothetical situation of the contact angle alloy-molybdenum-vapour is exactly 90°). At perfect wetting this amount could lead to floating

a)



b)

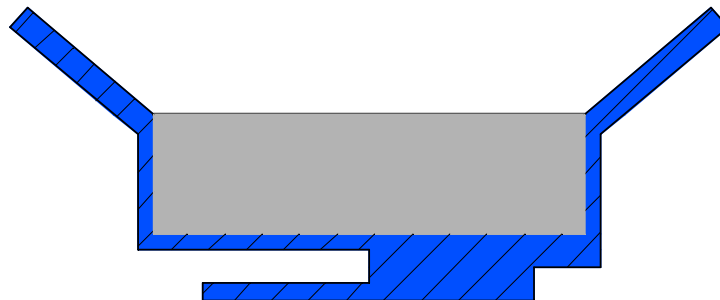


Fig. 4.1 Two types of crucibles used in this study: a) cylindrical crucible. Due to the wetting of the walls by the liquid alloy the liquid-vapour interface becomes concave from above after a while. b) funnel-shaped crucible with flat liquid-vapour interface. Boring in the bottom of the crucible (b) used for temperature measurements.

of the liquid alloy over the crucible walls, what could result in serious problems in the measuring setup. Molybdenum was chosen as material for the crucibles because of its inertness to alloy components in a wide range of temperatures. Additionally, it was shown, that several subsequent cleaning procedures do not affect the concentration of the alloy. Moreover, the amount of alloy does not change significantly. The crucible was fixed in a stainless steel plate specially designed for the transportation of the sample within the Omicron apparatus.

Despite of the relative simplicity of the construction, the crucible described above appeared not to be optimal for spectroscopic and STM measurements. The following disadvantages were found during several trails:

- The wetting of the crucible walls during cleaning increased continuously that can be explained by removal of oxides from the Mo container during sputtering. Finally the liquid alloy interface became concave from above with almost complete wetting of inner walls of the crucible. For different samples the interface was similar, but not identical – this results in slight differences at quantitative evaluation of XPS and AES spectra.
- Because the X-ray source and the electron gun are not located directly above the crucible (see next chapter), the walls of the crucible cast a shadow on the interface. That means the analysis of the entire surface was not possible.
- In STM experiment the relative position of the tip above the surface was not visible. This increased the time required for the approach.
- The temperature of the alloy was unknown. It can be only estimated from the reading of the thermocouple mounted on the manipulator near the heating element. A series of experiments on Ga-Bi alloys with various concentration of Bi exhibits that respective surface freezing temperatures can be reproduced by this thermocouple more or less well (see also Ch. 4.2).

All those drawbacks were eliminated in the second version of the crucible (Fig. 4.1b). The amount of material in the crucible was kept constant; a crucible together with a sample plate was machined from a single piece of molybdenum. When the cleaning procedure was conducted carefully the edges of the liquid interface lie exactly on the top of a cylindrical part of the crucible i.e. the inclined side of the funnel was not wet. A practically planar and shadow free interface was achieved in this crucible.

A boring ($\varnothing = 1\text{mm}$) in the bottom of the crucible was utilized to the temperature measurements. An additional thermocouple was installed in the analysis chamber replacing one of spare blind flange with feed-through (see Ch. 4.2).

4.2 Overview of the Omicron UHV unit including XPS, AES, UPS and STM techniques

For the investigation of the alloy surface the commercially available Multiprobe P system supplied by Omicron Nanotechnologies was utilized. A schematic overview of the apparatus is shown in Fig. 4.2. It consists of three parts, connected to each other: Fast Entry Lock (FEL) chamber (I), preparation chamber (II) and analysis chamber (III). All chambers have their own pumping stages. They are separated by manually operated gate valves (1) that allow independent pumping.

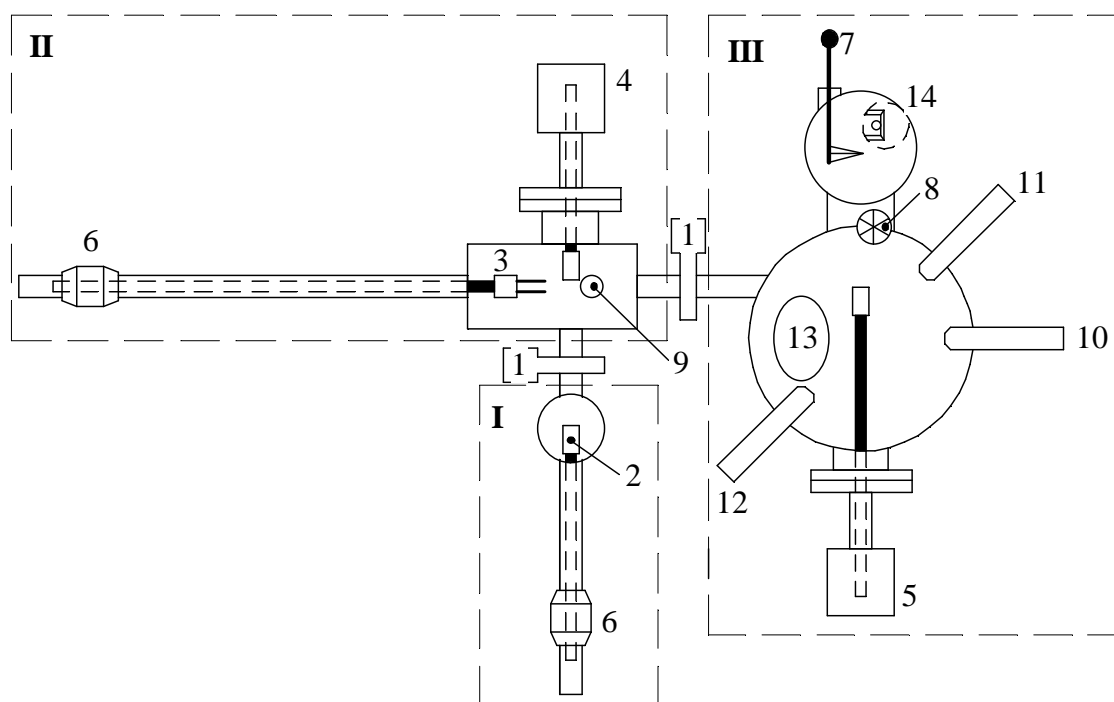


Fig. 4.2 Top view of the Omicron Multiprobe P apparatus. It consist of three chamber (I – Fast entry lock, II – Preparation chamber, III – Analysis chamber) separated with manual valves (1). Following parts are depicted with numbers: 2 – probe transporter, 3 – linear transfer head, 4, 5 – high precision manipulators, 6 – magnets for linear transfer and rotation, 7 – pincer grip wobble stick, 8 – revolver storage, 9 – Ar sputter gun, 10 – X-ray tube, 11 – e-gun, 12 – UV lamp, 13 – flange for electron analyser (not shown).

Samples and STM tips are loaded through the CF63 port on the FEL chamber. A probe transporter (2) carries the sample from the sample acceptance stage to the sample transfer head (3), which is used for further transportation of the sample to manipulators (4 and 5) in the preparation and analysis chamber, respectively. Both probe transporter and sample transfer head can be rotated and linearly moved using magnets (6). Once a sample is landed on the manipulator it can be moved in 3 dimensions with sub-millimetre precision and rotated around the axis of the manipulator. For the transfer of samples (and tip holders) to the tunnelling microscope a pincer grip wobble stick (7) is used. There is also a possibility to keep up to 6 samples in the analytical chamber simultaneously by means of revolver storage (8). Preparation chamber is equipped with the Ar⁺-ion sputter gun (9) mounted on the upper side of the chamber. The sputter gun generates an ion beam of variable intensity used for the sample surface cleaning. Radiation sources for the XPS (10), AES (11) and UPS (12) are located in the analysis chamber as well as the electron analyser (it is not shown explicitly in the Fig 4.2 due to large dimensions). The electron analyser is attached to the analysis chamber through CF100 flange (13). The tunnelling microscope (14) is mounted in separate vessel attached to the analysis chamber.

The FEL chamber makes it possible to introduce and to remove samples without ventilation of the main chambers. The relatively small volume of the FEL chamber allows fast pumping and therefore a pressure of 10^{-6} mbar can be reached within some 30 minutes. During the transfer the valve between FEL and preparation chamber must be open. In this way vacuum in the preparation chamber is spoiled from typically $10^{-9} - 10^{-10}$ mbar to 10^{-7} mbar for a short time, but it recovers fast when the valve is closed. The scheme of the pumping system of the apparatus is shown in Fig. 4.3.

In the preparation chamber the sample is subjected to final cleaning procedures, which are carried out by means of the Ar⁺-ion sputter gun. During the sputtering a thin layer of adsorbed atmosphere gases (O₂, CO₂, H₂O) and metal oxides are removed from the surface. The sample prepared in this manner has an atomically clean surface, so it is ready for ES and STM experiments.

The construction of the manipulator head is shown in Fig. 4.4. It consists of the massive molybdenum holder with rails (1) for the insertion of the sample plate. A resistance furnace (2) with ceramic insulation is located between the rails, direct under the sample plate. It is connected to DC power supply through the terminals (3). A temperature range up to 650K is available for this setup. It can be measured with two

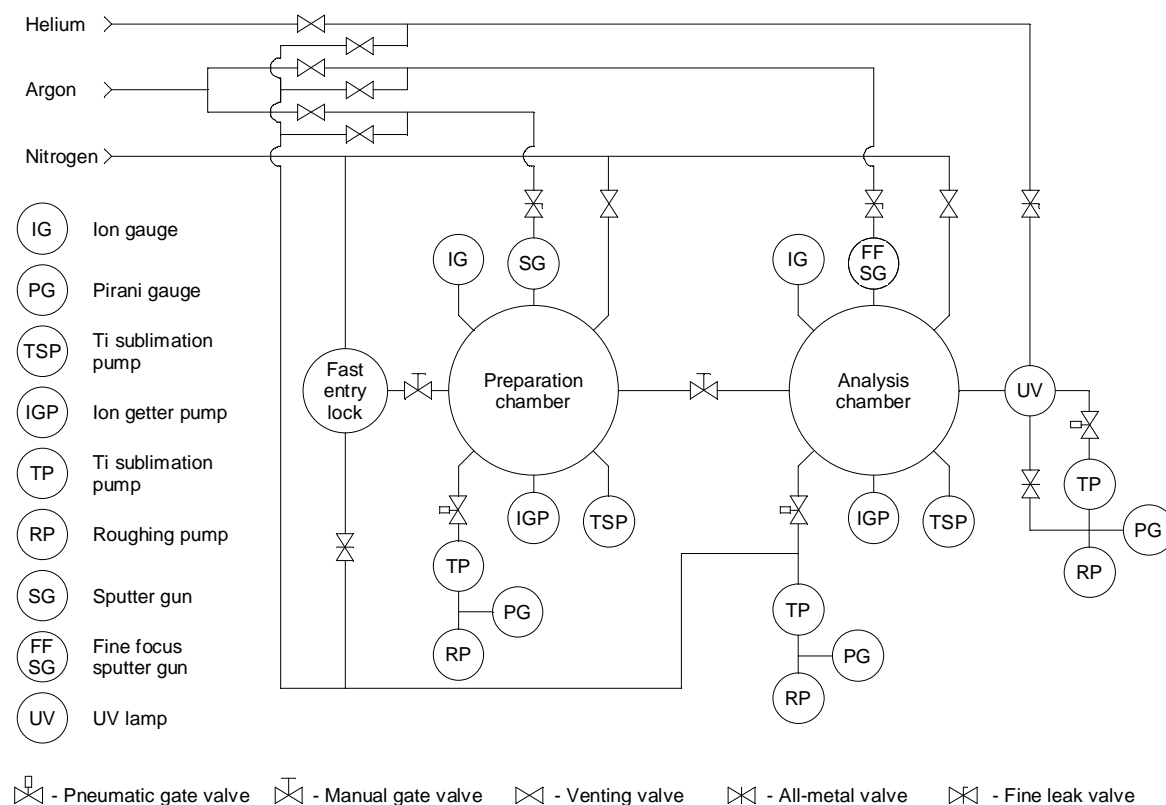


Fig. 4.3 Scheme of the gas supply and pumping system of the Omicron Multiprobe P apparatus.

thermocouples (4) and (5). Practically only the thermocouple (4) was used, because it displays a relevant temperature of the holder frame near by the crucible and the heater. The manipulator head is mounted on the stainless steel rod (8); ceramic ring (9) provides proper insulation of the head from the ground.

A cooling system consists of the reservoir (6) and a massive copper braid (7). Strongly cooled gaseous or liquid nitrogen was used as coolant. The reservoir and the braid provide very effective thermal exchange, allowing to reach the temperature of the crucible till $\sim 150\text{K}$. The primary purpose of the cooling system is to solidify the liquid alloy in order to prevent possible leaks during transportation within the UHV apparatus.

The original Omicron setup did not allow measuring the temperature inside the crucible; it could only be estimated roughly from the thermocouple mounted on the rails of the manipulator. Therefore an additional thermocouple was attached to the analysis chamber. As the crucible is set on the manipulator, the thermocouple tip can be inserted into the boring in the bottom of the crucible. The thermocouple for the

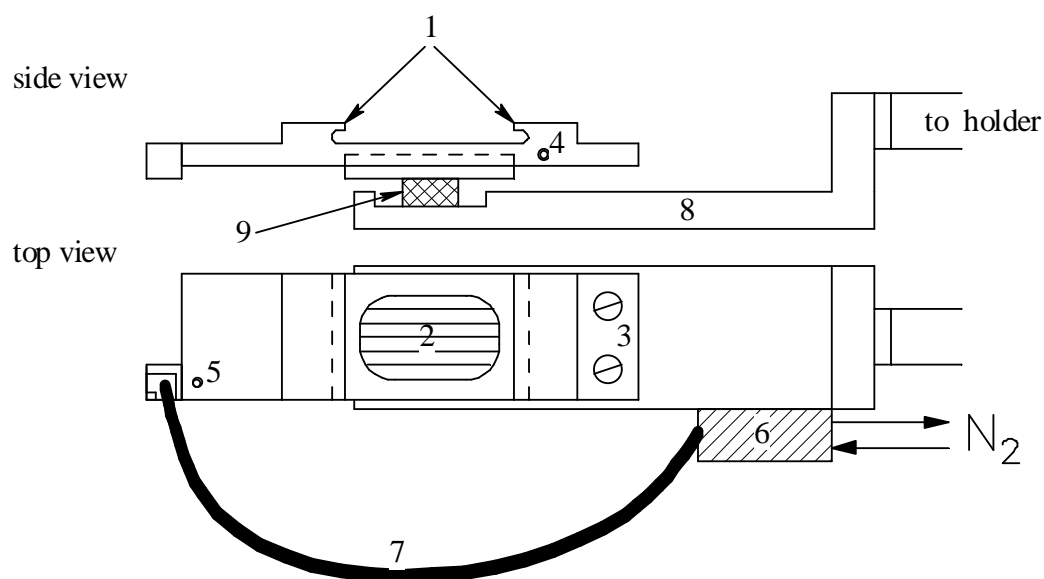


Fig. 4.4 Manipulator head in preparation and analysis chambers. Side and top view. 1 – molybdenum holder with guiding rails for sample plate or crucible, 2 – heating element in ceramic insulation, 3 – terminals for DC supply, 4, 5 – thermocouples, 6 – heat exchange reservoir, 7 – massive copper braid for heat exchange between reservoir and sample holder, 8 – stainless steel rod connecting the head to the holder, 9 – ceramic insulation.

crucible as well as the cooling system were assembled and tested in the laboratory of the institute.

4.3. Electronic spectra measurements

In order to get reliable and reproducible electron spectra of Ga-Bi and Ga-Pb bulk-vapour interfaces some peculiarities should be taken into account.

An electric charge on the sample affects the kinetic energies of outgoing electrons. Continuous bombardment of the sample by accelerated electrons or X-rays leads to the growth of electric charge on the sample when it is not connected to earth. This may result in a shift of the entire spectrum to higher kinetic energy (lower binding energy). Therefore correct spectra can be measured only if the analysed material is properly grounded. This was done by connection of one of the two wires of the resistance heater to the ground. The heater has an electrical contact to the sample holder; DC power supply was used.

The appropriate reproducibility of the intensities in XPS and AES spectra can be achieved only if the sources provide constant, time-independent flux of electrons/X-rays. Practically this means that one should switch on the source some 2-3 hours prior the measurement. Trial acquisition of reference samples showed very good stability of the X-ray tube: the signal level appeared to be constant for many hours (for the peak area of approx. 500 eV*kcts/s the difference is less than 0.5%). The electron gun displays less stable behaviour. Short-time variations (during the acquisition of one spectrum, typically 0.5-3 minutes) were about 3-5%; long-time drift was detected to be even more significant (up to 15% per hour). Fortunately, it was possible to read the electron emission current on the display of power supply unit and to adjust it manually in case of strong deviation. Additionally, the desired accuracy was reached by reduction of the acquisition time and increase of the number of taken spectra.

The yield of the electron detector (the level of the signal per single electron) has changed with time due to the aging of the channeltrons. This happens slowly, but if the interval between single measurements is longer than several months, the yield should be checked (and corrected if necessary), for example, by measurements of reference samples. Their role in this study played the pure metals (Ga, Pb, Bi) placed in standard molybdenum crucibles.

The detected intensity of the peaks should be kept within definite ranges. If it is too low the signal/noise ratio is also low and this results in an increase of the uncertainty of the peak areas (see also chapter 4.5). If the intensity is too high a part of the electrons will not be detected by the channeltrons, i.e. the output of the channeltrons becomes not linear. This factor plays a significant role for intensities greater than 10^6 cts/s per channel. There are several possibilities to control the intensities of the signal: the hemispherical analyser is equipped with a set of adjustable entrance and exit slits that can reduce the electron flux. It can be also done by the regulation of the output power of the electron gun or X-ray tube as well as the regulation of the distance to the sample (possible only for X-ray tube). All those parameters were optimized in the beginning of the experiments and then they were kept without changes in order to provide the same conditions for all ES measurements and to allow the subsequent analysis of the data.

A slightly different wetting of the crucible walls by the alloy can in principle affect the absolute values of the XPS and the AES signals. This increases the relative error of the quantitative analysis and makes it difficult to compare the film thickness for different concentrations. In order to investigate the influence of the interface curvature on

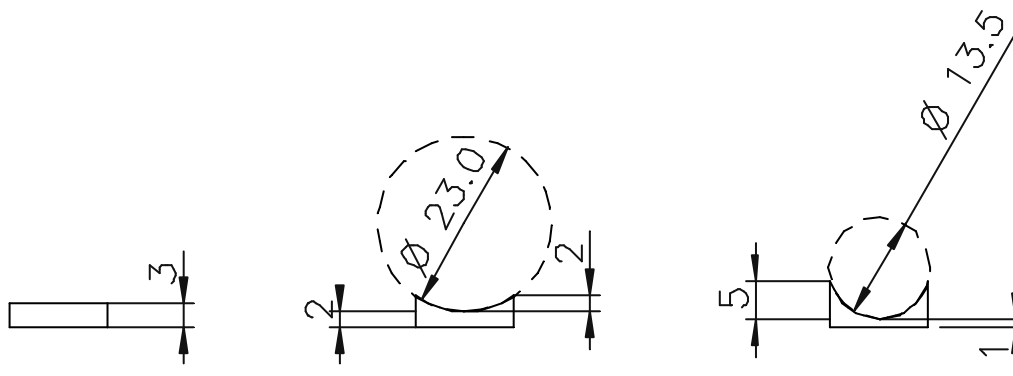


Fig. 4.5 Stainless steel samples used for the modeling of different wetting of the crucible walls. Radii of the curvature: 1 - ∞ (flat surface), 2 - 23mm, 3 - 13.5mm.

the XPS intensity the following experiment was performed: three pieces made of stainless steel were placed in the crucible. The pieces were machined so that their upper side models the different wetting situations (Fig. 4.5), whereas the mass of the pieces was the same. Then the XPS spectra of all three samples were recorded and the area of the Fe $2p_{3/2}$ (780 eV KE) peak was compared. A difference of 4% was found for two extreme cases ($R = \infty$ and $R = 13.5$ mm). With the assumption that the wetting of the crucible walls in Ga-Bi and Ga-Pb systems is similar for all samples, this source of error was considered as negligible.

4.4. STM image acquisition

All STM images in this study were recorded with the help of the variable temperature ($T \leq 650\text{K}$) “Micro SPM H” microscope supplied by Omicron Nanotechnologies. Since the microscope was maintained in the UHV chamber, all manipulations like exchange of samples and tunnelling tips are performed without ventilation of the chamber.

The principle of the construction of the microscope used in this study is shown in Fig 4.6. A sample (1) (crucible with alloy or sample plate) is inserted into the sample holder (2), which is equipped with stepping motors (3). They are used to move the sample in X- and Y-directions. The scanner tube (4) has a small magnet on the lower end, which fixes the tip holder (5). The scanner is connected to preamplifier, control unit and PC.

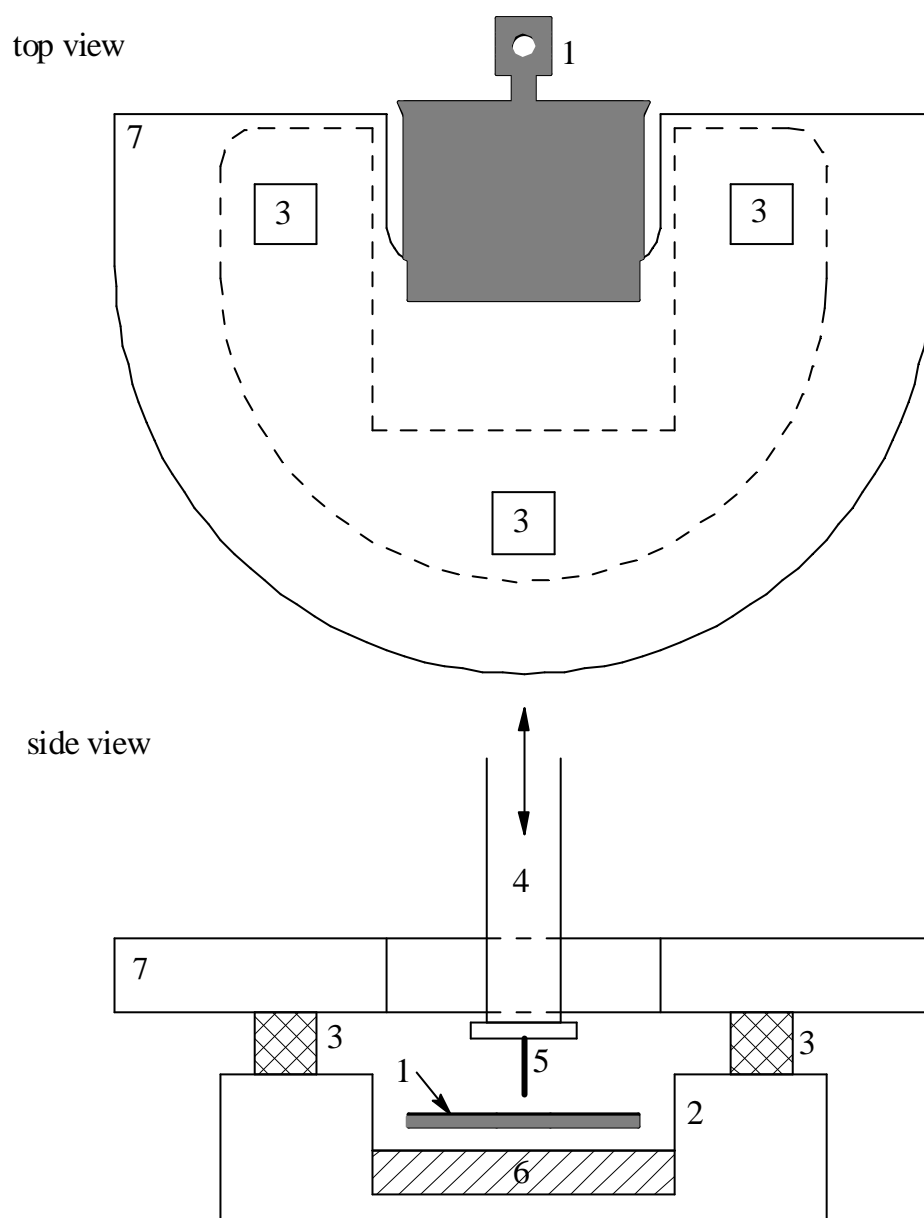


Fig. 4.5 Scheme of the sample stage of Micro SPM H microscope. Top and side view. Vibration isolation elements are not shown. 1 – sample plate, 2 – sample holder, 3 – stepping motors, 4 – scanner tube, 5 – tip holder with tip, 6 – heating element, 7 – massive microscope stage.

It is very important to isolate the sample holder and the scanner from any sort of mechanical vibration originated typically from roughening and turbomolecular pumps, which are located very close to the UHV chamber with the microscope. Usually they should be switched off during the STM acquisition. Another sort of vibration, which can distort the STM images, is the vibration of the floor. Such a phenomenon arises even if

the laboratory is located in the basement of the building. In the case of the Omicron setup special pneumatic legs are used to get rid of the building vibration. They can lift the whole table with the apparatus, so it has no direct contact to the floor. In addition, the floor under Omicron apparatus was separated from the rest of the building. The microscope itself is also equipped with vibration isolating vitone rings.

Before starting the STM measurements, the tip holder with a new tip must be mounted on the scanner. This can be done by the series of manipulations when the special tag with a tip holder is inserted in the microscope. After subsequent replacement of the tag with the sample a two-stage approach of the tip to the surface starts. In the beginning the tip-surface distance can be estimated by eye and the approach is controlled by the experimenter. When the distance becomes small, the automatic, feedback-controlled approach is initialized. It stops when the specified tunnelling current is achieved; then the scanning can be started.

Several parameters can be independently adjusted during the scan in order to increase the quality of STM images: gap voltage, feedback tunnelling current, loop gain, scan speed and scan area. There is no general rule how to optimize them, the “trial-and-error” method is used very often. A two-channel oscilloscope, connected to the control unit of the microscope was utilized to observe two important variables during the scan: actual tunnelling current and tip-surface distance. The analysis of the time dependence of those variables allows to find the suitable set of scan parameters. It also helps to locate the sources of noise.

The thermal expansion of materials drastically affects the images in STM; this phenomenon is known as thermal drift. Practically it appears as a shift or stretch/shrink of the scanned area¹. The best way to get rid of thermal drift is to keep the temperature of the whole setup, including the microscope and the sample at constant level. This was done with the help of air-conditioning in the laboratory, where the deviation of room temperature was kept within one degree.

¹ In principle the Scala Pro STM software used in our experiments provides a possibility to take into account the thermal drift and to correct the recorded images. This option can be used for the correction of linear (time-independent) thermal drift, which is seldom in practice.

4.5. Error analysis

Different sources of errors are considered below. Their influence on the final results i.e. thickness and chemical composition of the films is also described in this chapter. In general, the following sources of error have to be considered: error in concentration of the surface active component (Pb or Bi) in the liquid alloy, error in the measurement of the temperature of the alloy, error of the IMFP, electron analyzer instrumental error and error of XPS or AES peak area. These contributions are considered separately.

Error of concentration. This error is influenced mainly by such factors as precision of the balance, purity of the chemicals used for the sample preparation, peculiarity of the cleaning procedure. Since the purity of metals according to the data of manufacturer is very high, the corresponding error is considered as negligible. ‘‘Sartorius’’ R 160P piezoelectric balance used for the samples preparation allows the weight measurements with a precision of 0.1 mg. The expression for the mole fraction of Bi and corresponding error is given as follows (in case of Ga-Pb error is the same):

$$x_{Bi} = \left(\frac{m_{Bi}}{M_{Bi}} \right) / \left(\frac{m_{Bi}}{M_{Bi}} + \frac{m_{Ga}}{M_{Ga}} \right); \quad \Delta x_{Bi} = \left| \frac{\partial x_{Bi}}{\partial m_{Bi}} \right| \Delta m_{Bi} + \left| \frac{\partial x_{Bi}}{\partial m_{Ga}} \right| \Delta m_{Ga} \quad (4.1)$$

For the most dilute sample ($x(\text{Pb}) = 0.0006$) this expression gives a relative error of 2.5%; for higher concentrations it is less. Cleaning of the sample surface including removal of oxide particles mechanically and by sputtering may theoretically result in depletion of the surface active component in the alloy. This does not happen as one can judge from the fact that the surface freezing temperature was found to be constant after several cleaning procedures. Total concentration error can be therefore estimated to be lower than 3%.

Error of temperature. Temperature measurements were performed with a Ni-NiCr thermocouple with an absolute accuracy of $\pm 0.5\%$ (temperature in K). This means an absolute error of less than 2.5K for the entire temperature interval of the measurements. The temperature of the alloy surface can slightly differ from that in the bottom of the crucible, where it was measured. This difference is much more pronounced in the first version of the crucible, where the measurement point was located on the top of the sample

holder. In the second version of the crucible the temperature gradient seems to be low because of a relative small size of the crucible. Unfortunately one can not be completely sure due to lack of the experimental data concerning temperature gradient. One can estimate the maximal absolute error of 5K for the crucible 1 and around 1K for the crucible 2¹.

Error of IMFP. Inelastic mean free path is a constant for the material, which is used in the analysis of the XPS and AES data. This constant characterizes the interaction of the electrons of specific kinetic energy with atoms of the material. The values used in this study were taken from [73]. IMFPs were calculated from these empirical expressions showing that the root mean square difference between these IMFPs and those initially calculated was 11%. Given values of the IMFP are strictly correct only for ideal, flat surfaces. There are numerous facts in the literature, which prove that the surface of the material usually undergoes so-called surface roughening transition [74-77]. This effect is not strong for pure Bi [75], whereas for Pb it is well known [77]. In addition one should take into account the influence of the aggregate state of the surface on the IMFP through the capillary waves for the liquid surface. The amplitude of the capillary waves depends on the temperature and surface tension [78]. The possibility of the surface roughening as well as difference between solid and liquid surfaces increases the uncertainty of the IMFP.

Error of electron analyzer. According to the user's manual of the EA 125 electron energy analyzer the difference between real electron flux and detected one overcome 1% for count rates above 10^6 cts/s pro channeltron (this corresponds to $7 \cdot 10^6$ cts/s for device), since the channeltrons have specific dead-time. Those count rates were not reached in the experiments; typical count rate was not higher than $1.5 \cdot 10^6$ cts/s. Furthermore, the peak intensities of the references and studied samples usually have the same order of magnitude. Therefore the electron analyzer error is considered as negligible.

Error of XPS and AES peak area. The higher is the measured XPS or AES peak intensity, the larger is the corresponding signal-to-noise ratio. As it is mentioned in Ch. 4.3, the noise level of the X-ray source was much lower than that for the electron gun. Therefore the absolute error of the XPS peak area was found to be less than $2 \text{ eV} \cdot \text{kcts/s}$. This corresponds, for example, to the relative error of 3% for the peak with an area of 70

¹ With exception of particular measurements, where the thermocouple rod was deformed. This affected the thermal contact resulting in the lower temperature values in comparison the measurements with the proper thermocouple.

eV*kcts/s, for larger peaks it is certainly smaller. AES spectra are characterized by the relative error of the peak area up to 15%.

Additional source of error is background correction in the XPS and AES spectra. However, the influence of both peak area and background correction errors on the film thickness d is reduced, since the expressions for d contain always a ratio of the measured intensity to standard one, i.e. (I/I^0) .

Another source, which can affect the ES results, is different wetting of the crucible walls for standards (pure metals) and alloys, which results in slightly different surface profile. The influence of the wetting of the walls was reduced in the second version of the crucible (see also Ch. 4.1)

Total error can be calculated by Gauss' formula. For example, the error of the film thickness d , according to the overlayer model (eq. 3.9) depends on the error of two variables as follows:

$$\Delta d = \left| \frac{\partial d}{\partial \lambda_A} \right| \Delta \lambda_A + \left| \frac{\partial d}{\partial (I_A / I_A^0)} \right| \Delta (I_A / I_A^0) \quad (4.2)$$

The quantitative characterization of the film thickness becomes difficult, when $d > 3\lambda$ (or approximately 85 Å). In this case less than 5% of the signal comes from the bulk component, which is comparable to the error of λ and XPS measurements.

Error of the interatomic distances in the STM measurements results from two factors: resolution of the STM images and thermal drift of the sample under investigation. Images shown in this study were recorded with a maximum resolution of 400x400 pixels. This corresponds to maximal uncertainty of approximately 5 nm for the image of 2x2 μm size. For the STM images with atomic resolution (5x5 nm) the uncertainty is less than 0.125 Å. The influence of the thermal drift was taken into account by measuring of the interatomic distance in three different directions for the hexagonal orientation. The standard deviation of the distance from one considered atom to the next neighbour can be used for the characterization of the thermal drift. The vertical resolution of the STM scanner is 0.02 Å as given by manufacturer. So the height of terraces can be defined with this accuracy. The uncertainty in the depth of pits and grooves (see also Ch. 5.4) is much larger, because of relatively small dimensions of these objects¹.

¹ If the apex of the tip is larger than the width of the structure under study (groove or pit) one can not exclude the possibility of the tunnelling contact between the sides of the tip and the substrate. This makes apparent depth smaller than it is in reality.

Chapter 5.

Results

5.1 Wetting films in Ga-Bi and Ga-Pb systems

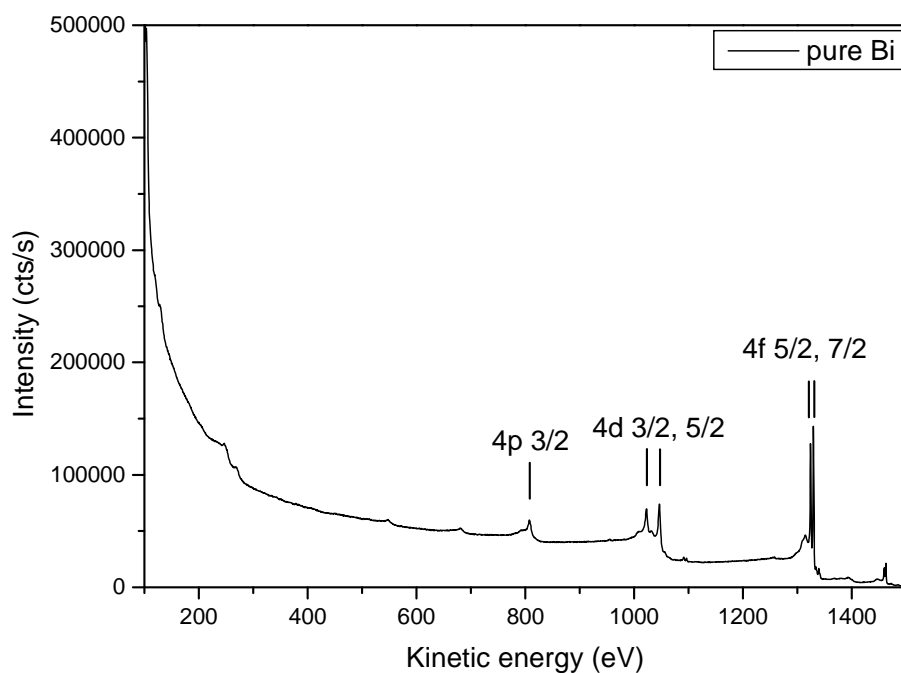
We start the presentation of the results with the characterization of the wetting films by means of X-ray photoelectron spectroscopy. The behaviour of the Ga-Bi and Ga-Pb systems for the concentration range between the eutectic and the monotectic points, i.e. $0.0022 < x_{\text{Bi}} < 0.085$, $302.6 < T(\text{K}) < 495.2$ and $0.0006 < x_{\text{Pb}} < 0.024$, $302.6 < T(\text{K}) < 588.0$ is described in this chapter. The considered temperature range starts nearly from the corresponding melting point and extends 100-150K above it. The XPS data for the alloys with different concentration of Bi as well as those for pure components are interpreted in terms of the overlayer model in order to obtain the effective film thickness [79]. Appendix A contains primary information concerning all XPS experiments performed in this study.

5.1.1 Ga-Bi

For the wetting film study in the Ga-Bi system the crucible of type I (cylindrical shape, curved interface) was used. In total five samples with the mole fraction of Bi 0.0028, 0.0031, 0.0112, 0.0115 and 0.0472 as well as pure Bi and Ga were investigated. The conditions for the XPS spectra acquisition were as follows: relative position of the sample holder in the analysis chamber (X/Y/Z): 14/140/5, EA entrance slit: 6x12 mm, EA

exit slit: 5x11 mm, 7 channel acquisition, position of the X-ray source according to the scale on the X-ray tube: 37 mm, X-ray source: Mg anode, $K\alpha$ radiation, 1486.6 eV, power: 255W (15kV x 17mA). All data concerning the kinetic energy of XPS transitions are related to the energy of the source given above.

a)



b)

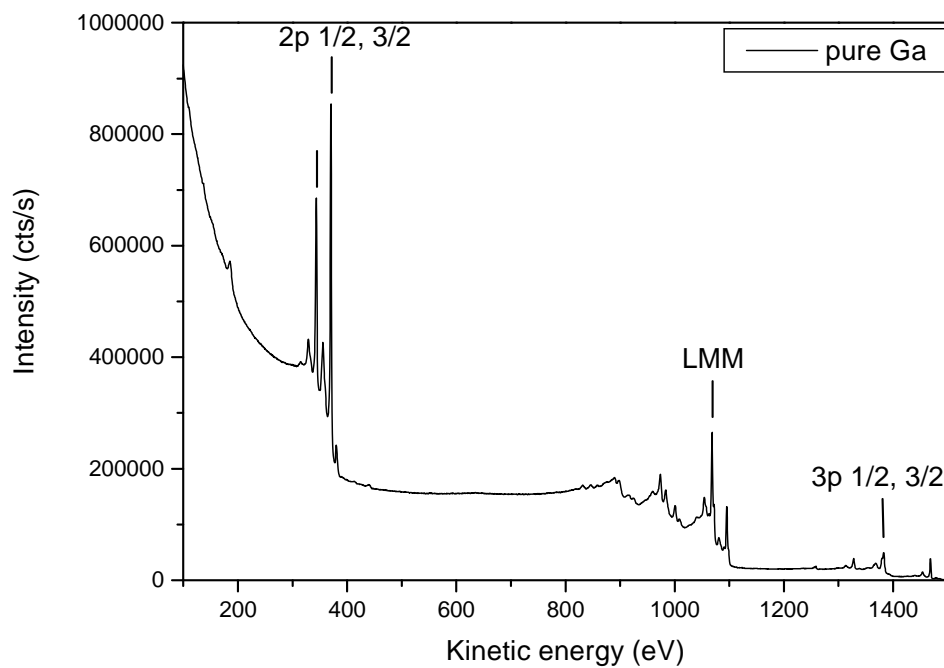


Fig. 5.1 XPS spectra of pure Bi (a) and Ga (b) at room temperature.

Fig. 5.1 shows the XPS spectra of pure Ga and Bi. Both spectra are very similar to those, which were measured by other authors [80, 81]. The characteristic background due to secondary electrons can be observed at low kinetic energies. The acquisition of the spectra for the pure components is vitally important for two reasons:

- to receive I^0 intensities for the quantitative analysis.
- to make sure that the alloy under investigation does not contain any impurities, which can affect the formation of the wetting film.

The most intense peak in case of Ga is the $2p_{3/2}$ transition with kinetic energy of 370 eV. The $3p_{1/2}$ and $3p_{3/2}$ transitions with corresponding energies of 1379 eV and 1383 eV are not so intense, furthermore they partially overlap each other.

Bi has numerous XPS transitions in a wide range of kinetic energy. The maximum intensity has the $4f_{7/2}$ peak at 1329.6 eV.

The spectrum of Ga exhibits a series of signals from 800 to 1100 eV, which can not be identified as XPS transitions. The kinetic energy of these peaks remains constant when the energy of the incident radiation is changed. This implies that they represent different Auger transitions.

In the beginning of the experiments the choice between Mg and Al anodes as the radiation source for all measurements was made in favour of Mg: in this case the Ga Auger series does not overlap with other signals in the spectrum.

In this and all subsequent studies the amount of oxygen, as the main impurity on the surface, was checked at regular intervals. A typical fragment of the spectrum for oxygen check is shown in Fig 5.2. The oxygen peak of maximum intensity is supposed to be found at 955.6 eV [82]. The sample was subjected to a cleaning procedure (see Ch. 4.1) when this signal became significant (dashed and dotted lines) and/or visible particles appeared on the surface. A small amount of oxygen in form of oxides is believed to be adsorbed at the interface between the bulk alloy and the walls of the crucible. It can come to the surface by means of diffusion when the bulk is liquid. The second way is the adsorption from the gas phase. This was observed, for example, when the sample was kept for several weeks in the UHV chamber, even at very low pressure ($\sim 10^{-10}$ mbar).

One can discriminate between physi- and chemisorption if the exact kinetic energy of the oxygen peak can be determined. The deviation of the peak from 955.6 eV to higher kinetic energy reveals the presence of oxides [62].

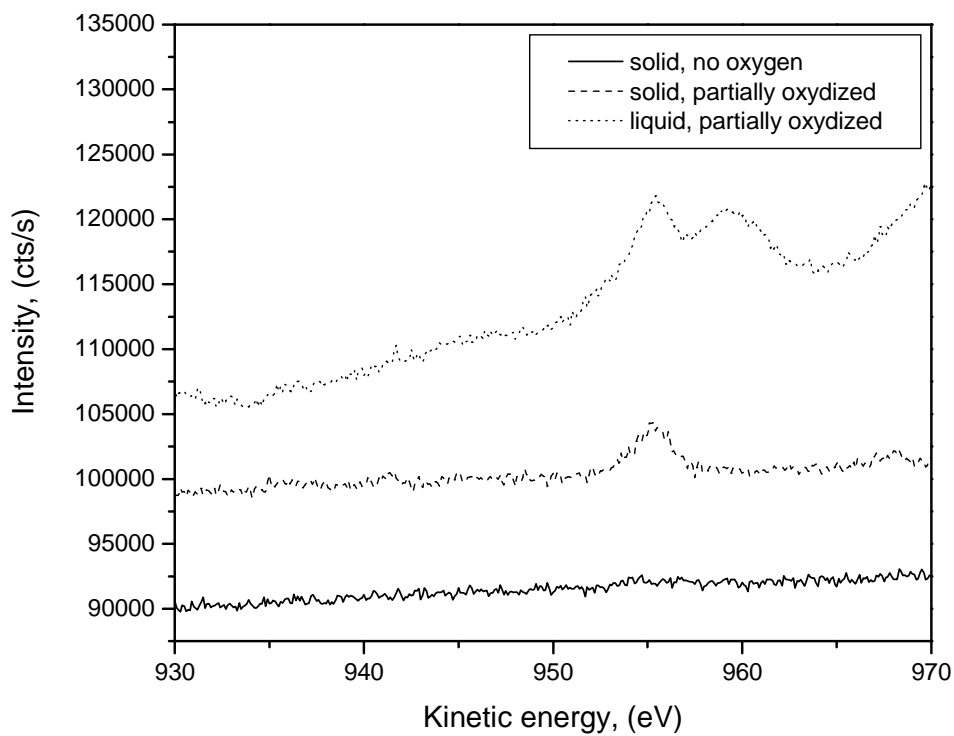


Fig. 5.2 XPS spectrum used for the oxygen check.

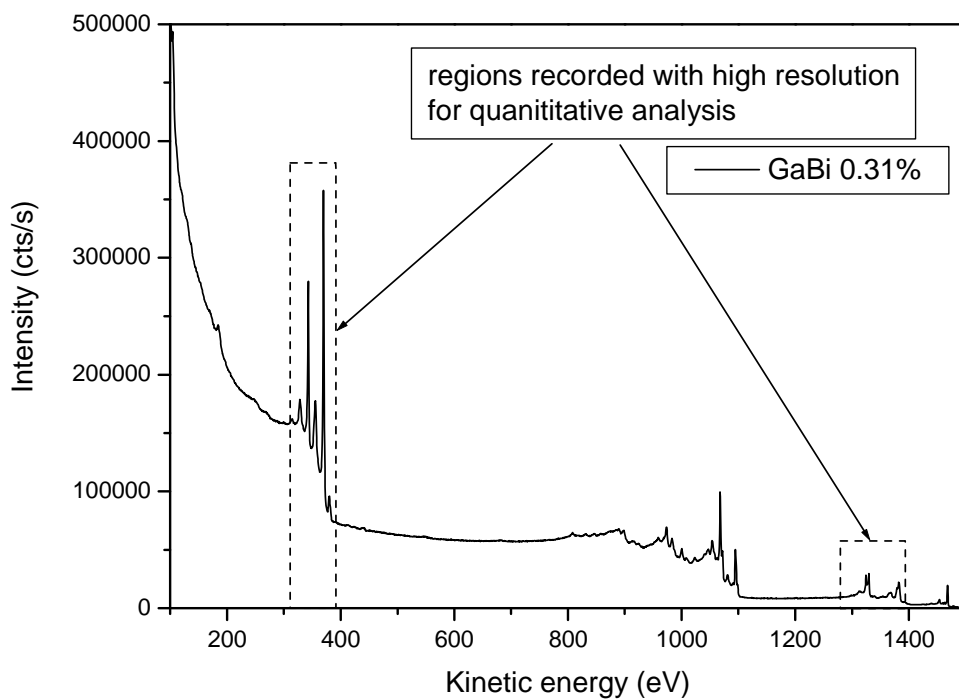


Fig. 5.3 XPS spectrum of Ga-Bi liquid alloy. $x(\text{Bi}) = 0.0031$, $T=170^\circ\text{C}$.

As we already mentioned in Ch. 3.1 the absolute values of the XPS signals can be reproduced very well. Therefore only one spectrum is normally shown. In practice the measurements were performed usually several times.

The spectrum of the wetting film for the liquid alloy ($x_{\text{Bi}}=0.0031$ $T=130^\circ\text{C}$ i.e. $\sim 65^\circ\text{C}$ above the SF temperature) is presented in Fig. 5.3. It appears to be a combination of the spectra for the pure components. Since the absolute intensities of the corresponding Ga and Bi peaks are relevant for quantitative analysis, only the narrow regions shown in Fig 5.3 were recorded with high resolution ($\Delta E=0.1$ eV, dwell time = 0.4 sec.). These spectra for different temperatures were used to determine the wetting film thickness according to the overlayer model.

Fig 5.4 represents the dependence of the wetting film thickness as a function of temperature for different Bi concentrations. The value of d was obtained by solution of eq. 5.1, derived for the overlayer model (see eq. 3.9 and 3.10 in Ch. 3):

$$\frac{I(\text{Bi})/I^0(\text{Bi})}{I(\text{Ga})/I^0(\text{Ga})} = \left(1 - \exp\left(-\frac{d}{\lambda_{\text{Bi}}(E_{\text{Bi}})\cos\theta}\right) \right) \cdot \exp\left(\frac{d}{\lambda_{\text{Bi}}(E_{\text{Ga}})\cos\theta}\right) \quad (5.1)$$

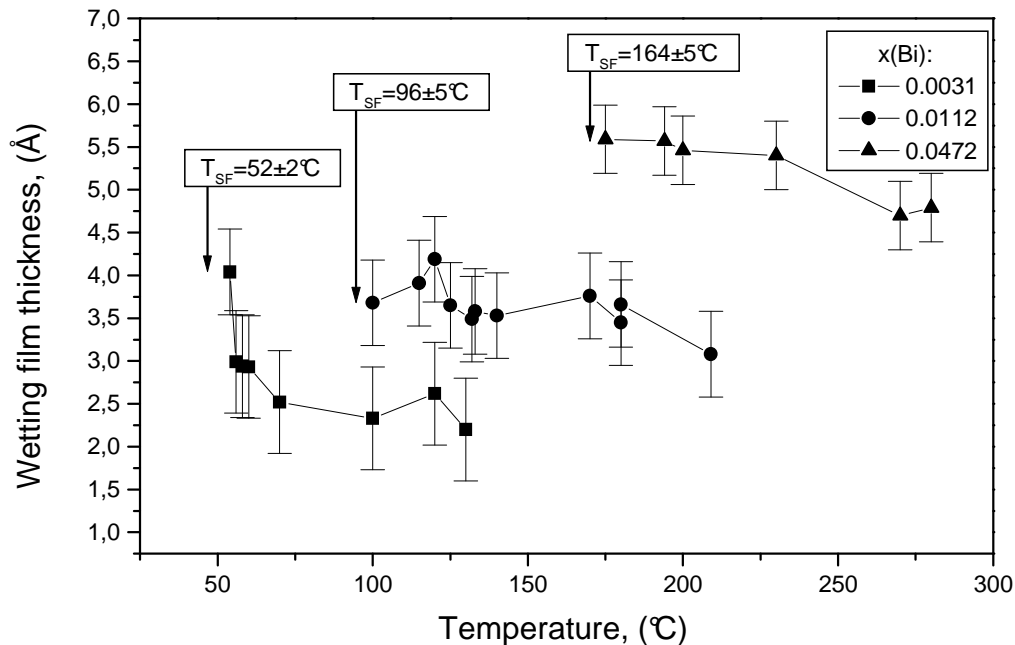


Fig. 5.4 Dependence of the wetting film thickness in Ga-Bi system for different concentration of Bi and temperatures above the respective surface freezing temperature T_{SF} .

For low Bi concentration one can neglect the Bi content in the bulk phase and consider it as pure Ga. For the concentration $x_{\text{Bi}}=0.0472$ it was not the case, so equations 3.11 and 3.12 were used.

The thickness of the wetting film varies between $\sim 2.5\text{\AA}$ for $x(\text{Bi})=0.0031$ and $\sim 5.5\text{\AA}$ for $x(\text{Bi})=0.0472$. Despite of the experimental error of 10 to 20%, one can notice the decrease of the wetting film thickness with temperature for all studied concentrations. The increase of the film thickness from 2.5\AA to 5.5\AA corresponds to a growth from ~ 1 to ~ 2 monolayers of Bi. This result is in good agreement with the results obtained by other methods [40, 83]. It is also consistent with model calculations [95].

5.1.2 Ga-Pb

The XPS spectra of the Pb and the Ga-Pb alloy are shown in Fig. 5.5 and 5.6, respectively. One can notice, that these spectra closely resemble the spectra of Bi and Ga-Bi alloy, since Pb as the neighbour of Bi in the periodic system of elements has a very similar pattern of transitions to Bi (compare 5.4a and Fig. 5.1a) The $4f_{7/2}$ peak at 1349 eV,

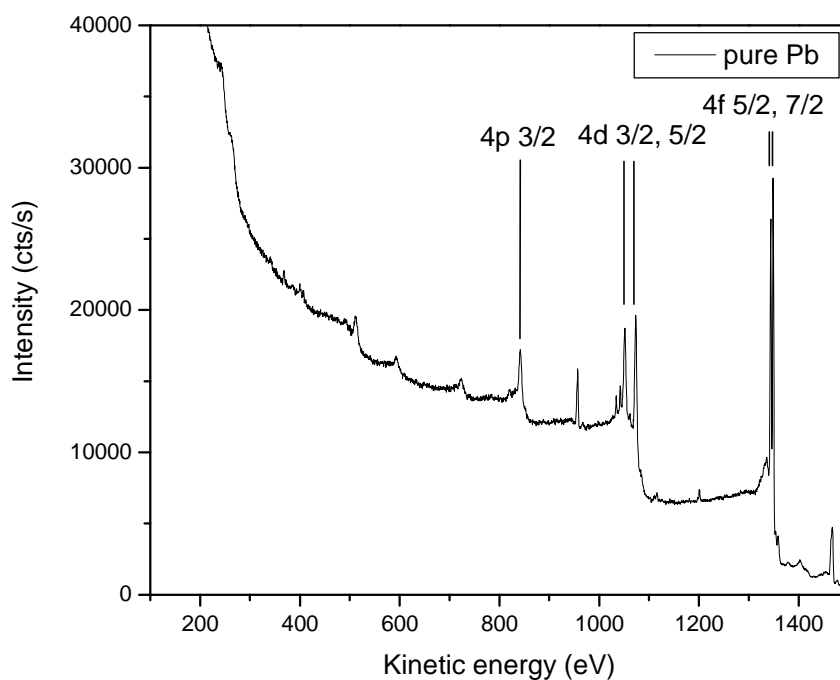
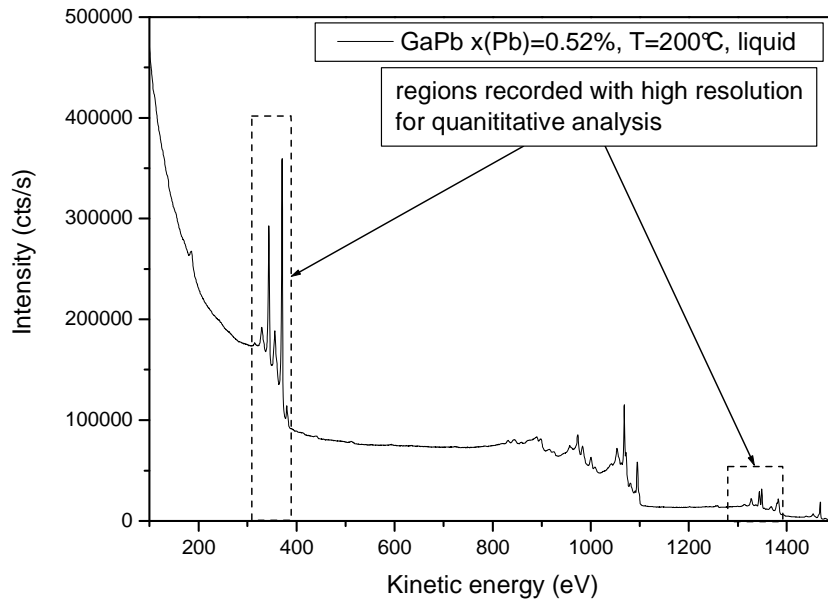


Fig. 5.5 XPS spectra of pure Pb (a) at room temperature. For quantitative analysis the area of Pb $4f_{7/2}$ peak was used.

a)



b)

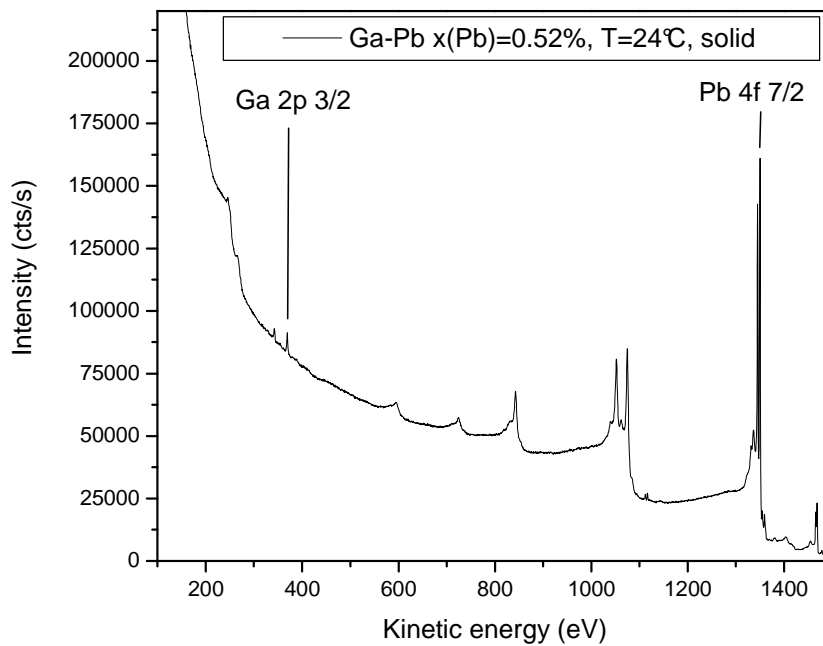


Fig. 5.6 XPS spectra of Ga-Pb alloy, $x(\text{Pb}) = 0.0052$ in liquid (a), $T > T_{\text{SF}}$ and solid (b), $T \ll T_{\text{SF}}$ states.

which has a high intensity and almost no overlapping, was chosen for the quantitative analysis and determination of the film thickness. It was performed as described above (see Ch. 3.1) using the absolute intensities of standards i.e. pure Ga and Pb in terms of overlayer model. In order to double-check the result, the calculation of d was repeated using eq. (3.9) and (3.10) separately. In this case one obtains two values for d : one comes from considering the XPS signals of the pure wetting film component (Pb) (eq. 3.9), another one is defined by the ration (I/I_0) for the bulk component (Ga) (eq. 3.10). Both values of d were found to be very similar to each other; moreover they were close to those, which were obtained by the combined formula (eq. 5.2):

$$\frac{I(\text{Pb})/I^0(\text{Pb})}{I(\text{Ga})/I^0(\text{Ga})} = \left(1 - \exp\left(-\frac{d}{\lambda_{\text{Pb}}(E_{\text{Pb}})\cos\theta}\right) \right) \cdot \exp\left(\frac{d}{\lambda_{\text{Pb}}(E_{\text{Ga}})\cos\theta}\right) \quad (5.2)$$

The general behaviour of the wetting film thickness in the Ga-Pb system resembles that for Ga-Bi system. The film thickness increases slightly with the concentration of Pb and decreases slowly with the temperature. These relative changes

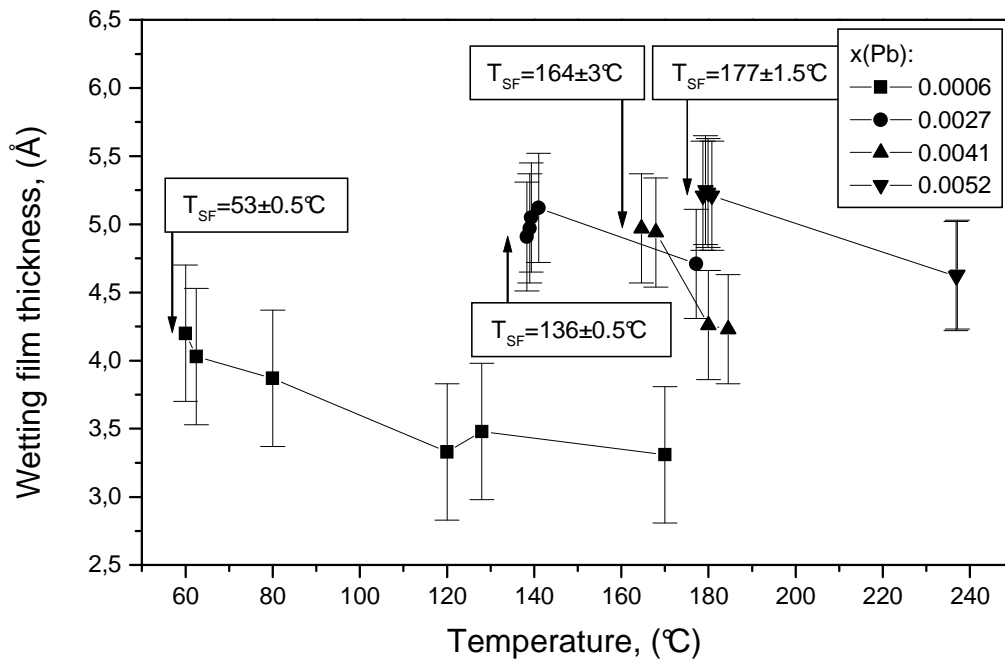


Fig. 5.7 Temperature dependence of the wetting film thickness in Ga-Pb system for different concentration of Pb.

are clearly visible on the XPS spectra, but their magnitude remains within the experimental error of the applied method. The dependence of wetting film thickness on the temperature for several studied concentrations of Pb is shown in Fig. 5.7.

5.2 Surface freezing films in the Ga-Bi system

One central objective of this study is to characterize the surface freezing films studied before by SHG [34, 38], surface light scattering [39, 40], ellipsometry [36] and model calculation [95]. This chapter describes the experimental results for the Ga-Bi system with compositions between the eutectic and the monotectic points. The questions of interest comprise such properties as SF film *thickness*, its *homogeneity* and *chemical composition* as well as the dependence of these variables on the temperature. Results from electron spectroscopy methods (XPS, AES) as well as tunneling microscopy techniques are presented below.

5.2.1 Homogeneity of the SF films – results from AES

This part of the study was supposed to answer the following questions:

- 1) Does the SF film cover the entire alloy-vapor interface after the SF transition?
- 2) Is the thickness of the SF film everywhere the same?

As it is already mentioned in Ch. 3.1 a significant difference between AES and XPS techniques is the dimensions of the analysis area. In the setup used in this study it is practically impossible to resolve the fragments of the surface using XPS. So the AES, capable to answer the questions above, was successfully applied. The numerical interpretation of the AES results is more difficult in comparison to the XPS because of the unknown electron backscattering factor $r(E)$. But this method is suitable for the determination of the relative changes in the SF film thickness as a function of the position on the surface.

The AES experiments were conducted as follows: By means of the manipulator the crucible was set so that one spot of ~1mm in diameter on the surface is exposed to the electron beam from the e-gun. Then the spectra of the Ga LMM Auger transition (1067

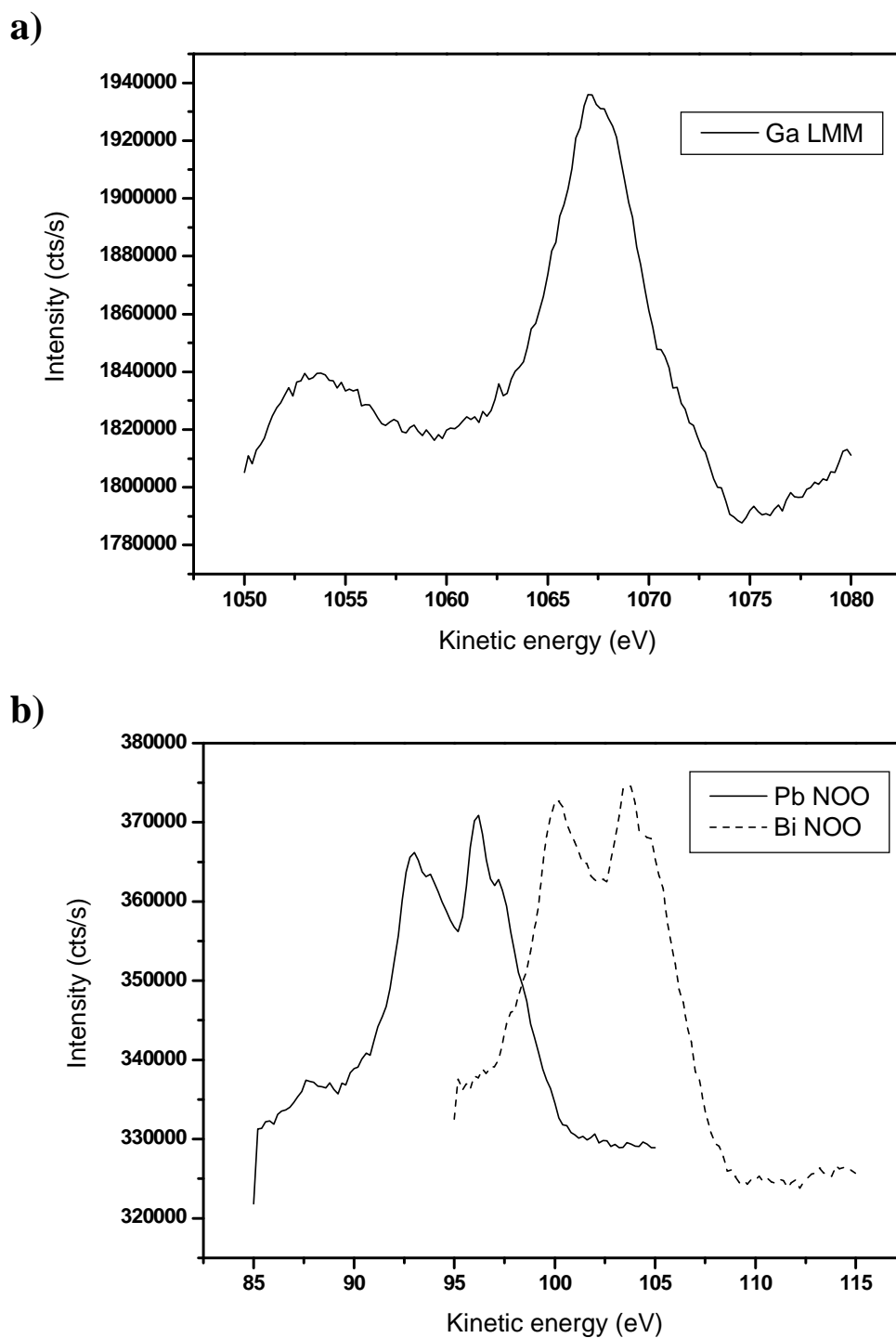


Fig. 5.8 Fragments of the AES spectra of Ga (a), Bi and Pb (b)

eV) and Bi (NOO transition, 105 eV) were recorded (see Fig.5.8). Afterwards the crucible was moved so that another point appears in the focus of the e-gun and so on. Only the position of the crucible in the XY plane was changed, the geometry of the analyzer and

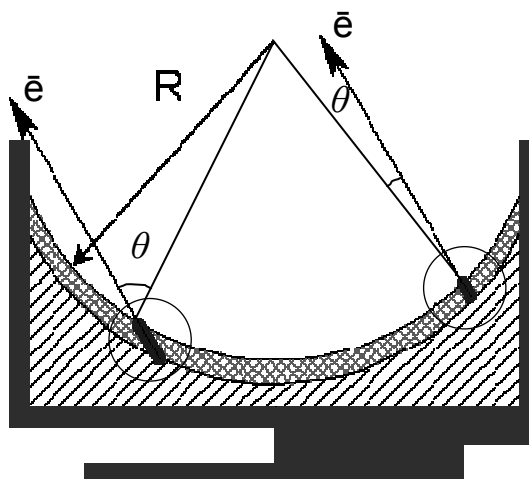


Fig. 5.9 Surface profile in the cylindrical crucible. The apparent film thickness is not the same for different points on the surface. It depends on the surface curvature.

the source were kept constant. Typical distance between measurement points was 2-3 mm; so a rectangular grid, covering the entire surface, consisted of 15-25 points. The following settings of the e-gun were used: $E_{el} = 3000$ eV, $I_{fil} = 2.25$ A, $I_{em} = 1$ μ A, grid = 0.28, focus = 5.62 (relative scale). The temperature of the crucible during the whole scan must be kept constant.

The value of the SF film thickness was determined by the numerical solution of eq. (5.3) – analog of the eq. (5.1) applied for the XPS measurements:

$$\frac{I(Bi)/I^0(Bi)}{I(Ga)/I^0(Ga)} = \frac{1+r(E_{Bi})}{1+r(E_{Ga})} \cdot \left(1 - \exp\left(-\frac{d}{\lambda_{Bi}(E_{Bi}) \cos \theta}\right) \right) \cdot \exp\left(\frac{d}{\lambda_{Bi}(E_{Ga}) \cos \theta}\right) \quad (5.3)$$

whereby the electron backscattering factor $r(E)$ was assumed to be equal to zero for all points [62]. The $I_0(Pb)/I_0(Ga)$ ratio was estimated from the AES data for the wetting film with known thickness. For a quantitative analysis the curvature of the surface should be taken into account (Fig. 5.9). The electron emission angle θ is not the same for all points of the AES scan. It is difficult to describe the precise shape of the surface, so an approximated model is required. We modeled the alloy-vapor interface as a fragment of a sphere with the radius R (Fig. 5.9). R as the only fitting parameter was estimated from the AES measurements of the wetting film. Using this model one can calculate the correct values of θ for different measurement points. The shadow effect from the walls of the

crucible was also taken into account excluding a part of the area from consideration. After the calculation of the thickness d for a given temperature the map of the surface i.e. the thickness profile of the SF film as a function of the coordinates X and Y was constructed.

A typical map for the Ga-Bi system at $T=T_{SF}$ is shown in Fig. 5.10a. For all measured concentrations of Bi the maps of the SF films exhibit similar features:

- 1) In most experiments the SF film covers the entire surface of the alloy. This is consistent with the observation made by naked eye.
- 2) The SF films are more or less homogeneous i.e. the calculated thickness does not vary much when one jumps from one measurement point to the next one.
- 3) All observed films are very thick in comparison with the wetting films. The typical thickness obtained with eq. 5.2 were found to be around 50-70Å. This value is 4-5 times larger than the IMFP λ for the Ga LMM signal (and ~10 times larger than $\lambda(E_{Bi})$). Thus, the error of the overlayer model for such d is very large. So the real thickness of the SF film can be much greater than 50Å.
- 4) The properties of the SF films were found to be independent on the cooling rate. Different cooling rates (1-20 K/h) were investigated.
- 5) After the SF transition the formed film seems not to change its thickness and homogeneity if the temperature of the system is decreased. No significant transformations were observed on the SF films during the subsequent cooling 20-50K below T_{SF} (similar behaviour shows SF films in Ga-Pb system at cooling rates > 1 K/h, characterizing however by lower thickness, see also Fig. 5.14, circle symbols). This means either the film is stable and the thickness does not change or these changes are outside of the depth resolution of the AES method.
- 6) The SF films are stable with time. No changes of thickness or homogeneity were observed within the period up to 96 hours, when the system was kept at the SF temperature.

One should notice that a different behaviour, comparing to that described above, was observed in a few experiments. For example, fragment of the surface, which was not covered with the SF film, was sometimes detected at $T \leq T_{SF}$ when formation of the film was already complete. This can be ascribed on the impurity effect, when the oxidized surface prevents the formation of the SF film, although oxygen content was not determined by means of AES.

5.2.2 Thickness of the SF films

Some aspects concerning the thickness of the SF films were discussed in the previous chapter. More precise measurements of the thickness were performed by means

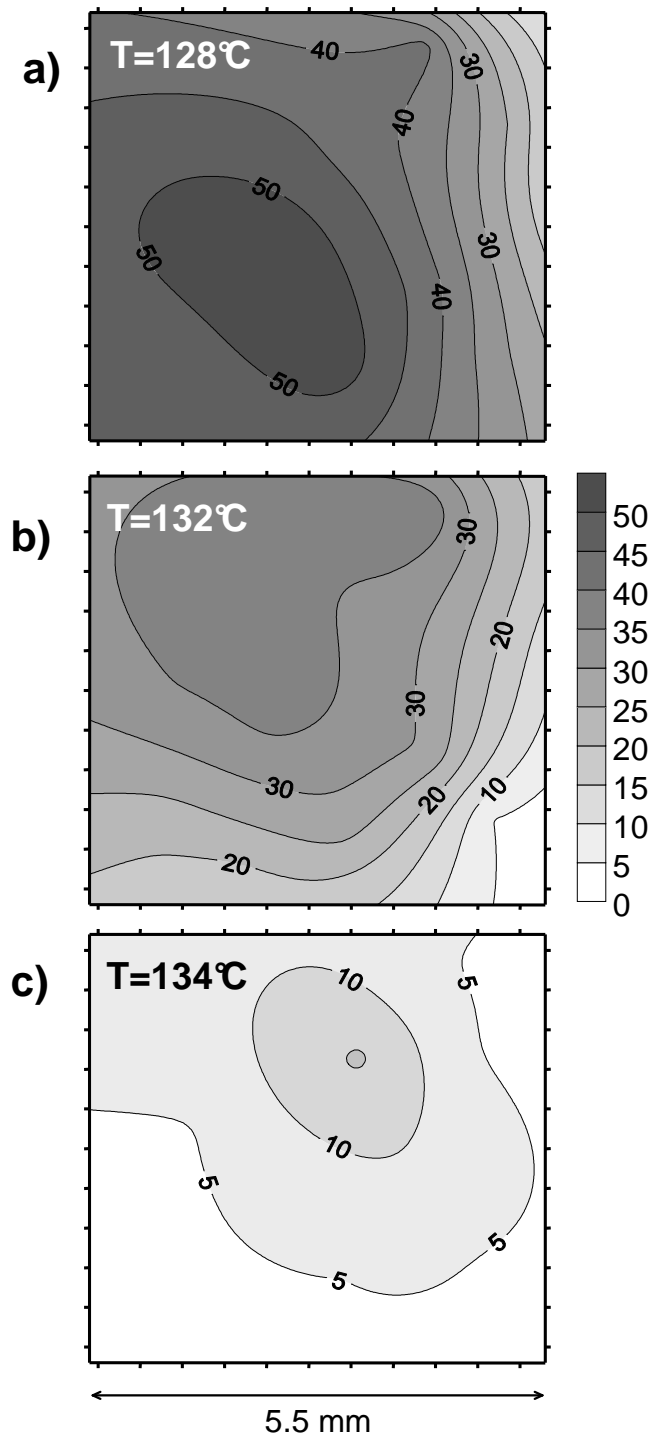


Fig. 5.10 Maps of the surface constructed on the results of AES investigation of the Ga-Bi alloy, $x(\text{Bi})=0.0115$. After formation of the SF film at a cooling rate of 5 K/h (a) the sample was heated up with 0.05 K/h. The resulting surfaces (b) and (c) are thinner than the original one. The thickness of the SF film changes gradually without partial melting.

of XPS. Typically, after the SF transition on cooling one can see a strong increase of the Bi signal simultaneously with the rapid disappearing of the Ga peak [84].

The magnitude of the Ga $2p_{3/2}$ peak after the SF transition for all measured concentrations is distinguishable in different cooling cycles, but in most cases it was relatively low. The eq. 5.2 yields the corresponding thicknesses of the SF films between 25 and 40\AA . As it is already mentioned, this value is 3-4 greater than the IMFP for Ga peak ($\sim 10\text{\AA}$ at 370eV), what increases dramatically the uncertainty of the method for such thick film. It is not clear why the relative intensities of Bi and Ga sometimes vary significantly for different experiments, performed under the same (or very similar) conditions. One possible explanation can be an incomplete coverage of the interface with the SF film, whereby the small part of the surface remains liquid. This effect has been observed several times when the system was kept at $T = T_{SF}$ for 5-10 hours or when the temperature was slowly (3-5 K/h) decreased below T_{SF} . The incomplete coverage could

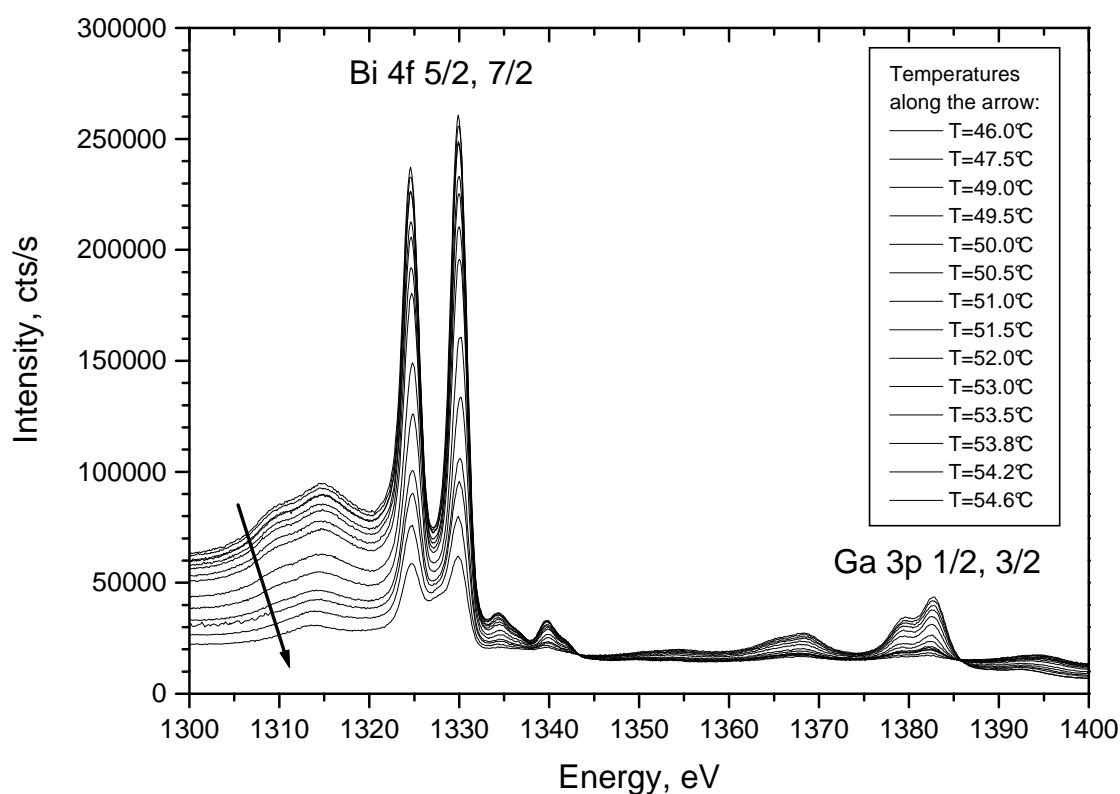


Fig. 5.11 Typical XPS spectra of Ga-Bi alloy, $x(\text{Bi})=0.0031$ on heating. The transition from one spectrum to the next one is gradual, without abrupt changes.

result in an increase of the Ga signal, accompanied by a decrease of the Bi one¹. Taking into account the latter possibility one can qualitatively conclude that the SF films in Ga-Bi system are usually more than 40-60Å (~ 15-20 ML) thick independently on the Bi concentration.

XPS spectra of the Ga-Bi system on cooling for the temperatures below SF point do not reveal any changes, because the intensities of the both components remain practically the same. Therefore, it was concluded that no significant perturbations in the SF film takes place, when the system is cooled below the SF temperature. If it is heated up after the formation of the SF film, the following phenomena were observed: At a temperature of 2-4K above T_{SF} the SF film starts to melt. This is consistent with the hysteresis behaviour observed in the SHG and capillary wave studies [40, 34, 38] The melting of the SF film, appears to the observer as the gradual melting of bulk material i.e. disappearing of the SF film from parts of the surface. It is accompanied by a significant growth of the Ga peak simultaneously with a fall of the Bi signal in the XPS spectrum (Fig. 5.11). At the end of the transition the alloy seems to be identical to the one before cooling. Such behaviour was found to be typical for SF films, formed at cooling rates of 0.5-5 K/h.

One experiment with the Ga-Bi alloy for $x_{Bi}=0.0115$ was performed with an extremely slow heating rate of 0.05 K/h. The film thickness was measured by means of AES. The results are shown in Fig. 5.10. In this case the gradual decrease of the film thickness rather than partial melting was observed. In a separate run the temperature of the alloy was kept constant for the same period of time (~5 days) and no changes in the thickness were detected.

The altering of the alloy surface, resulting from the formation of the SF film was also studied by means of UPS. The UPS spectra of the Ga-Bi ($x(Bi) = 0.0031$) alloy for two temperatures above and below the SF transition are displayed in Fig. 5.12. The spectrum of the SF film is characterized by two signals at 18.3 eV and 20.5 eV respectively. These signals were also found in the spectrum of pure Bi, measured by Ölhafen et al. [85]. They disappear when the SF film melts at increasing temperature (>50°C).

¹ We emphasize, that only a few number of XPS measurements on the SF films in Ga-Bi system resulted in high Ga-peak intensity, what can be interpreted either as low film thickness or as the thick film, which covers only a part of the interface.

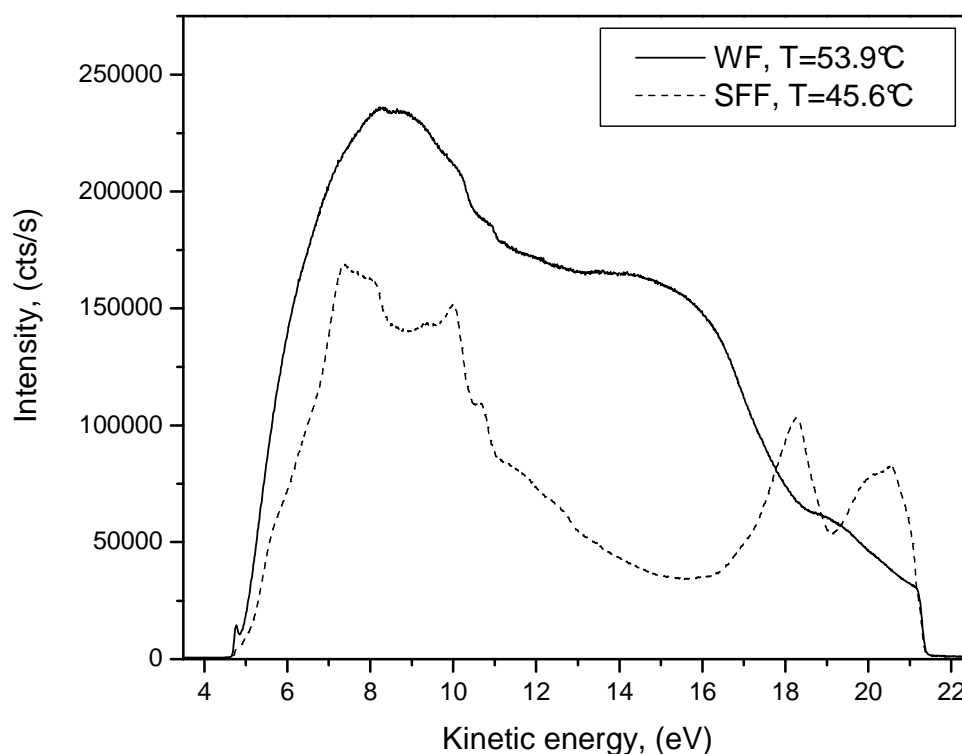


Fig. 5.12 UPS spectra of Ga-Bi alloy, $x(\text{Bi})=0.0031$ before and after SF transition. Two peaks at 18,3 eV and 20.5 eV are specific for solid Bi.

The depth profiling experiment utilizing layer-by-layer sputtering was performed with strongly undercooled SF films in the Ga-Bi system. The surface of the alloy was prepared in a following way: the SF film was obtained as usual by cooling of the sample with a cooling rate of 7 K/h starting from one-phase region. After formation of the SF film the cooling was continued until the room temperature is reached. This resulted in the solidification of the bulk alloy, because the Ga-Bi system does not show a supercooling behaviour. The surface of the alloy (i.e. strongly undercooled SF film) was sputtered during definite time and subsequently analyzed by means of XPS. Then this procedure was repeated several times. The results are summarized in the Table 5.1. The calibration of the sputter-gun yields the sputtering rate of 0.25 ± 0.1 ML/s for pure Bi. The effect of the preferential sputtering was considered as negligible. From the Table 5.1 one can see that the change of the chemical composition of the sputtered material takes place only during the first hundred seconds of sputtering; this corresponds to the removal of approximately 25 ML of the material. The study of deeper layers up to 1.5 μm gives almost the same chemical composition within the error of the method. It is remarkable,

Sputtering time (hours)	Depth (nm)	I(Ga) (eV*cts/s)	I(Bi) (eV*cts/s)	x(Ga) from I(Ga)
0	0	268.9	1172	0.065
0.03	10	580.4	1019	0.14
0.06	20	576.2	999.0	0.14
0.1	32	532.5	992.8	0.13
0.6	195	609.1	981.6	0.15
1.6	520	550.6	985.6	0.14
3.6	1200	590.1	952.4	0.15
4.6	1500	640.1	926.8	0.16

Table 5.1 The results of the depth profiling experiments using sputtering in Ga-Bi ($x(\text{Bi})=0.0031$) alloy. According to the calibration procedure sputtering rate was estimated to $\sim 0.25 \pm 0.1$ ML/s for pure Bi. Thickness for one ML of 0.4nm [87] was taken.

that the bulk composition was not reached even after removal of 1.5 μm of the metal. The SF film appears to play an important role for the nucleation and growth of the Bi-rich bulk phase during the phase separation process. Although this method does not provide information about the SF film thickness in the moment of its formation, it can be useful for the characterization of the alloy at lower temperatures ($T \ll T_{\text{SF}}$).

5.2.3 Surface topography of the strongly undercooled films

The aim of the following part of this study was to investigate the surface structure of the SF films on the micro- and nanometer scale with the STM technique. Such information can help to answer many questions concerning the properties of the SF films. Unfortunately all attempts to acquire STM images at the SF temperature, directly after SF film formation, were not successful. We assume that the liquid Ga-rich phase underneath the SF film can cause some critical problems for the STM image acquisition. These could be e.g. a floating of the entire film on the top of the liquid phase. Another complication is that a short electric contact of the tunneling tip with the liquid phase occurs (it can happen due to defects in the SF film). In this case the feedback electronics of the microscope will withdraw the tip immediately, this is also known as jump-to-contact phenomenon, described by [86]. In order to get rid of these negative effects the temperature of the

system was decreased to reach the point of the bulk freezing. In this state it was possible to reach a stable, vibration-free tunneling mode.

The strongly undercooled SF films for the Ga-Bi samples with Bi concentrations of 0.0031 and 0.0115 were investigated by STM at room temperature. The parameters for the microscope were chosen as follows: bias voltage ± 0.08 -0.4 V, tunneling current 0.08-0.5 nA, loop gain 5-10%, scan speed 2000-3000 nm/s. The dimensions of the STM images were varied from $5 \times 5 \text{ nm}^2$ (atomic resolution) up to $2 \times 2 \mu\text{m}^2$. Usually one or two pulses of 5-10 V were applied to the fresh W-tip in order to remove the oxidized material from the apex and so to reach the appropriate quality of the STM images. This procedure was sometimes repeated during the experiment.

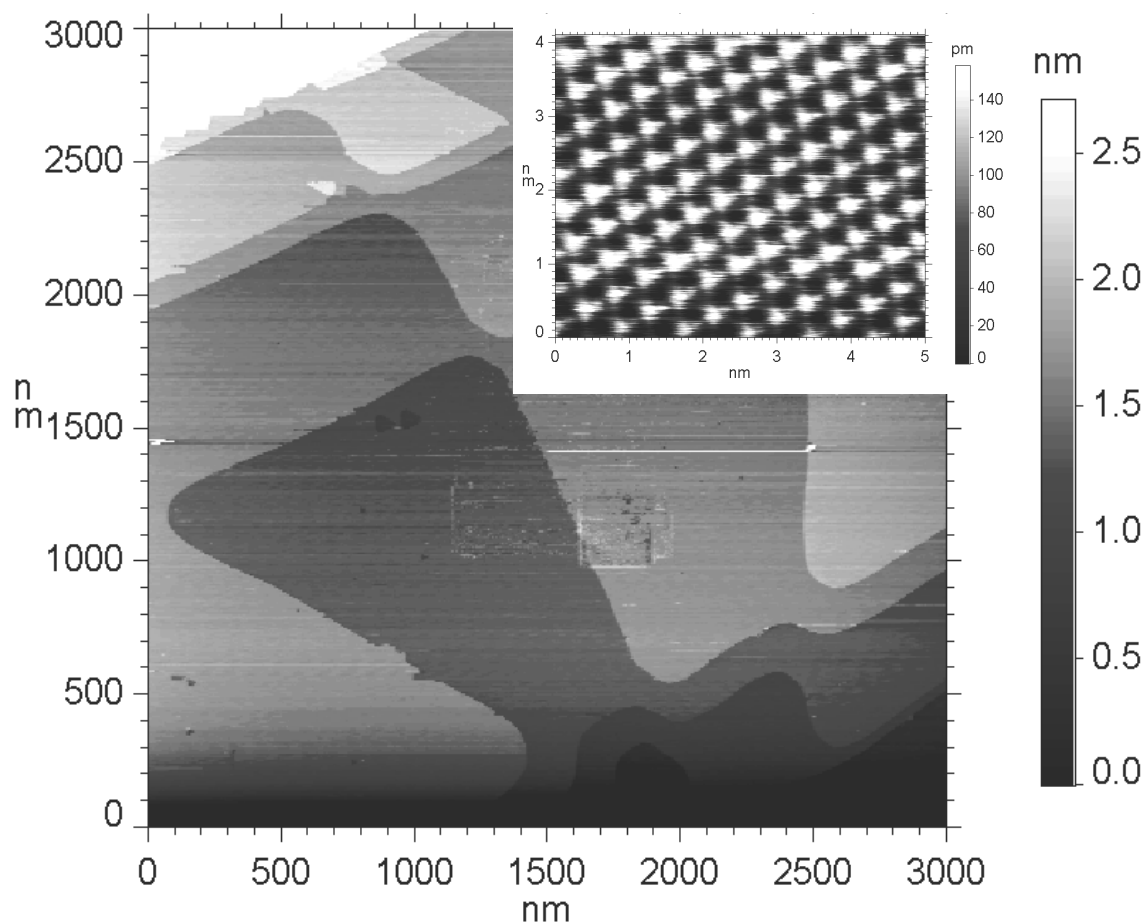


Fig. 5.13 STM image at room temperature of the solid/vapour interface of a Ga-Bi alloy, $x(\text{Bi}) = 0.0115$ after the SF transition and bulk solidification. Atomically resolved Bi(0001) is shown in inset.

The image in Fig 5.13 shows typical features of the undercooled SF films in the Ga-Bi system. Atomically flat terraces have an area up to some μm^2 . This value is extraordinary large in comparison to the dimensions of the terraces in pure bulk crystalline Bi [87]. The height of the terraces was determined to be 0.37 ± 0.02 nm; this value is in good agreement with the step edge height of 0.4 ± 0.002 nm measured by STM at room temperature on a Bi single crystal cleaved along the basal trigonal (0001) plane [88]. The terraces contain a few defects like islands and holes. Their height (depth) was observed to have a thickness corresponding to 1ML. The latter feature was not always detected for the freshly prepared surfaces. One can see that these small defects as well as large terraces have very often a triangular symmetry. A zoom into the terrace results in the atomic resolved image (Fig 5.13, inset), exhibiting an ordered hexagonal structure with the corresponding interatomic distance of 0.44 ± 0.02 nm. This result is also in good agreement with the known lattice constant of 0.4533 for Bi in the (0001) plane in a three-fold symmetrical trigonal network.

5.3 Surface freezing films in the Ga-Pb system

5.3.1 Thickness and homogeneity of SF films in the Ga-Pb system

Formation of the SF film in the Ga-Pb system is considered in this chapter. XPS and AES techniques have been applied to characterize the film thickness and homogeneity. A comparison with the SF phenomenon in the Ga-Bi system is also provided.

The appearance and development of the SF film for the Ga-Pb alloy looks similar to that in the Ga-Bi system if one observes it with naked eye. A front, which has a different reflection (it appears grayer), starts to grow from one or several points usually near the walls of the crucible, when the temperature of the alloy on cooling reaches a certain value above the liquidus temperature, known as SF temperature. The fronts join each other and the film formed in this way covers a large fraction of the surface. This process usually took less than one minute for the crucible used in our experiments. Those parts of the interface near the walls of the crucible, which were not covered by the SF film, do not undergo visible changes if the cooling of the crucible is continued. That means, the lateral growth of the film seems to stop in approx. one minute after the

beginning of the formation and the film seems not to expand or to stretch during further cooling.

The film appears for the observer to be more or less homogeneous immediately after formation and in the next 60-100 minutes. Using a high-resolution CCD camera one can only see joints of different fronts and the border between the SF film and the “liquid” parts of the interface¹. After approx. 1.5 hours when the system is kept at constant temperature one can record with the CCD camera the unexpected appearance of microscopic islands (see detailed description in Chapter 5.3.2).

For the characterization of the SF film without any visible defects one of the following approaches can be used. The XPS spectrum can be either recorded immediately after SF film formation or at lower temperatures with sufficient cooling rate. It was found experimentally that the formation of defects (islands) can be suppressed when the system is cooled down with a cooling rate higher than approx. 3 K/h.

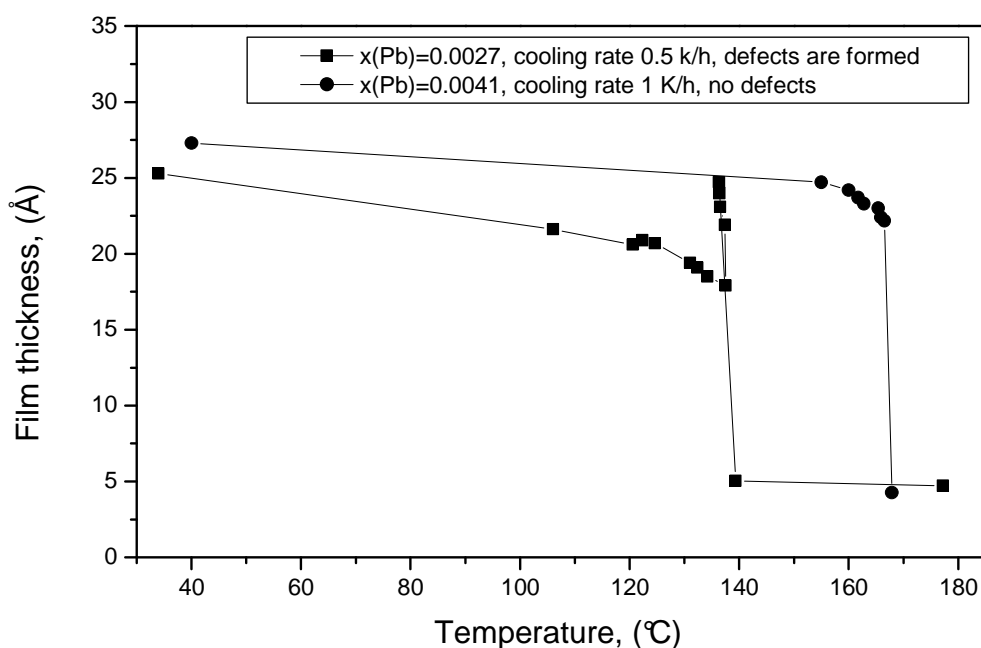


Fig. 5.14 The dependence of the SF film thickness on temperature for two different cooling rates. The thickness is calculated according to the overlayer model (eq. 5.2).

¹ Designation “liquid” is more or less correct since this part seems not to change during SF transition. Unfortunately we do not have further information, but the optical observation of the reflection difference gives a strong indication.

In a first approximation the thicknesses of the SF films can be calculated in the same way as for wetting film i.e. using eq. (5.2). Limitations of this approach as well as alternative methods are discussed in ch. 6.1. Fig. 5.14 represents the changes in the SF film thickness as a function of temperature. Such behaviour (slow increase of d with decreasing temperature) was found to be typical for all studied alloys. The comparison of the thickness dependence for films with and without defects is also provided.

5.3.2 Evolution of the SF films in Ga-Pb system

The SF films in the Ga-Pb system are not stable – they undergo deep changes with time if the system is kept at constant temperature. Defects of different types appear on the surface after a while, in contrast to the Ga-Bi system¹. Detailed description of these defects as well as a quantitative interpretation of the XPS data is provided in this chapter.

An important experimental observation, which attracted special attention to the problem of the time evolution of the SF films, was a significant increase of the Ga signal in XPS spectra recorded 3-6 hours after film formation. First it was associated with a relaxation of the film and respective decrease of the film thickness. Then the use of a high-resolution CCD-camera with zoom function gave unexpected results: the film did not appear as a homogeneous one, but it had many islands of approximately the same size. The subsequent detailed analysis revealed that the islands become visible in ~1 hour after SF film formation². The appearance and the growth of islands were followed within next 5-7 hours. Depending on the conditions of the film formation (cooling rate, external heat sources like X-ray tube etc.) the islands can reach 100-150 μm in diameter (Fig 5.15 left, bottom) or they grow together forming some kind of interconnected structure (Fig 5.15 right bottom). In some experiments the appearance of grooves with ~100 μm width was also observed. This seems to be a final state in the evolution of the SF film, because no change was usually observed after 10-15 hours.

The reflection of defects (islands and grooves) resembles the reflection of the liquid surface of Ga-Pb alloy at the temperature above SF transition i.e. wetting film. Moreover, the reflection of islands does not change on heating of the alloy, which results

¹ Ga-Bi system has been intensively studied in our laboratory in a separate experiment by means of ellipsometry. The CCD camera was used to check the surface of the liquid alloy and SF films. Formation of islands or other kinds of defects was not observed.

² Minimal size of objects, that can be resolved using this camera, is about 10 μm .

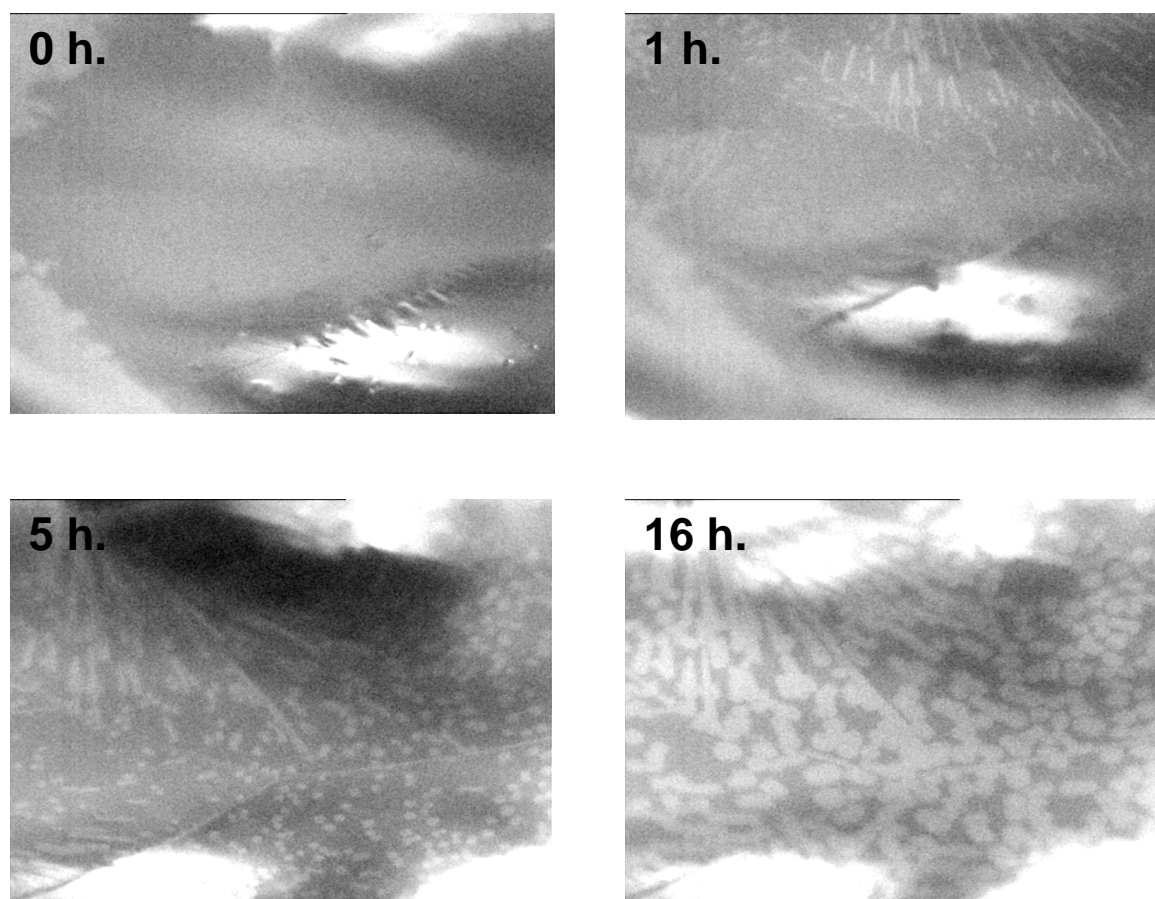


Fig. 5.15 Evolution of the SF film in Ga-Pb system, $x(\text{Pb}) = 0.0041$ at constant temperature. Formation of defects is clearly visible.

in the film melting. So the assumption, that the islands consist of a Ga-rich liquid phase, is very probable.

As it was mentioned above, at the high cooling rates (3 K/h and more) the formation of island is not observed. The time-dependent formation of islands is likely in competition with the growth of the film thickness in z -direction. If the film is thick enough, the defects probably could not start to form. At the lower temperatures the deposition of bulk Pb on the SF film, which is precipitated due to phase separation, can theoretically improve this effect.

Unfortunately the use of AES could not give any additional information that can be used for the characterization of the SF films. The spot size of the AES gun was found to be too large ($\sim 1\text{mm}$ in diameter) to resolve the defects ($\sim 0.1\text{mm}$), so one can obtain only an averaged signal of islands and film. Taking into account additional difficulties concerning the interpretation of the AES results and respective large uncertainties, they are omitted here.

5.3.3 Surface topography of the strongly undercooled films

Investigation of the undercooled SF films in the Ga-Pb system was performed in a similar way as this was done for the Ga-Bi system. Usually the alloy was heated up well above the liquidus temperature and then it was cooled to the room temperature with a cooling rate of 5-7 K/h, which is high enough to avoid the formation of islands. Due to a strong tendency of the bulk Ga-Pb alloy to be supercooled for all studied concentrations, temperatures of -20 -40°C were required in order to reach the freezing of the bulk.

Prepared in such a way the surface was subjected to the STM characterization. The following parameters were used for the microscope: bias voltage $\pm 0.2 - 0.35\text{V}$, tunneling current 0.15-0.25nA, loop gain 6-10%, scan speed of $\sim 2500\text{ nm/s}$ for large images ($1 \times 1\mu\text{m}^2$, $2 \times 2\mu\text{m}^2$), and $\sim 250\text{ nm/s}$ for small images with atomic resolution ($5 \times 5\text{ nm}^2$, $10 \times 10\text{ nm}^2$).

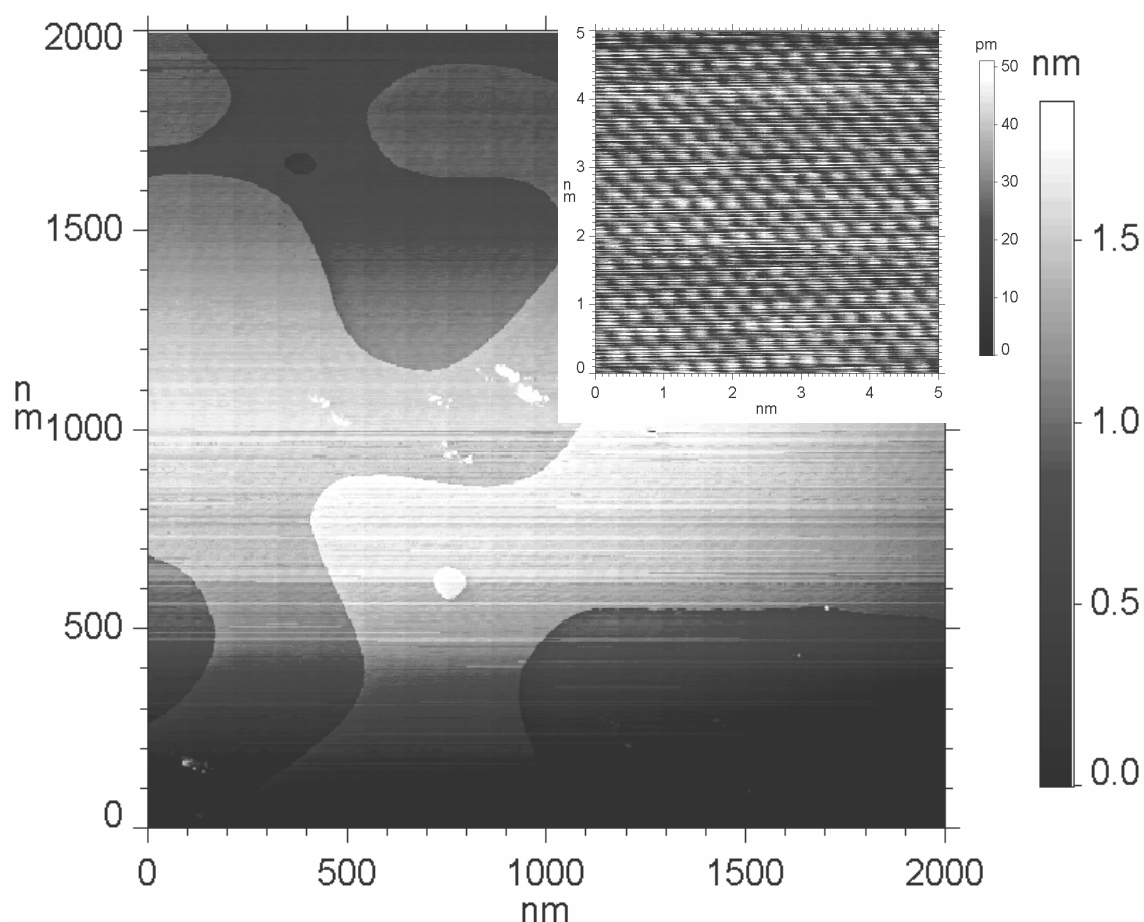


Fig. 5.16 STM image at room temperature of the solid/vapour interface of a Ga-Pb alloy, $x(\text{Pb}) = 0.0041$ after the SF transition and bulk solidification. Atomically resolved Pb(111) is shown in inset.

The typical view of the surface was found to be independent on the Pb concentration in the bulk. One of the STM images, representing special features of the strongly undercooled SF film in Ga-Pb alloy, is shown in Fig 5.16. The surface is characterized by very large, atomically flat terraces without any defects. The edges of the terraces have curved shape, its height was found to be about $0.3\pm 0.02\text{nm}$ (value of 0.33 is given by [89] for pure Pb). Such a step edge height corresponds to one monolayer. The small image with atomic resolution shows hexagonally ordered atoms with lattice constant of $0.36\pm 0.01\text{nm}$. This value is also in good agreement with known lattice constant for (111) surface of Pb monocrystal [90].

5.4 Tip-induced surface modification and nanostructuring

The phenomena described in this chapter are modification of the alloy surface on the nanometer scale via interactions with STM tip. Such a modification was not the primary objective of the study, however it was discovered during the STM experiments on the strongly undercooled SF films in the Ga-Bi system [90]. Although surface modification through the STM tip is a well known phenomenon described in the literature [91-94], the case of Bi to our knowledge is not studied yet. The mechanism of tip-induced surface modification is also under discussion [94]. Therefore we report here the results, which appear to be very interesting and promising for further investigation.

The tip-induced surface modification experiments were performed on the Ga-Bi alloy with the concentration of Bi = 0.0115. The SF film was obtained as it is described in Ch. 5.1.4. Very large, atomically flat terraces on the top of the SF film in the Ga-Bi system represent a perfect platform for the surface modification experiments. Even insignificant changes can be easily detected on such a flat surface. Basically three types of the tip-induced nanostructures were observed: squares, small craters/holes and large ones. We begin the description with the first observed type of artificial nanostructure, i.e. the squares (or parts of it). An unexpected STM scan results from the same area repeated several times initiates subsequent investigations. The feature, which attracted an attention, was a kind of rectangular pattern in the upper left angle of the STM image. It was not visible on the first scan, then it appeared on the second scan (same area and dimensions), twice on the third one and so on. Careful consideration of the images in Fig. 5.17 results

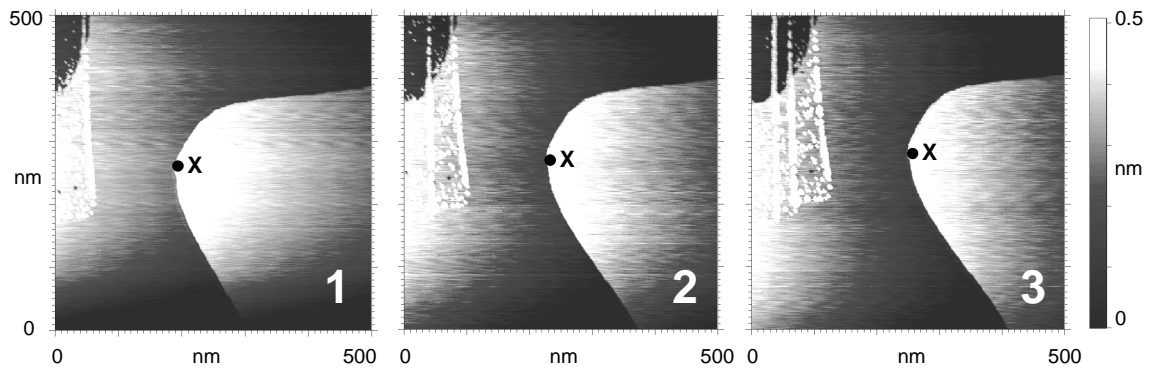


Fig. 5.17 STM images of Ga-Bi, $x(\text{Bi}) = 0.0031$ solid/vapour interface. Three subsequent scans. See text for details.

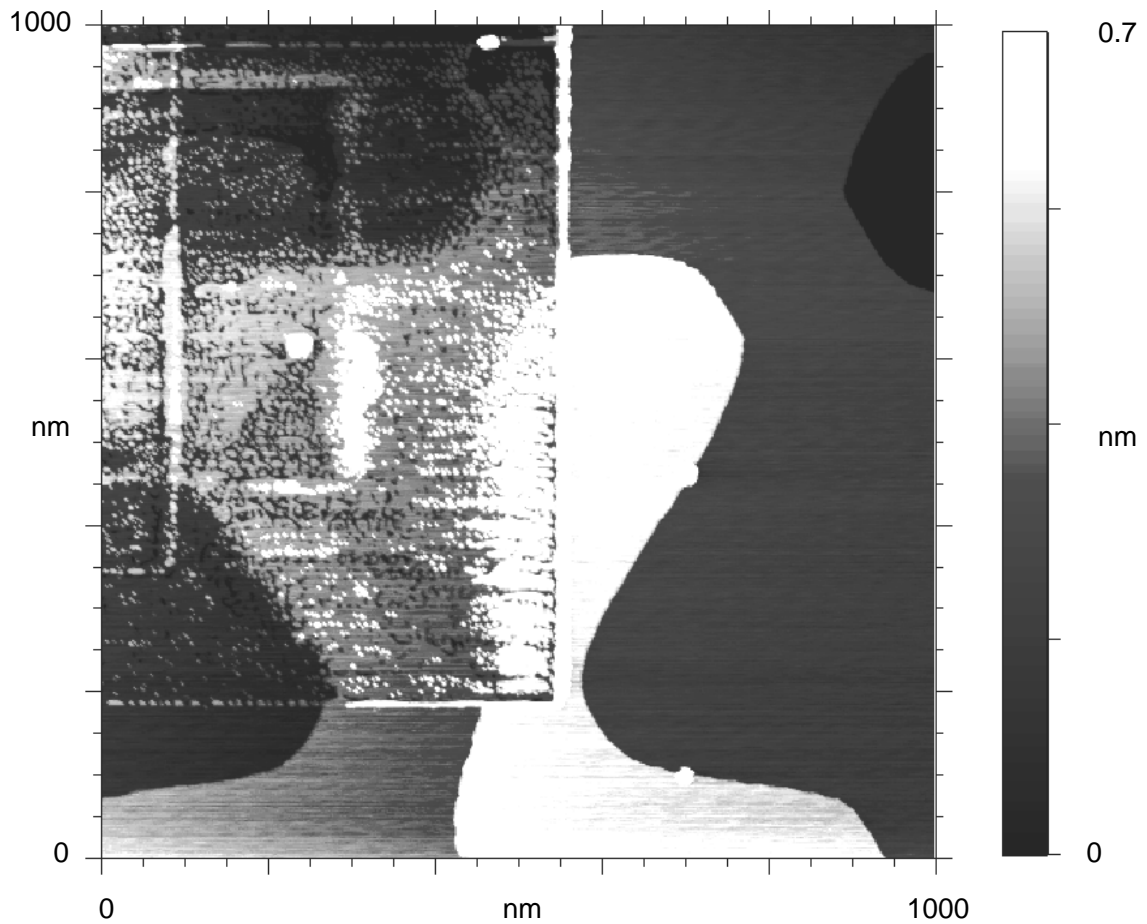


Fig. 5.18 Artificial nanostructures of rectangular shape. Parameters of the scan are as follows: $V_{\text{bias}} = 0.4$ V.

in the following observation: the distance between the first rectangular pattern and the point “X” (it was arbitrarily chosen on the step edge on the first image and then fixed). That means, the surface undergoes a slight thermal drift. Moreover, one can notice, that rectangular pattern lies exactly on the left and upper borders of the previous image.

Fig. 5.18 displays the result of another experiment: after the series of scans the scan area was shifted down and to the right from the original position. Then the scan was repeated, the resulting image is shown on the Fig 5.18. One can see that the upper left angle shows quite different features in comparison to the rest of the picture. The surface appears to be changed during the first scan. The step edges can be still be recognized despite of the damage. The borders of the first scan appear as barriers of 1-2nm (3-5ML) height. Formation of such barriers on the outer borders of the scan area was confirmed in several experiments with different tunneling tips, including the scans, rotated by 45° in respect to the previous one.

The key to the understanding of the surface modification during the STM imaging is variation of scan parameters: bias voltage, feedback current and, probably, scan speed. Without discussion of the mechanism of the nanostructuring, it is important to notice that the appropriate combination of scan parameters results in atom transfer between the STM tip and the sample surface. The set of parameters can be empirically adjusted in order to control the intensity and direction of the atom transfer.

The approach described above was further developed for the creation of one-dimensional patterns (grooves or barriers) as well as zero-dimensional ones (pits and islands). An option in Scala® software used together with Micro SPM H microscope to switch the scanner among frame-, line- and point-mode can be utilized for this purpose. An optimization of the scan parameters was performed empirically in order to achieve controlled extraction and deposition of Bi atoms.

Fig 5.19 shows artificially formed nanostructures such as islands (1), barrier (2), pits (3) and groove (4). They were obtained by applying relatively high bias voltage of +3V (3,4) and -2,8V (1,2) respectively. Switch of the sign of the bias voltage results in change of the atom transfer direction. Tunneling current was kept constant at 0.5nA. Point-mode (1,3) and line-mode (2,4) of the scanner were utilized, in latter case a rather large value for the scan speed (4000 nm/s) is required to achieve the desire effect.

The respective height profiles are shown in the Fig 5.19b. The depth of the pits and grooves corresponds mostly to 1-2ML i.e. it is greater than normal step edge of the terraces. Islands and barriers can be characterized with the same height. It was shown that

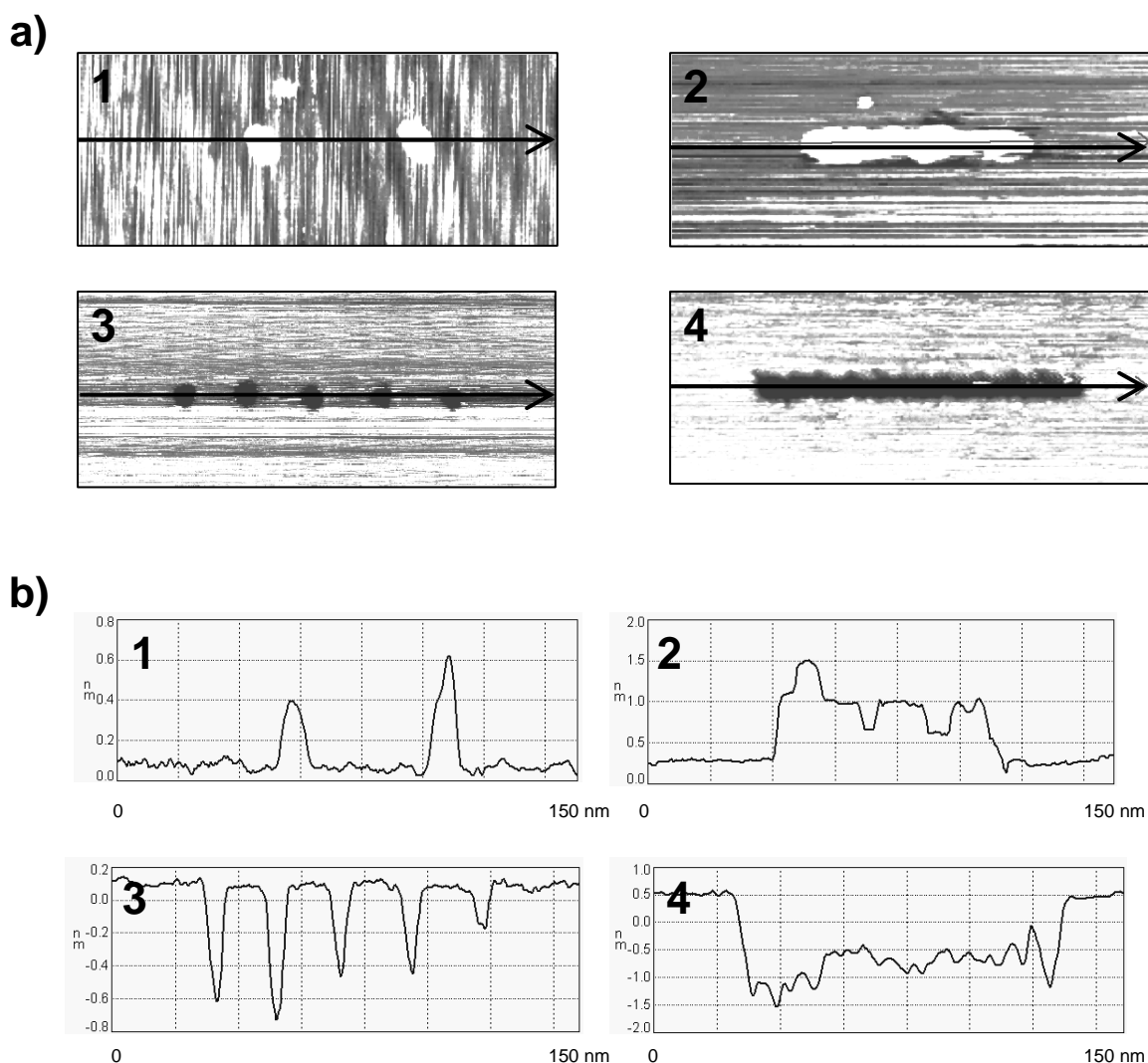


Fig. 5.19 Artificial nanostructures on the surface of the Ga-Bi alloy made by high bias voltage pulses; (a) STM images (dimensions: 150x60 nm): islands (1), barrier (2), pits (3) and groove (4) are formed applying -2.8V (1,2) or +3.2V (3,4) bias voltage; (b) corresponding line profiles.

near circular shape of the pits and islands is not stable with time. After a while they accept a triangular shape, which seems to be typical and energetically more favourable for the defects at Bi-surface.

The size of the nanostructures can be changed by slight variation of the bias voltage, but this effect was found to be weak. Further increase of the bias voltage to $\pm 4V$ results in much more serious damage on the surface. One can see the outcome of such a pulse in point mode in the Fig 5.20. A mount of $\sim 20\text{nm}$ height surrounded by “moat” is formed. Real dimensions of the moat are probably larger than that shown in the picture, because the tip is probably unable to reach its deepest point if the width of the moat is

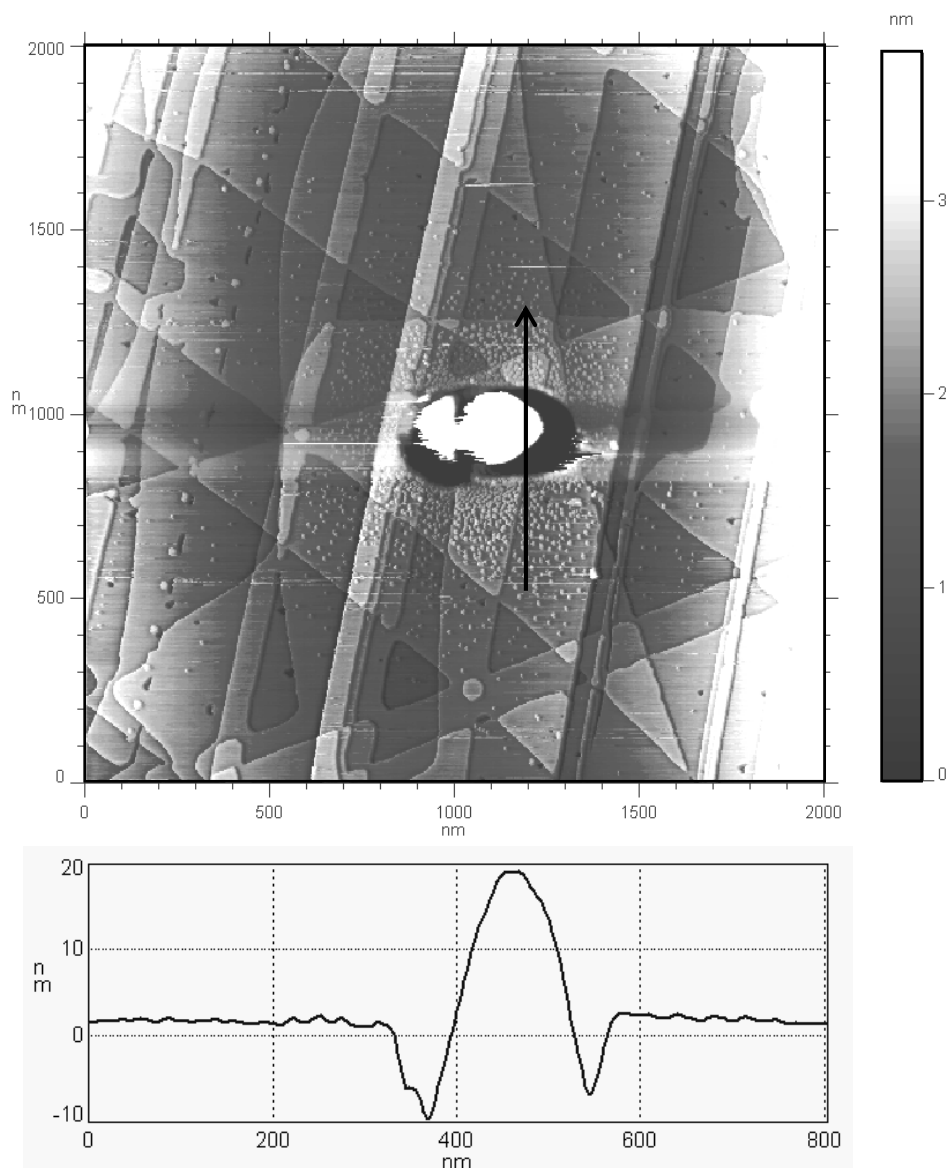


Fig. 5.20 STM image of Ga-Bi, $x(\text{Bi}) = 0.0031$ solid/vapour interface. Dimensions: $2 \times 2 \mu\text{m}$. The defect in the middle is the result of the pulse application. ($V_p = 4\text{V}$). Correspond depth profile is shown below.

smaller than the width of the tip. An array of splitters is visible in the lower part of the image – they appear as many preferentially triangular islands of 1ML height.

The mechanism of described surface modification and nanostructuring as well as the details of tip-surface interactions will be discussed in the Ch. 6.3.

Chapter 6.

Discussion

6.1 Modelling of thickness, coverage and chemical composition for the surface freezing films in the Ga-Pb system

Several approaches to the interpretation of the XPS data with respect to the thickness and homogeneity of the SF films are proposed and discussed. Besides of the simple overlayer model, which assumes Pb as the only component of the SF film, another model approach describing the film material as a mixture of Pb and Ga is considered. For the quantitative description of the SF film with defects in Ga-Pb system a possibility of incomplete coverage is taken into account.

6.1.1 Surface freezing films without defects

One of the main problems for the thickness determination of the SF films in the Ga-Pb system is that the overlayer model fails if one splits the eq. 5.2 into two equations considering the Ga and Pb signals separately:

$$\frac{I(Pb)}{I^0(Pb)} = 1 - \exp\left(\frac{-d_1}{\lambda_{Pb}(E_{Pb}) \cos \theta}\right) \quad (6.1)$$

$$\frac{I(Ga)}{I^0(Ga)} = \exp\left(\frac{-d_2}{\lambda_{Pb}(E_{Ga}) \cos \theta}\right) \quad (6.2)$$

where d_1 and d_2 are the thickness of the overlayer calculated in two different ways: eq. 6.1 takes into account only the change in the intensity of the overlayer component, whereas eq. 6.2 operates with bulk component only. Indeed, if the model were correct both equations should give the same value for the overlayer (= SF film) thickness:

$$d_1 = -\lambda_{Pb}(E_{Pb}) \cos \theta \cdot \ln\left(1 - \frac{I(Pb)}{I^0(Pb)}\right) \quad (6.3)$$

$$d_2 = -\lambda_{Pb}(E_{Ga}) \cos \theta \cdot \ln\left(\frac{I(Ga)}{I^0(Ga)}\right) \quad (6.4)$$

i.e. d_1 must be equal to d_2 , which is not the case for the most of XPS measured SF films in Ga-Pb system. One example, illustrating this discrepancy is given in the table 6.1. From the table 6.1 one can conclude that the overlayer model gives consistent values of d for the wetting films, whereas the difference between d_1 and d_2 for the SF films is quite large.

I(Ga) 2p3/2	I(Pb) 4f7/2	T (°C)	d_1 (Å), Pb from eq.(6.3)	d_2 (Å), Ga from eq. (6.4)	$d_{\text{effective}}$ from eq. (5.2)	System state
1320	89.1	237.1	4.7±0.4	4.6±0.4	4.6±0.4	WF
1334	89.9	236.0	4.7±0.4	4.5±0.4	4.6±0.4	WF
1294	102.5	180.8	5.4±0.4	4.9±0.4	5.2±0.4	WF
1296	103.3	179.9	5.5±0.4	4.9±0.4	5.2±0.4	WF
1295	103.7	179.3	5.5±0.4	4.9±0.4	5.3±0.4	WF
856	428.4	179.0	38±5	9.5±0.9	16±3	SFF starts to form
434.1	464.6	178.3	45±7	17±3	21±4	SFF
427	466	176.7	46±7	17±3	22±4	SFF

Table 6.1 XPS measurements of the SF transition in Ga-Pb ($x(\text{Pb}) = 0.0052$) alloy. Cooling rate of 5 K/h was used. Notes: WF – wetting film, SFF – surface freezing film, SFF+I – surface freezing film with defects (islands).

This discrepancy in two different methods of the thickness calculation can not be explained merely through large uncertainty of the film thicknesses. Therefore it gives rise to the assumption, that the structure of the SF films is more complicated than we believed in the beginning. The time evolution of the SF film, i.e. the formation of islands allows us to assume that the film is not in thermodynamic equilibrium and it consists probably of Pb with some small fraction of Ga. This could be different types of incorporations like cavities or clusters of Ga-rich phase in the film. This could be also microscopic islands of Ga, which are visible neither by naked eye, nor by the CCD-camera. Since these are only assumptions and nothing specific is known about those incorporations, the material of the film could be considered as a mixture of two components with effective concentration of Ga (Pb is main component).

In order to find a more appropriate way of characterization of the SF film it may be useful to introduce two more variables besides of the film thickness d : The first one is the mole fraction of Ga in the film material, x_{Ga}^f , which will characterize the effective chemical composition of the film. The second variable is the coverage c describing the ratio between frozen parts of the interface and the entire analysis area. The appropriate model for the description of the SF film should probably take into account all three unknowns: d , x_{Ga}^f and c . From a mathematical point of view a maximum of two unknowns can be found by the solution of the system of two equations. For the SF film without holes i.e. immediately after its formation, the coverage is nearly one for most cases³. So one can describe the system with an effective thickness d and an effective Ga concentration in the film, x_{Ga}^f . The corresponding relative XPS intensities for Ga and Pb can therefore be expressed as (α and β are introduced for convenience as the relative XPS intensities for Ga and Pb, respectively):

$$\alpha \equiv \frac{I(\text{Ga})}{I^0(\text{Ga})} = \underbrace{\exp\left(\frac{-d}{\lambda_{\text{Pb+Ga}}(E_{\text{Ga}})\cos\theta}\right)}_{\text{bulk}} + x_{\text{Ga}}^f \cdot \underbrace{\left(1 - \exp\left(\frac{-d}{\lambda_{\text{Pb+Ga}}(E_{\text{Ga}})\cos\theta}\right)\right)}_{\text{film}} \quad (6.5)$$

$$\beta \equiv \frac{I(\text{Pb})}{I^0(\text{Pb})} = \underbrace{(1 - x_{\text{Ga}}^f) \cdot \left(1 - \exp\left(\frac{-d}{\lambda_{\text{Pb}}(E_{\text{Pb}})\cos\theta}\right)\right)}_{\text{film}} \quad (6.6)$$

³ Although on the photographic images one can see the border between liquid and frozen parts (see e.g. Fig. 5.14), we believe that the liquid part is outside of the analysis area and the XPS signal comes from the frozen part only.

where $\lambda_{\text{Pb+Ga}}$ describe the IMFP in mixed media. As a good approximation one can accept $\lambda_{\text{Pb+Ga}} \approx \lambda_{\text{Pb}}$ since the IMFP depends on the outgoing electron energy, rather than the nature of the material; moreover, Pb appears to be the main component of the SF film. A further assumption is, that Pb concentration in bulk liquid can be neglected ($x_{\text{Ga}}^b \approx 1$). An analytical solution of the system of equations given above is possible neither for d nor for x_{Ga}^f . But one can express one of the unknowns from the first equation and then set it into the second one e.g. x_{Ga}^f :

$$\beta(\alpha, d) = \left(1 - \frac{\alpha - \exp\left(\frac{-d}{\lambda_{\text{Pb}}(E_{\text{Ga}})\cos\theta}\right)}{1 - \exp\left(\frac{-d}{\lambda_{\text{Pb}}(E_{\text{Ga}})\cos\theta}\right)} \right) \cdot \left(1 - \exp\left(\frac{-d}{\lambda_{\text{Pb}}(E_{\text{Pb}})\cos\theta}\right) \right) \quad (6.7)$$

$$\beta(\alpha, x_{\text{Ga}}^f) = (1 - x_{\text{Ga}}^f) \cdot \left(1 - \exp\left(\frac{\lambda_{\text{Pb}}(E_{\text{Ga}})}{\lambda_{\text{Pb}}(E_{\text{Pb}})} \cdot \ln\left(\frac{\alpha - x_{\text{Ga}}^f}{1 - x_{\text{Ga}}^f}\right)\right) \right) \quad (6.8)$$

The eq. (6.7) and (6.8) can be solved either numerically or graphically. The numerical calculation of d and x_{Ga}^f was performed with an aid of the MathCAD software package. The determined values of d and x_{Ga}^f with corresponding experimental data α and β are shown in the table 6.2.

Another method for the determination of d and x_{Ga}^f is a graphical solution: $\beta(\alpha, d)$ and $\beta(\alpha, x_{\text{Ga}}^f)$ are to be plotted on the same graph, whereby α is considered as an independent variable; d and x_{Ga}^f taken as parameters. Such a plot is shown in Fig. 6.1a. The solid line in the Fig. 6.1 on the left of the plot represents the solution of the eq. (6.8) for the constant film composition of $x_{\text{Ga}}^f = 0.12$. The lower dashed line is $\beta = \beta(\alpha, d)$ for $d = 60\text{\AA}$. An intersection of the solid line with the dashed one the only solution for given α and β . Graphical data representation has significant advantage in comparison to the numerical solution of the equations (6.7), (6.8), because the influence of the experimental error in the XPS intensities on the film thickness and composition is clearly visible if the experimental points are plotted in the same graph with corresponding error bars. So if the intersection of two lines is in the uncertainty region of the experimental point that means that the film can be characterized within the considered model by definite values of thickness, composition. The uncertainty of two unknowns, i.e. thickness and chemical

composition, depends on the error of experimental points: all intersections located within the uncertainty region of experimental points represent possible states of the system.

Analysing all experimental data for the SF films in the Ga-Pb system with different concentration of Pb we have concluded that the applied model can describe the experimentally observed values of the relative XPS intensities more or less good.

x(Pb)	Run Nr.	α	β	T (°C)	x_{Ga}^f	d (Å)	d_{min} (Å)	d_{max} (Å)
0.0052	1	0.215	0.787	178.3	0.21±0.02	macroscopic	94	macroscopic
$T_{\text{SF}}=177\pm 1^\circ\text{C}$		0.211	0.788	176.7	0.21	207	91	macroscopic
	2	0.26	0.704	172.8	0.26	84	68	130
		0.26	0.722	170.7	0.26	103	77	macroscopic
		0.168	0.841	23	0.17	macroscopic	102	macroscopic
		0.168	0.903	5	0.17	macroscopic	macroscopic	macroscopic
	3	0.214	0.765	172.7	0.21	102	77	macroscopic
		0.205	0.784	171.1	0.20	118	83	macroscopic
		0.153	0.824	165.4	0.15	100	77	macroscopic
0.0041	1	0.197	0.789	166.5	0.20	114	82	macroscopic
$T_{\text{SF}}=164\pm 3^\circ\text{C}$		0.192	0.79	165.9	0.19	106	79	macroscopic
		0.181	0.8	165.4	0.18	106	79	macroscopic
		0.176	0.808	162.8	0.18	110	81	macroscopic
		0.166	0.848	160.0	0.17	macroscopic	110	macroscopic
		0.156	0.84	155.0	0.16	150	90	macroscopic
		0.121	0.876	40	0.12	163	92	macroscopic
	2	0.188	0.831	160.2	0.19	macroscopic	117	macroscopic
		0.075	0.938	136.9	0.07	macroscopic	111	macroscopic
0.0027	1	0.075	0.938	136.9	0.07	macroscopic	110	macroscopic
$T_{\text{SF}}=136\pm 0.5^\circ\text{C}$	2	0.156	0.839	136.3	0.16	145	89	macroscopic
		0.166	0.831	136.4	0.17	157	90	macroscopic

Table 6.2 Experimental results of α and β for different bulk concentrations $x(\text{Pb})$ measured at different temperatures relative to the surface freezing temperature T_{SF} ; with these data the thickness d and composition x_{Ga}^f of the surface freezing film have been determined by numerical solution of the equations (6.7) and (6.8).

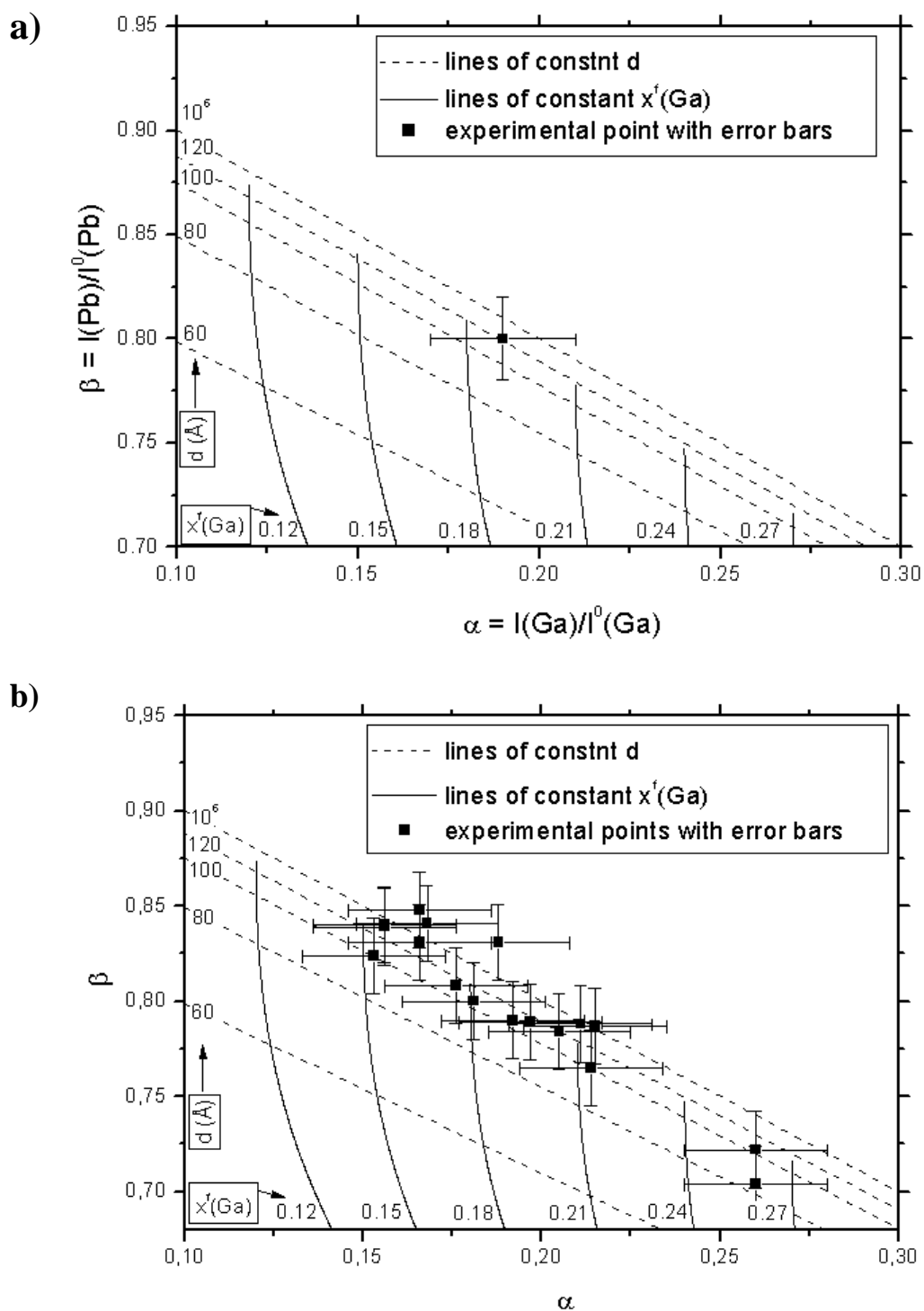


Fig. 6.1 Graphical solution of the model for description of the SF films in Ga-Pb system (a). The intersection of dash- and solid lines represent the thickness and chemical composition of the SF film for given intensities α and β . All intersections within the error bars of the experimental point describe possible state of the system. The second plot (b) shows the distribution of the experimental points in different experiments i.e. different cooling cycles and concentration of Pb. See also Table 6.2.

Following information is obtained:

- 1) One cannot observe a clear correlation of any variables d or x_{Ga}^f to the concentration of Pb in the bulk. The distribution of experimental points i.e. α and β is similar for all studied Pb concentrations (see Fig. 6.1b).
- 2) The lower limit of thickness according to the model is about 80\AA . As an upper limit one should take infinity, in practical view that means macroscopic values of few microns.
- 3) Considering the SF films immediately after formation, one can see that the content of Ga in the film varies for different experimental points from 0.16 to 0.26. The value of 0.19 ± 0.03 in the middle appears to be more probable, because the majority of the experimental points lie near it.
- 4) Within one run the Ga content in the SF film decreases with falling temperature. For the film thickness the tendency to opposite. These dependences are demonstrated in the Fig. 6.2.

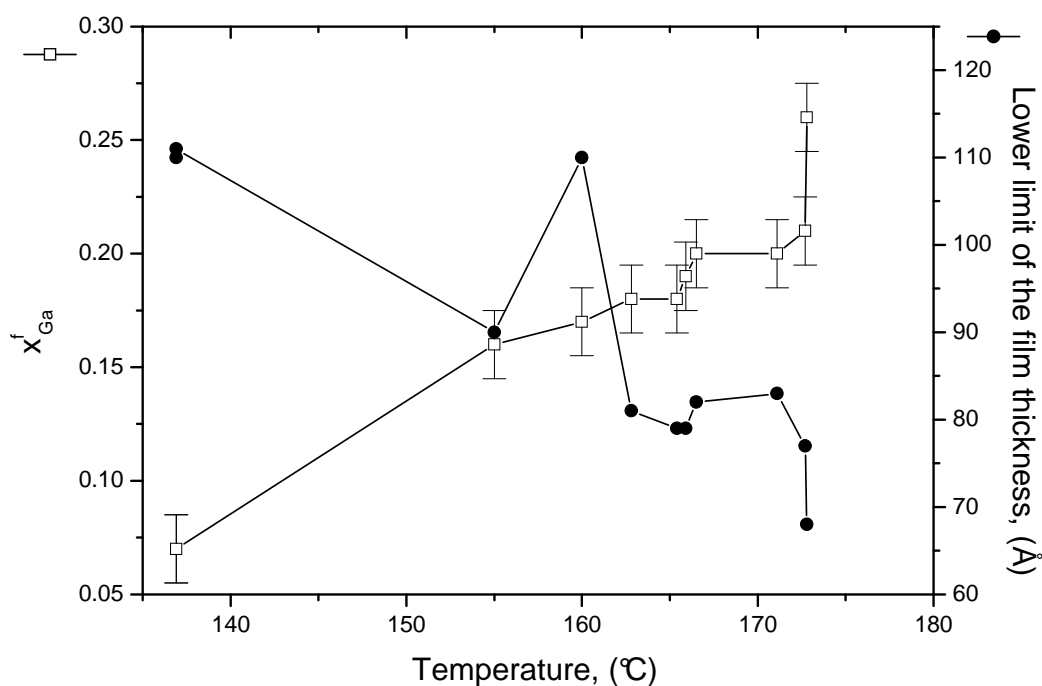


Fig. 6.2 Content of Ga in the SF film (-□-) and the lower limit of the SF film thickness (-●-) as a function of temperature. $x(\text{Pb}) = 0.0052$ with one exception for the points on the left of the plot: $x(\text{Pb}) = 0.0041$ $T = 137^\circ\text{C}$. As the maximal values of the thickness the model predicts very high (macroscopic) values for all points.

- 5) The model predicts macroscopic film thickness and low Ga content in the film for the temperatures much lower than that for SF transition. This is correct also for the room temperature.

Additionally one can notice that different effective Ga concentration in the film for different experiments is in good agreement with known facts about instability and evolution of the film, described in the next chapter.

Describing the SF films in the Ga-Bi we considered the Ga signal in XPS spectrum as an artefact, resulting from the incomplete coverage where the parts of the interface near the crucible walls remain liquid after SF transition. An alternative explanation for the Ga peak, which cannot be excluded, is also the possibility that the material of the SF film can contain some small fraction of Ga.

A theoretical description of the SF films in Ga-Bi system is given in the work of Tsekov and Freyland [95]. Pure Bi has been considered as the material of the film because of negligible solubility of Ga in solid Bi. For the constant composition of the alloy the authors predicted an exponential increase of film thickness approaching the liquidus line by decrease of the temperature. This result from the condition of equality of the chemical potentials in different phases in contact:

$$\mu_{liquid}^{bulk}(T, x) = \mu_{solid}^{film}(T, d) \quad (6.9)$$

$$\mu_{liquid}^{bulk}(T, x) = \mu_{liquid}^0 + RT \ln x + c_0 + c_1 T + c_2 T \ln T \propto \rho_{Bi}^{solid} \cdot \exp(-k_{TF} d) \quad (6.10)$$

where $\rho_{Bi}^{solid} = 47400 - 1.87T \text{ mol/m}^3$ is the molar density [96], k_{TF} is the wavevector of the Thomas-Fermi screening. This theoretical description can be strictly applied only for the systems in thermodynamically equilibrium state. In the experiments performed in this study the SF films in the Ga-Bi system characterized by the intermediate thicknesses (between one monolayer and macroscopic value) were not observed. This could be explained if one assumes that the real films investigated in XPS and AES experiments did not reach thermodynamic equilibrium. It seems that the SF films in both Ga-Bi and Ga-Pb systems in the moment of its formation and in the further time are metastable. The SF films in Ga-Pb system can be definitely defined as metastable, because of dramatic changes, which can be observed in several hours after the film formation at constant temperature.

6.1.2 Surface freezing films with defects in the Ga-Pb system

Besides of the model for the SF films described above, which is characterized by variable thickness and chemical composition and which assumes a homogeneous film, an alternative modelling approach is proposed and evaluated within the frameworks of this study. It takes into account inhomogeneity of the film as shown in Fig. 5.15. A varying coverage is the obvious difference between the films with and without defects. For the latter case the coverage of 100% was assumed, whereas the occurrence of islands decreases this value significantly. Two models described below use the coverage as variable together with thickness (1) and composition (2). These approaches are presented below.

1. Variable thickness and coverage. The SF film is considered as a slab with an effective thickness d , which covers a certain part of the interface – the rest of the interface is liquid. The spot of electron analyzer contains both of them. The system is described with the following equations:

$$\left\{ \begin{array}{l} \alpha = c \cdot \underbrace{\exp\left(\frac{-d}{\lambda_{Pb}(E_{Ga}) \cos \theta}\right)}_{\text{bulk_under_SF_film}} + (1-c) \underbrace{\exp\left(\frac{-d_0}{\lambda_{Pb}(E_{Ga}) \cos \theta}\right)}_{\text{bulk_under_wetting_film}} \\ \beta = c \left(\underbrace{1 - \exp\left(\frac{-d}{\lambda_{Pb}(E_{Pb}) \cos \theta}\right)}_{\text{SF_film}} \right) + (1-c) \left(\underbrace{1 - \exp\left(\frac{-d_0}{\lambda_{Pb}(E_{Pb}) \cos \theta}\right)}_{\text{wetting_film}} \right) \end{array} \right. \quad (6.9)$$

Graphical solutions are constructed using:

$$\beta(\alpha, d) = 1 - t_1 + \left(t_1 - \exp\left(\frac{-d}{\lambda_{Pb}(E_{Pb}) \cos \theta}\right) \right) \cdot \left(\frac{\alpha - t_2}{\exp\left(\frac{-d}{\lambda_{Pb}(E_{Ga}) \cos \theta}\right) - t_2} \right) \quad (6.10)$$

$$\beta(\alpha, c) = (1-c) \cdot (1-t_1) + c \left(1 - \exp\left(\frac{\lambda_{Pb}(E_{Ga})}{\lambda_{Pb}(E_{Pb})} \ln\left(\frac{t_2(c-1) + \alpha}{c}\right)\right) \right) \quad (6.11)$$

where the contribution of the wetting film is given by constants: $t_1 = \exp(-d_{wf}/\lambda_{Pb}(E_{Pb})) = 0.842$, $t_2 = \exp(-d_{wf}/\lambda_{Pb}(E_{Ga})) = 0.65$ ($d_{wf} = 4.8\text{\AA}$). The model did not give satisfactory results for the SF film with or without defects.

2. Variable composition and coverage. As in the latter model the SF film does not cover the entire analysis area. The frozen part is assumed to be a of macroscopically thick film (10 μm) with some fraction of Ga as incorporations or cavities. XPS intensities are expressed as follows:

$$\left\{ \begin{array}{l} \alpha = c \left(\underbrace{x_{Ga}^f \left(1 - \exp\left(\frac{-d^f}{\lambda_{Pb}(E_{Ga})}\right) \right)}_{\text{bulk_under_SF_film}} + \underbrace{\exp\left(\frac{-d^f}{\lambda_{Pb}(E_{Ga})}\right)}_{\text{SF_film}} \right) + \underbrace{(1-c) \exp\left(\frac{-d_0}{\lambda_{Pb}(E_{Ga})}\right)}_{\text{bulk_under_wetting_film}} \\ \beta = \underbrace{c(1-x_{Ga}^f) \left(1 - \exp\left(\frac{-d^f}{\lambda_{Pb}(E_{Pb})}\right) \right)}_{\text{SF_film}} + \underbrace{(1-c) \left(1 - \exp\left(\frac{-d_0}{\lambda_{Pb}(E_{Pb})}\right) \right)}_{\text{wetting_film}} \end{array} \right. \quad (6.12)$$

Contribution of bulk under SF film in total Ga signal can be neglected¹. Corresponding functions for the graphical solution are given as:

$$\beta(\alpha, c) = \left(1 - \frac{\alpha - t_2 + ct_2}{c} \right) \cdot c + (1-c) \cdot (1-t_1) \quad (6.13)$$

$$\beta(\alpha, x_{Ga}^f) = (1-x) \cdot \left(\frac{\alpha - t_2}{x_{Ga}^f - t_2} \right) + \left(1 + \frac{\alpha - t_2}{x_{Ga}^f - t_2} \right) \cdot (1-t_1) \quad (6.14)$$

Plots for graphical solution are shown in the Fig. 6.3.

The model of the film with variable chemical composition and coverage can be successfully applied for the characterization of the SF films with defects. An attempt to use these models for the interpretation of the XPS data for the films without defects failed because both models do not provide a combination of d and c (or x_{Ga}^f and c) which

¹ For the SF film thickness a rather large, macroscopic value of 10 μm was chosen. Since d here is several orders of magnitude greater than λ_{Ga} the part of Ga signal coming from the bulk phase underneath the film is zero. Another (smaller) value of thickness will shift the lines of constant coverage down as well as the lines of constant composition. As a result the number of intersections with experimental point will be decreased. In other words the model is getting worse.

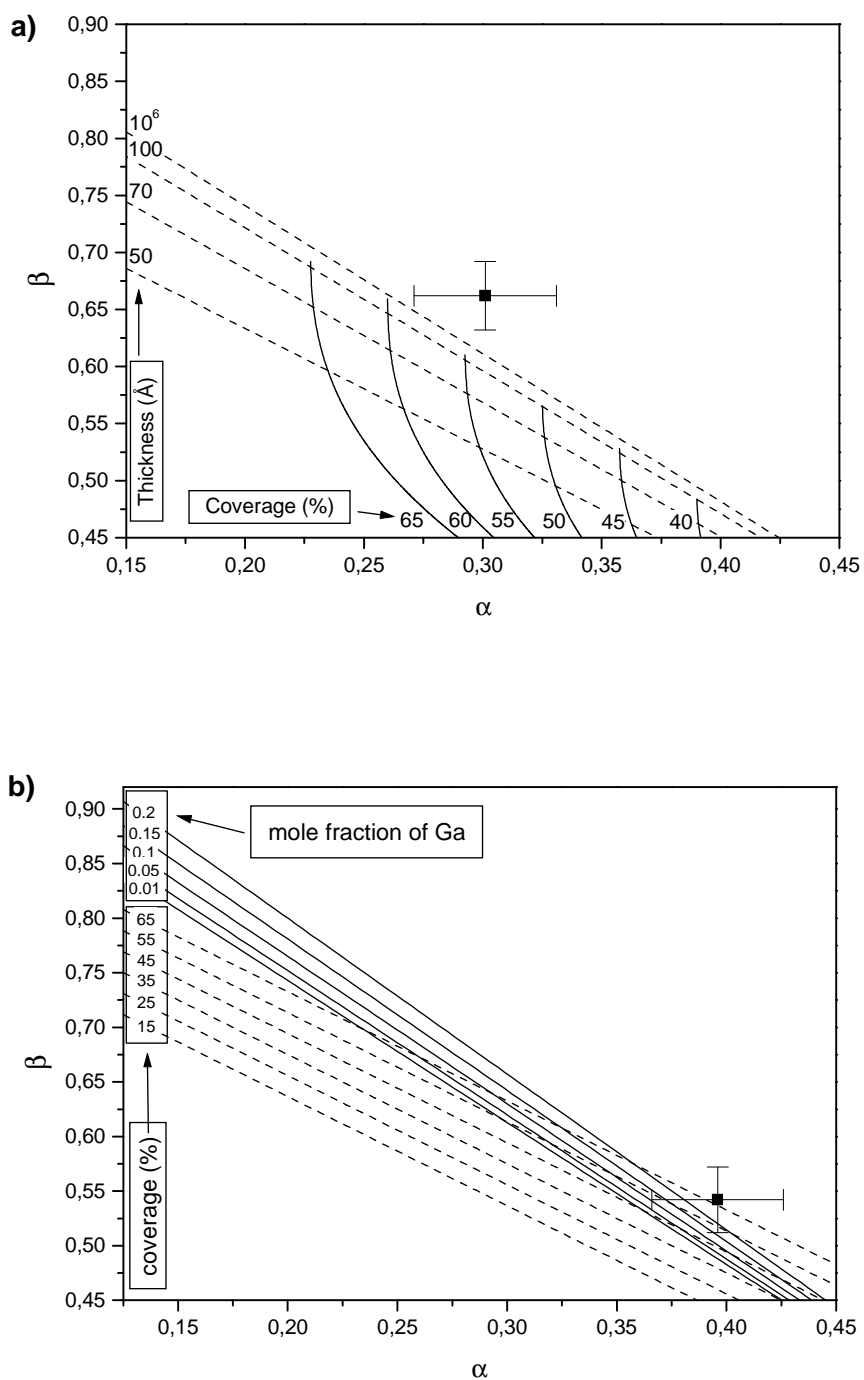


Fig. 6.3 Graphical solution of the model of variable thickness and coverage (a) and variable chemical composition and coverage (b). The second model was successfully applied for the interpretation of the XPS intensities of the SF films with defects in the Ga-Pb system.

x(Pb)	Run Nr.	Film age (h)	α	β	T (°C)	Model for SF film with defects variable x_{Ga}^f and c at constant $d = 10\mu\text{m}$	
						x_{Ga}^f	c
0.0052	1	18	0.301	0.662	176.7	0.11-0.29	0.66-0.95
	2	5.5	0.206	0.797	160.2	0.13-0.28	0.86-1
0.0041	1	2.75	0.222	0.788	162.0	0.16-0.3	0.89-1
	2*	4	0.252	0.734	161.9	0.16-0.31	0.82-1*
0.0027	1	1.5	0.183	0.812	136.5	0.07-0.24	0.82-1
		3	0.204	0.79	137.4	0.09-0.26	0.81-1
		15	0.285	0.673	137.5	0.06-0.27	0.79-0.93
		20	0.271	0.691	134.2	0.05-0.26	0.65-0.95
		23.5	0.258	0.707	132.4	0.05-0.25	0.67-0.97
		44	0.216	0.742	122.3	0-0.19	0.63-0.93
		48	0.225	0.749	120.6	0.04-0.24	0.71-1
		120	0.201	0.752	106.0	0-0.16	0.61-0.91
		135	0.147	0.843	34.0	0.01-0.19	0.8-1
	2	17	0.396	0.542	137.3	0.15-0.36	0.53-0.82
		19	0.435	0.506	137.3	0.23-0.41	0.54-0.84
		22	0.455	0.465	137.4	0.17-0.4	0.44-0.73
		39	0.514	0.395	137.4	0.26-0.47	0.39-0.67
	3	24	0.409	0.545	134.2	0.23-0.4	0.61-0.91
		48	0.471	0.41	135.0	0-0.33	0.24-0.52

Table 6.3 Results from the model 2 (variable composition and coverage) used for the description of the XPS measurements of the SF film in Ga-Pb alloys with defects. For the concentration $x(\text{Pb}) = 0.0041$ after 4 hours at $T = 161.9^\circ\text{C}$ (marked with *) a photographic image was made.

corresponds to the experimentally observed points. The parameters of the SF film predicted by the model are given in the table 6.3.

According to the model with variable d and c ($x_{Ga}^f = 0$) the area of island amounts about 10% of the analysis area for the first measurement and continually grows with time. The area of islands can be independently checked by analyzing of the photographic images of the alloy surface (it was found that islands have ~15% of the area ($c = 0.85$) for $x(\text{Pb}) = 0.0041$ after 4 hours at $T = 161.9^\circ\text{C}$). This confirmed the value for the coverage given above (0.82-1). The process of the SF film aging at very slow cooling rate of 0.4 K/h is shown in Fig. 6.4. Decrease of the coverage corresponds to growth of islands,

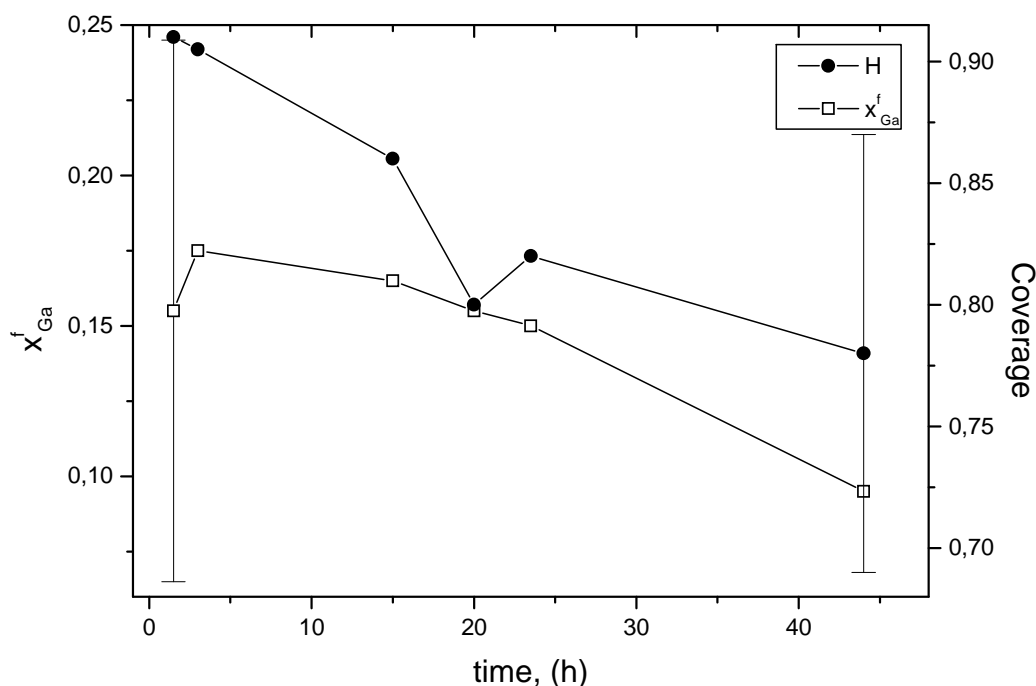


Fig. 6.4 Time dependence of Ga content in the SF film ($-\square-$) and coverage of the interface ($-\bullet-$). Temperature was decreased very slowly (0.4 K/h). Area of islands grows (decreasing coverage) simultaneously with x_{Ga}^f . Error bars for c and x_{Ga}^f are quite large.

which was experimentally observed. The model also predicts the fall of x_{Ga}^f with time. Extrapolating this result to the room temperature one will get very low Ga content in the film, that means if the islands are not taken into account, the material of the film is rather pure Pb.

Since the SF film with islands is formed from the “normal” SF film one can expect, that the Ga concentration in the film cannot differ much from the Ga concentration in the original film (here only the rest film is considered, islands are not taken into account). Indeed, for the majority of the experimental points the value of x_{Ga}^f between 0.15 and 0.2 was found. This is in good agreement with the value of x_{Ga}^f , which was observed for the SF films without defects (ch. 6.1.1)

The formation of defects on the SF films in the Ga-Pb system was observed, to our knowledge, for the first time. The cooling rate appears to be an effective method to control the formation and the growth of defects. The formation of defects can be completely suppressed at high cooling rates ($> 3\text{K/h}$).

All applied modelling approaches are strictly correct only for the flat surfaces. This is generally not always the case for the system under investigation. On one hand, we know from the STM experiment that the surfaces in both Ga-Bi and Ga-Pb systems show atomically flat terraces at room temperature, characterized by an area in the μm^2 range. On the other hand, the surface roughening transition [74-77] may affect the surface of the frozen films at elevated temperature.

6.2 Mechanism of the tip-induced nanostructuring

Surface modification on the nanometer scale is well known phenomenon [91, 93] in vacuum as well as in electrolyte environment [97]. One should start with an issue of reported applications of the STM for altering of the surface and fabrication of the structures on the nanometer scale.

Different mechanisms for the description of this phenomenon are proposed. According to [98] the interactions of the W-tip with Au-surface can be described in terms of the electroetching. Standard current density j in a normal tunneling mode can be approximately described by the following equation:

$$j_{STM} \sim \frac{e^2 \hbar}{2mA} N(E_F) V \exp(-1.1\phi^{0.5}d) \quad (6.1)$$

where V is the bias voltage, ϕ is the effective height of the tunnel barrier A is the effective area of the interaction (about 0.1 nm^2), d - the tip-surface separation $\sim 0.5 \text{ nm}$., R is the radius of the apex., $N(E_F)$ is the density of states at the Fermi level for the tip. A relatively high value of the current in the very first moment after the pulse and low effective area of the emission region of the tip gives a large value of the tunneling current density.

Increase of the bias voltage may result in the transition from the normal tunneling mode to so-called Field Emission Mode (FEM) at a well-defined threshold, which is characterized by the Fowler-Nordheim equation [99]:

$$j_{FEM} \sim F^2 \exp(-c\phi_{tip}^{3/2}v(y)/F) \quad (6.2)$$

where F , the strength of the electric field, is related to the applied bias voltage by $F = \beta V_{pulse}$, (β – geometrical factor) c is a known constant, ϕ is the work function of the tip and $v(y)$ is the slow varying function of the parameter $y = (e^3 \beta V)^{1/2} / \phi_{tip}$.

The current density in the FEM mode is 100-1000 times greater in comparison to the STM mode. This may result in sudden increase of the substrate and tip temperature followed by partial evaporation of the material. Similar processes take place also during the first treatment of the new W-tip. In order to remove the tungsten oxide from the tip apex and to reach the tunneling mode between two metals (substrate and tip) one applies a pulse of 5-10V bias voltage. The pulse changes the microstructure of the apex, which is followed by the formation of an atomically sharp tip apex capable to acquire the STM images with atomic resolution.

The second hypothesis, originally proposed for the description of the Pt nanodot formation on the Si(111) 7x7 substrate [100] implies the formation of the nanobridge between the tip and the substrate. Authors assume the following mechanism: application of relatively high bias voltage (+3V) results in a significant increase of the electric field density in the gap region. In this situation only one or two additional atoms are needed in

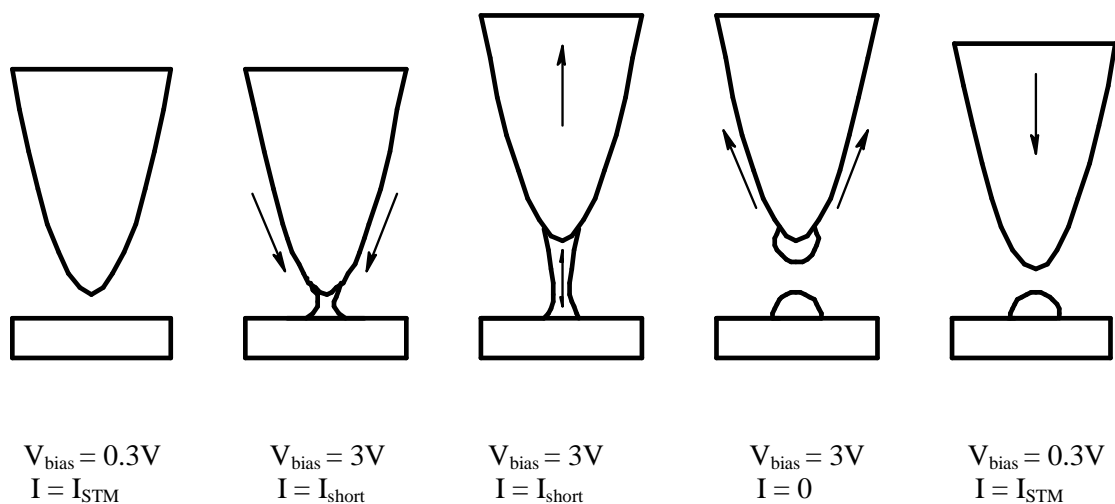


Fig. 6.5 Possible mechanism of the surface modification on the nanometer scale from [100]. Comments are in text.

the tunneling gap to disturb the tunneling mode increasing electron transport by several orders of magnitude. Such extra atoms can originate, on one hand, from the thermal diffusion processes on the surface or, on another hand, from the applied electric field. Once these atoms fill the gap, the electric current through the tip suddenly increases, this causes the electromigration-induced transfer of the atoms located on the tip surface to the apex. These atoms completely fill the gap region ($\sim 0.4\text{nm}$), forming a nanobridge. The reaction time of the STM electronics is much longer in comparison to the time of the nanobridge formation. Therefore it occurs for the next several milliseconds, while the tip is being withdrawn. This results in the break of the nanobridge in some point, nearly in the middle. Finally after relaxation some part of the nanobridge atoms is deposited on the surface, whereas the rest spreading on the tip forms a new apex. Schematic representation of whole process is given in the Fig 6.5.

Depending on the applied voltage the nanobridge can leave different traces on the surface, which was successfully demonstrated in our experiments (ch. 5.4).

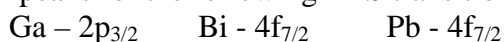
Another model for the understanding of the Bi (0001) surface nanostructuring, which combines two approaches described above, was proposed in [90]. The mechanism closely resembles a jump-to-contact description, which is typical for the material transfer from tip to substrate in the electrochemical environment [97]. At positive electric pulses Bi is field evaporated from the substrate with a barrier of evaporation of approx. 2.2 eV and is deposited on the tungsten tip. Here the field induced evaporation is followed by the formation of a nanobridge between tip and surface. Since Bi completely wets W, the tip apex will be covered homogeneously by a Bi film. Depending on the behaviour and stability of this film a jump-to-contact can occur. The model assumes that the processes of Bi evaporation and condensation are much faster in comparison to the reaction time of the microscope.

In order to reverse the direction of the Bi transport one can switch the polarity of the applied pulse. The difference of this mechanism in comparison to that in electrochemical environment is the source of Bi: in latter case it is accumulated on the tip apex from the electrolyte by reduction, whereas in our case it is evaporated from the Bi surface leaving defects such as pits and grooves.

Appendix A

XPS peak intensities measured on the pure components (Ga, Bi, Pb) and alloys (Ga-Bi, Ga-Pb)

Area of peaks for the following XPS transitions is provided in the tables below:



Film thickness is calculated, according to the eq. (5.1) for Ga-Bi and eq. (5.3) for Ga-Pb e.g. the film is considered as a slab consisting of pure surface active component (Bi or Pb). Numbers in brackets give the effective thickness of the SF films with defects (islands).

Acronyms frequently used as notes:

WF – wetting film

SFF – surface freezing film

SFF+I – surface freezing film with defects (islands)

Pure components: Ga, Bi, Pb

Metal	T (°C)	I ⁰ (eV*kcts/s)	Notes
Ga	20	4106	solid crucible 1
	70	4055	liquid, crucible 1
	170	4124	liquid, crucible 1
	25	2020*	crucible 2
	100	1613**	liquid, crucible 1
Bi	325	1174	liquid, crucible 1
	25	1094	solid, crucible 1
Pb	25	630**	solid, crucible1
	25	590	solid, crucible2
	25	585*	solid, crucible2

* - estimated from the measurements on the wetting film, see Ch. 5.1.1

** - reference for Ga-Pb $x(\text{Pb}) = 0.06\%$

Ga-Bi $x(\text{Bi}) = 0.31\%$, crucible 1, measurement 1 28.07.2003

T (°C)	I(Ga) (eV*kcts/s)	I(Bi) (eV*kcts/s)	Film thickness (Å)	Notes
130	3321	99.1	2.20	WF
100	3242	103.3	2.33	WF
70	3247	113.9	2.52	WF
50	275.6	1073	28.9	SFF

Ga-Bi $x(\text{Bi}) = 0.31\%$, crucible 1, measurement 2 04.08.2003

T (°C)	I(Ga) (eV*kcts/s)	I(Bi) (eV*kcts/s)	Film thickness (Å)	Notes
120	3137	115.5	2.62	WF
60	3122	131.6	2.93	WF
58	3084	130.0	2.94	WF
56	2961	127.9	2.99	WF
54	615.1	942	21.5	SFF
52	652.7	953	21.2	SFF

Ga-Bi $x(\text{Bi}) = 0.31\%$, crucible 1, measurement 3 06.08.2003

T (°C)	I(Ga) (eV*kcts/s)	I(Bi) (eV*kcts/s)	Film thickness (Å)	Notes
140	3085	150.8	3.29	WF
70	3073	153.9	3.36	WF
54	2923	186.8	4.04	WF
45	154.1	1095	33.8	SFF

Ga-Bi $x(\text{Bi}) = 0.31\%$, crucible 1, measurement 3 07.08.2003

T (°C)	I(Ga) (eV*kcts/s)	I(Bi) (eV*kcts/s)	Film thickness (Å)	Notes
140	3108	162.3	3.47	WF
45	257.8	1090	29.5	SFF
0	485.2	1172	25.0	SFF

Ga-Bi $x(\text{Bi}) = 0.31\%$, crucible 1, measurement 4 08.08.2003

T (°C)	Sputtering time (h)	I(Ga) (eV*kcts/s)	I(Bi) (eV*kcts/s)	Film thickness (Å)	Ga content	Notes
20	0	268.9	1172	29.8		SFF
20	0.03	580.4	1019		0.14	SFF
20	0.06	576.2	999.0		0.14	SFF
20	0.1	532.5	992.8		0.13	SFF
20	0.6	609.1	981.6		0.15	SFF
20	1.6	550.6	985.6		0.14	SFF
20	3.6	590.1	952.4		0.15	SFF
20	4.6	640.1	926.8		0.16	SFF

Ga-Bi $x(\text{Bi}) = 1.12\%$, crucible 1, measurement 1 02.09.2003

T (°C)	I(Ga) (eV*kcts/s)	I(Bi) (eV*kcts/s)	Film thickness (Å)	Notes
180	2956	165.9	3.66	WF
140	3152	168.3	3.53	WF
133	3147	171.2	3.58	WF
125	3112	173.5	3.65	WF
115	3060	187.3	3.91	WF
112	360.6	1053	26.5	SFF
55	215.9	1106	31.1	SFF

Ga-Bi $x(\text{Bi}) = 1.12\%$, crucible 1, measurement 2 29.10.2003

T (°C)	I(Ga) (eV*kcts/s)	I(Bi) (eV*kcts/s)	Film thickness (Å)	Notes
209	3326	149.4	3.08	WF
132	3219	169.8	3.49	WF
100	3175	179.2	3.68	WF
96	1372	609.3	13.0	SFF
96	1192	757.6	15.3	SFF

Ga-Bi $x(\text{Bi}) = 1.12\%$, crucible 1, measurement 3 18.08.2003

T (°C)	I(Ga) (eV*kcts/s)	I(Bi) (eV*kcts/s)	Film thickness (Å)	Notes
180	3128	162.2	3.45	WF
170	3124	181.3	3.76	WF
120	2948	197.5	4.19	WF
90	715.0	1024	21.0	SFF
25	642.8	1057	22.1	SFF

Ga-Bi $x(\text{Bi}) = 1.15\%$, crucible 2, measurement 4 10.12.2003

T (°C)	Time (h)	I(Ga) (eV*kcts/s)	I(Bi) (eV*kcts/s)	Film thickness (Å)	Notes
178		2665	167.0	3.98	WF
131.8		2627	180.7	4.27	WF
128	0	32.1	1049	47.2	SFF
127.8	0.5	71.5	1038	40.0	SFF
130.2	10	215.9	940.2	29.8	SFF
130.2	16	314.0	1183	28.6	SFF

Ga-Bi $x(\text{Bi}) = 4.72\%$, crucible 1, measurement 1 23.09.2003

T (°C)	I(Ga) (eV*kcts/s)	I(Bi) (eV*kcts/s)	Film thickness (Å)	Notes
280	2848	229.6	4.79	WF
200	2742	266.9	5.46	WF
174	2880	236.8	4.85	WF
90	135.8	1195	35.7	SFF

Ga-Bi $x(\text{Bi}) = 4.72\%$, crucible 1, measurement 2 06.11.2003

T (°C)	I(Ga) (eV*kcts/s)	I(Bi) (eV*kcts/s)	Film thickness (Å)	Notes
230	2566	245.9	5.40	WF
194	2570	257.4	5.57	WF
161	99.0	1024	37.0	SFF

Ga-Bi $x(\text{Bi}) = 4.72\%$, crucible 1, measurement 3 06.11.2003

T (°C)	I(Ga) (eV*kcts/s)	I(Bi) (eV*kcts/s)	Film thickness (Å)	Notes
270	2710	213.0	4.70	WF
175	2611	256.5	5.49	WF
166	82.7	1034	38.7	SFF

Ga-Bi $x(\text{Bi}) = 4.72\%$, crucible 1, measurement 4 13.11.2003

T (°C)	I(Bi) (eV*kcts/s)	Film thickness (Å) calculated from Bi signal only (eq. 6.3)	Notes
280.0	229.6	5.54	WF
270.0	212.9	5.09	WF
230.0	245.9	5.99	WF
200.0	266.9	6.58	WF
194.0	257.4	6.31	WF
183.0	251.6	6.15	WF
175.0	262.5	6.45	WF
170.0	262.0	6.44	WF, very slow cooling
169.0	261.0	6.41	WF
168.0	287.3	7.16	
167.0	292.9	7.33	
166.7	328.1	8.39	
166.3	340.2	8.76	
166.0	364.0	9.51	
165.7	360.0	9.39	
165.4	376.4	9.92	
165.0	385.0	10.20	
164.5	360.3	9.40	
163.5	368.4	9.66	no visible changes on the surface

Ga-Pb $x(\text{Pb}) = 0.06\%$, crucible 1, measurement 1 28.11.2005

T (°C)	I(Ga) (eV*kcts/s)	I(Pb) (eV*kcts/s)	Film thickness (Å)	Notes
170	1267	74.5	3.31	WF
120	1183	70.0	3.33	WF
80	1113	79.5	3.87	WF
60	1094	86.9	4.20	WF

Ga-Pb $x(\text{Pb}) = 0.06\%$, crucible 1, measurement 2 31.03.2004

T (°C)	I(Ga) (eV*kcts/s)	I(Pb) (eV*kcts/s)	Film thickness (Å)	Notes
128	1179	73.7	3.48	WF
50	719.5	259.9	11.4	SFF
40	485.4	315.4	15.3	SFF

Ga-Pb $x(\text{Pb}) = 0.06\%$, crucible 1, measurement 3 01.04.2004

T (°C)	I(Ga) (eV*kcts/s)	I(Pb) (eV*kcts/s)	Film thickness (Å)	Notes
62.5	1080	81.3	4.03	WF
53.3	636.4	203.4	10.61	SFF
58.0	1126	90.8	4.25	WF
53.1	870.7	157.4	7.52	SFF
52.8	679.2	175.7	9.39	SFF

Ga-Pb $x(\text{Pb}) = 0.27\%$, crucible 2, measurement 1 23.04.2004

T (°C)	Time (h)	I(Ga) (eV*kcts/s)	I(Pb) (eV*kcts/s)	Film thickness (Å)	Notes
141.0		1169	90.5	5.12	WF
136.1	0	982	125.1	7.23	?
134.2	24	826	321.6	(13.7)	SFF+I
135.0	48	951	241.8	(11.0)	SFF+I

Ga-Pb $x(\text{Pb}) = 0.27\%$, crucible 2, measurement 2 30.04.2004

T (°C)	Time (h)	I(Ga) (eV*kcts/s)	I(Pb) (eV*kcts/s)	Film thickness (Å)	Notes
139.0		1323	98.3	4.97	WF
136.9	0	151.1	553.4	32.4	SFF
137.3	17	799.6	319.6	(13.9)	SFF+I
137.3	19	878.2	298.4	(12.8)	SFF+I
137.4	22	919.2	274.2	(11.9)	SFF+I
137.4	39	1039	233.3	(10.2)	SFF+I

Ga-Pb $x(\text{Pb}) = 0.27\%$, crucible 2, measurement 3 05.05 - 10.05.2004

T (°C)	Time (h)	I(Ga) (eV*kcts/s)	I(Pb) (eV*kcts/s)	Film thickness (Å)	Notes
177.2		1415	97.7	4.71	WF
139.3		1379	104.6	5.05	WF
136.3	0	316.1	494.9	24.7	SFF cooling 0.5 K/h
136.4	0.5	336.0	490.1	24.0	SFF
136.5	1.5	369.0	479.3	(23.1)	SFF+I
137.4	3	411.6	465.9	(21.9)	SFF+I
137.5	15	575.0	397.0	(17.9)	SFF+I
134.2	20	546.6	407.7	(18.5)	SFF+I
132.4	23.5	521.5	417.0	(19.1)	SFF+I
131.0	26.5	510.6	424.6	(19.4)	SFF+I
124.6	39.5	445.3	434.3	(20.7)	SFF+I
122.3	44	436.2	438.0	(20.9)	SFF+I
120.6	48	455.4	441.7	(20.6)	SFF+I
106.0	120	406.5	443.8	(21.6)	SFF+I
34	135	296.6	497.6	(25.3)	SFF+I

Ga-Pb $x(\text{Pb}) = 0.27\%$, crucible 2, measurement 4 25.05.2004

T (°C)	Time (h)	I(Ga) (eV*kcts/s)	I(Pb) (eV*kcts/s)	Film thickness (Å)	Notes
138.3		1353	98.8	4.91	WF
136.6	0	235.7	548.0	28.2	SFF
136.6	2.3	369.9	503.9	(23.5)	SFF+I

Ga-Pb $x(\text{Pb}) = 0.41\%$, crucible 2, measurement 1 17.09.2004

T (°C)	Time (h)	I(Ga) (eV*kcts/s)	I(Pb) (eV*kcts/s)	Film thickness (Å)	Notes
180		1347	100.2	4.97	WF
162.3	0	395.4	475.7	22.4	SFF
184.5	1	1359	100.3	4.94	WF
162.2	0	313.3	527.6	25.3	SFF
162.0	2.75	448.2	464.8	(21.2)	SFF+I
161.9	4	509.7	438.5	(19.6)	SFF+I

Ga-Pb $x(\text{Pb}) = 0.41\%$, crucible 2, measurement 2 22.09.2004

T (°C)	I(Ga) (eV*kcts/s)	I(Pb) (eV*kcts/s)	Film thickness (Å)	Notes
164.6	1301	77.9	4.23	WF
160.2	378.8	490.1	23.0	SFF
136.9	151.1	553.4	32.4	SFF

Ga-Pb $x(\text{Pb}) = 0.41\%$, crucible 2, measurement 3 03.11.2004

T (°C)	Time (h)	I(Ga) (eV*kcts/s)	I(Pb) (eV*kcts/s)	Film thickness (Å)	Notes
167.9		1397	84.5	4.26	WF
166.5	0	397.5	465.8	22.2	SFF
165.9	0.5	387.0	466.1	22.4	SFF
165.4	1	366.2	471.9	23.0	SFF
162.8	3.5	355.4	476.8	23.3	SFF
161.7	4.5	347.1	483.7	23.7	SFF
160.0	6	335.0	500.3	24.2	SFF
155.0	22	314.8	495.6	24.7	SFF
40	25	245.4	516.8	27.3	SFF

Ga-Pb $x(\text{Pb}) = 0.52\%$, crucible 2, measurement 1 22.09.2004

T (°C)	Time (h)	I(Ga) (eV*kcts/s)	I(Pb) (eV*kcts/s)	Film thickness (Å)	Notes
172.7	0	432.3	451.6	21.2	SFF
171.1	1	413.6	462.3	21.8	SFF
165.4	2.5	380.6	485.9	22.9	SFF
160.2	5.5	416.2	470.2	(21.9)	SFF+I

Ga-Pb $x(\text{Pb}) = 0.52\%$, crucible 2, measurement 2 20.10.2004

T (°C)	Time (h)	I(Ga) (eV*kcts/s)	I(Pb) (eV*kcts/s)	Film thickness (Å)	Notes
237.1		1320	89.1	4.63	WF
236.8		1334	89.9	4.62	WF
180.8		1294	102.5	5.21	WF
179.9		1296	103.3	5.23	WF
179.3		1295	103.7	5.25	WF
178.3	0	434.1	464.6	21.4	SFF, T is kept constant
176.7	2	427.0	466.0	21.6	SFF
176.7	18	608.0	390.7	(17.4)	SFF+I

Ga-Pb $x(\text{Pb}) = 0.52\%$, crucible 2, measurement 3 19.11.2004

T (°C)	Time (h)	I(Ga) (eV*kcts/s)	I(Pb) (eV*kcts/s)	Film thickness (Å)	Notes
178.7		1304	103.4	5.21	WF
176.1		1331	94.6	4.81	WF
172.8	0	524.3	415.5	19.0	SFF
170.7	0.5	525.5	425.7	19.2	SFF
23	1.5	338.9	496.0	24.1	SFF
5	2.6	339.1	533.0	24.7	SFF, frozen bulk

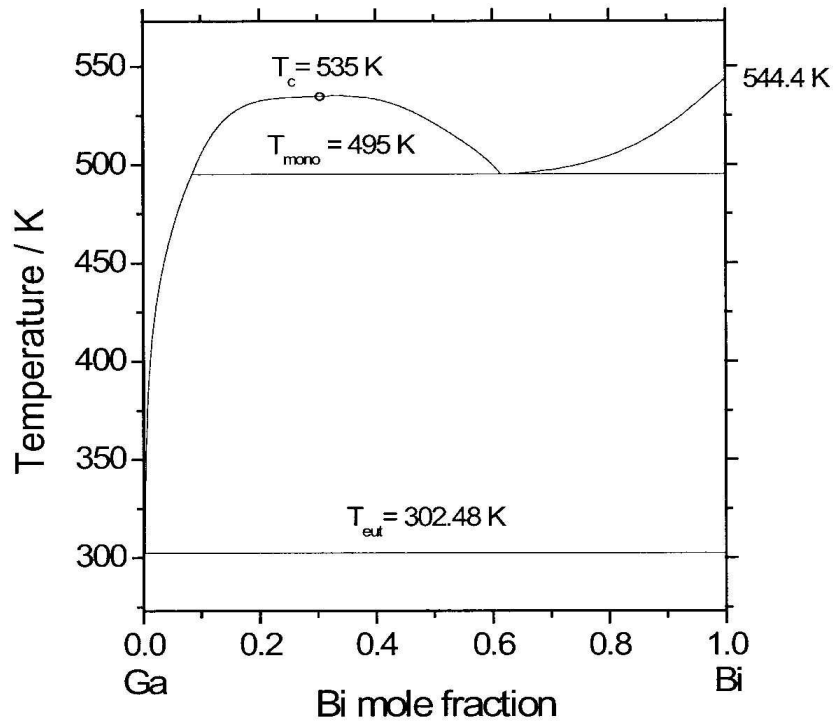
Ga-Pb $x(\text{Pb}) = 0.52\%$, crucible 2, measurement 4 22.09.2004

T (°C)	Sputtering time (h)	I(Ga) (eV*kcts/s)	I(Pb) (eV*kcts/s)	Film thickness (Å)	Notes
20	0	295.7	527.3	25.8	SFF
20	0.2	285.6	531.7	26.2	SFF
20	0.4	333.1	518.0	24.6	SFF
20	0.6	297.1	541.4	26.0	SFF

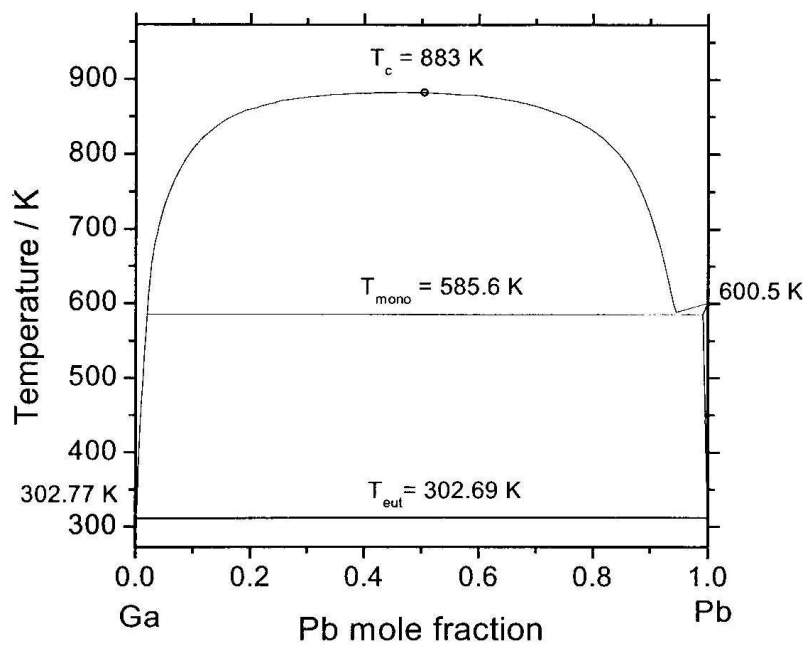
Appendix B

Phase diagrams of the Ga-Bi and Ga-Pb systems.

1. Ga-Bi (B. Predel, Z. Phys. Chem. NF 24 (1960) 206)



2. Ga-Pb (B. Predel, Z. Metallk., 50 (1959) 663)



Manufacturer list

Alfa Chemicals	A. Johnson Matthey Company Postfach 110765 D-76057, Karlsruhe, Germany
Goodfellow	Goodfellow GmbH Postfach 1343 D-61213, Bad Nauheim, Germany
Omicron	Omicron Nanotechnology GmbH Limbergerstr. 75 D-65232, Taunusstein, Germany
Berliner Glass	Berliner Glass KG Waldkraiburgerstr. 5 D-12347, Berlin, Germany
Eurotherm	Eurotherm GmbH Postfach 1453 D-65534, Limburg an der Lahn, Germany

References

- [1] Xu, B.; Liang, X.; Dong, M. S.; Ma, S. **Progress of nano -surface engineering**. International Journal of Materials & Product Technology (2003), 18(4/5/6), 338-343.
- [2] Dresselhaus, M. S. **Perspectives on nanosciences and nanotechnology**. Surfaces and Interfaces in Nanostructured Materials and Trends in LIGA, Miniaturization, and Nanoscale Materials, MPMD Global Innovations Proceedings held at the TMS Annual Meeting, 5th, Charlotte, NC, United States, Mar. 14-18, 2004 (2004), 385-92.
- [3] Dash, J. G. **History of the search for continuous melting**. Reviews of Modern Physics (1999), 71(5), 1737-43.
- [4] Wettlaufer, J. S. **Impurity Effects in the Premelting of Ice**. Physical Review Letters (1999), 82(12), 2516-9.
- [5] Regan, M. J.; Pershan, P. S.; Magnussen, O. M.; Ocko, B. M.; Deutsch, M.; Berman, L. E. **Capillary-wave roughening of surface-induced layering in liquid gallium**. Physical Review B: Condensed Matter (1996), 54(14), 9730-3.
- [6] Celestini, F.; Ercolessi, F.; Tosatti, E. **Role of orientational order at surface-initiated recrystallization of a liquid metal**. Surface Science (1997), 377-379 914-7.
- [7] Regan, M. J.; Tostmann, H.; Pershan, P. S.; Magnussen, O. M.; DiMasi, E.; Ocko, B. M.; Deutsch, M. **X-ray study of the oxidation of liquid-gallium surfaces**. Physical Review B: Condensed Matter (1997), 55(16), 10786-90.
- [8] Kroes, G. J. **Surface melting of the (0001) face of TIP4P ice**. Surface Science (1992), 275(3), 365-82.
- [9] Dosch, H.; Lied, A.; Bilgram, J. H. **Glancing-angle X-ray scattering studies of the premelting of ice surfaces**. Surface Science (1995), 327(1/2), 145-64.
- [10] Dosch, H.; Lied, A.; Bilgram, J. H. **Disruption of the hydrogen-bonding network at the surface of Ih ice near surface premelting**. Surface Science (1996), 366(1), 43-50.
- [11] Doepenschmidt, A.; Butt, H.-J. **Measuring the Thickness of the Liquid-like Layer on Ice Surfaces with Atomic Force Microscopy**. Langmuir (2000), 16(16), 6709-14.
- [12] Wei, X.; Miranda, P. B.; Zhang, C.; Shen, Y. R. **Sum-frequency spectroscopic studies of ice interfaces**. Physical Review B: Condensed Matter and Materials Physics (2002), 66(8), 085401/1-13.
- [13] Lang, P. **Surface induced ordering effects in soft condensed matter systems**. Journal of Physics: Condensed Matter (2004), 16(23), R699-R720.
- [14] Tkachenko, A. V.; Rabin, Y. **Theory of surface freezing of alkanes**. Physical Review E: (1997), 55(1-B), 778-84.
- [15] Dash J. G. in: Taub H.; Torzo G.; Lauter H. J.; Fain S. C., Jr. **Frost heave and the surface melting of ice**. NATO ASI Series, Series B: Physics (1991), 267(Phase Transitions Surf. Films 2), 339-56.
- [16] Rhykerd, C. L., Jr.; Schoen, M.; Diestler, D. J.; Cushman, J. H. **Epitaxy in simple classical fluids in micropores and near-solid surfaces**. Nature (London, United Kingdom) (1987), 330(6147), 461-3.

- [17] Van der Veen, J. F. **Melting and freezing at surfaces**. *Surface Science* (1999), 433-435 1-11.
- [18] Wu, X. Z.; Ocko, B. M.; Sirota, E. B.; Sinha, S. K.; Deutsch, M.; Cao, B. H.; Kim, M. W. **Surface tension measurements of surface freezing in liquid normal alkanes**. *Science* (Washington, DC, United States) (1993), 261(5124), 1018-21.
- [19] Wu, X. Z.; Sirota, E. B.; Sinha, S. K.; Ocko, B. M.; Deutsch, M. **Surface crystallization of liquid normal-alkanes**. *Physical Review Letters* (1993), 70(7), 958-61.
- [20] Hughes, C. J.; Earnshaw, J. C. **Light-scattering study of a surface-induced phase transition in alkane fluids**. *Physical Review E*: (1993), 47(5), 3485-96.
- [21] Earnshaw, J. C.; Hughes, C. J. **Surface-induced phase transition in normal alkane fluids**. *Physical Review A: Atomic, Molecular, and Optical Physics* (1992), 46(8), R4494-6.
- [22] Chao, C. Y.; Hui, S. W.; Maclennan, J. E.; Ho, J. T. **Surface-freezing transitions and novel tilted hexatic phases in smectic liquid-crystal films**. *Physical Review Letters* (1997), 78(13), 2581-4.
- [23] Chao, C. Y.; Hui, S. W.; Maclennan, J. E.; Pang, J. Z.; Ho, J. T. **Surface-freezing transitions and novel tilted hexatic phases in smectic liquid-crystal thin films**. *Molecular Crystals and Liquid Crystals Science and Technology, Section A: Molecular Crystals and Liquid Crystals* (1999), 330 1495-502.
- [24] Swanson, Brian D.; Sorensen, Larry B. **What forces bind liquid crystals?** *Physical Review Letters* (1995), 75(18), 3293-6.
- [25] Ocko, B. M. **Smectic-layer growth at solid interfaces**. *Physical Review Letters* (1990), 64(18), 2160-3.
- [26] Deutsch, M.; Wu, X. Z.; Sirota, E. B.; Sinha, S. K.; Ocko, B. M.; Magnussen, O. M. **Crystalline bilayers on the surface of molten alcohol**. *Europhysics Letters* (1995), 30(5), 283-8.
- [27] Gang, O.; Wu, X. Z.; Ocko, B. M.; Sirota, E. B.; Deutsch, M. **Surface freezing in chain molecules. II. Neat and hydrated alcohols**. *Physical Review E*: (1998), 58(5-B), 6086-100.
- [28] Gang, O.; Ocko, B. M.; Wu, X. Z.; Sirota, E. B.; Deutsch, M. **Surface freezing in hydrated alcohol melts**. *Physical Review Letters* (1998), 80(6), 1264-7.
- [29] Gang, O.; Ocko, B. M.; Wu, X. Z.; Sirota, E. B.; Deutsch, M. **Structural control of the surface-frozen layer in alcohol melts**. *Journal of Physics: Condensed Matter* (2000), 12(8A), A357-62.
- [30] Gang, O.; Ocko, B. M.; Wu, X. Z.; Sirota, E. B.; Deutsch, M. **Surface structure tuning in alcohol melts by bulk additives**. *Colloids and Surfaces A* (2000), 164(1), 55-61.
- [31] Gang, O.; Ocko, B. M.; Wu, X. Z.; Sirota, E. B.; Deutsch, M. **Tunable surface phases in alcohol-diol melts**. *Physical Review Letters* (1999), 82(3), 588-91.
- [32] Gang, O.; Ellmann, J.; Moller, M.; Kraack, H.; Sirota, E. B.; Ocko, B. M.; Deutsch, M. **Surface phases of semi-fluorinated alkane melts**. *Europhysics Letters* (2000), 49(6), 761-7.
- [33] Wu, X. Z.; Ocko, B. M.; Tang, H.; Sirota, E. B.; Sinha, S. K.; Deutsch, M. **Surface freezing in binary mixtures of alkanes: new phases and phase transitions**. *Physical Review Letters* (1995), 75(7), 1332-5.

- [34] Turchanin, A.; Freyland, W.; Nattland, D. **Surface freezing in liquid Ga -Bi alloys: optical second harmonic and plasma generation study.** *Physical Chemistry Chemical Physics* (2002), 4(4), 647-54.
- [35] Yang, B.; Gidalevitz, D.; Li, D.; Huang, Z.; Rice, S. A. **Two-dimensional freezing in the liquid-vapor interface of a dilute Pb:Ga alloy.** *Proceedings of the National Academy of Sciences of the United States of America* (1999), 96(23), 13009-11.
- [36] Bartel, K.; Nattland, D.; Kumar, A.; Dogel, S.; Freyland, W. **Ellipsometric characterization of surface freezing in Ga-based alloys.** *Journal of Physics: Condensed Matter* (2006), 18(15), 3535-42.
- [37] Nattland, D.; Turchanin, A.; Freyland, W. **Surface freezing transitions in liquid binary alloys.** *Journal of Non-Crystalline Solids* (2002), 312-314 464-71.
- [38] Turchanin, A.; Freyland, W. **Surface freezing and wetting in Ga -Pb alloy: Second harmonic and plasma generation study.** *Physical Chemistry Chemical Physics* (2003), 5(23), 5285-90.
- [39] Ayyad, A. H.; Mechdiev, I.; Freyland, W. **Light scattering study of surface freezing and surface viscoelasticity in a eutectic liquid Ga - Bi alloy.** *Chemical Physics Letters* (2002), 359(3,4), 326-30.
- [40] Ayyad, A. H.; Freyland, W. **Wetting transition in liquid Ga - Bi alloys. Light scattering study of surface energy and entropy.** *Surface Science* (2002), 506(1-2), 1-11.
- [41] Dogel, S.; Nattland, D.; Freyland, W. **Complete wetting transitions at the liquid-vapor interface of gallium-bismuth alloys: Single-wavelength and spectroscopic ellipsometry studies.** *Physical Review B: Condensed Matter and Materials Physics* (2005), 72(8), 085403/1-12.
- [42] Shpyrko, O.G.; Streitel, R.; Balagurusamy, V.S.K.; Pershan, P.S. et. al (2006) in preparation.
- [43] Freyland, W. **Metal-molten salt interfaces. Wetting transitions and electrocrystallization.** *NATO Science Series, II: Mathematics, Physics and Chemistry* (2002), 52(Molten Salts: From Fundamentals to Applications), 149-77.
- [44] Dietrich, S. **Wetting phenomena.** *Phase Transitions Crit. Phenom.* (1988), 12 1-218.
- [45] Charvolin, J.; Joanny, J. F.; Zinn-Justin, J. (eds), *Liquids at Interfaces*, North-Holland, Amsterdam, (1990).
- [46] Croxton, C. A. (ed.), *Fluid Interfacial Phenomena*, John Wiley and Sons, New York, (1986).
- [47] Israelachvili, J. N. *Intermolecular and Surface Forces*, 5th ed., Academic Press, London, (1995).
- [48] Widom, B. **Structure of the $\alpha\gamma$ interface.** *Journal of Chemical Physics* (1978), 68(8), 3878-83.
- [49] Maeda, N.; Yaminsky, V. V. **Experimental observations of surface freezing.** *International Journal of Modern Physics B* (2001), 15(23), 3055-77.
- [50] Loewen, H. **Melting, freezing and colloidal suspensions.** *Physics Reports* (1994), 237(5), 249-324.
- [51] Pluis, B.; Denier van der Gon, A. W.; van der Veen, J. F.; Riemersma, A. J. **Surface-induced melting and freezing. I. Medium-energy ion scattering investigation of the melting of lead{hkl} crystal faces.** *Surface Science* (1990), 239(3), 265-81.

- [52] D'Evelyn, M. P.; Rice, S. A. **Structure in the density profile at the liquid-metal-vapor interface.** *Physical Review Letters* (1981), 47(25), 1844-7.
- [53] Zhao, M.; Chekmarev, D. S.; Cai, Z.-H.; Rice, S. A. **Structure of liquid Ga and the liquid-vapor interface of Ga.** *Physical Review E: Statistical Physics, Plasmas, Fluids, and Related Interdisciplinary Topics* (1997), 56(6), 7033-42.
- [54] Regan, M. J.; Kawamoto, E. H.; Lee, S.; Pershan, P. S.; Maskil, N.; Deutsch, M.; Magnussen, O. M.; Ocko, B. M.; Berman, L. E. **Surface layering in liquid gallium: an X-ray reflectivity study.** *Physical Review Letters* (1995), 75(13), 2498-501.
- [55] Magnussen, O. M.; Ocko, B. M.; Regan, M. J.; Penanen, K.; Pershan, P. S.; Deutsch, M. **X-ray reflectivity measurements of surface layering in liquid mercury.** *Physical Review Letters* (1995), 74(22), 4444-7.
- [56] Grubel, G.; Als-Nielsen, J.; Freund, A. K. **The TROIKA beamline at ESRE.** *Journal de Physique IV: Proceedings* (1994), 4(C9 Proceedings of the European Symposium on Frontiers in Science and Technology with Synchrotron Radiation, 1994), C9/27-34.
- [57] Elbaum, M.; Lipson, S. G.; Dash, J. G. **Optical study of surface melting on ice.** *Journal of Crystal Growth* (1993), 129(3-4), 491-505.
- [58] Maeda, N.; Yaminsky, V. V. **Surface supercooling and stability of n-alkane films.** *Physical Review Letters* (2000), 84(4), 698-700.
- [59] Merkl, C.; Pfohl, T.; Riegler, H. **Influence of the molecular ordering on the wetting of SiO₂/air interfaces by alkanes.** *Physical Review Letters* (1997), 79(23), 4625-8.
- [60] Sirota, E. B.; Wu, X. Z.; Ocko, B. M.; Deutsch, M. **What drives the surface freezing in alkanes?** *Physical Review Letters* (1997), 79(3), 531-.
- [61] Freyland, W.; Ayyad, A. H.; Mechdiev, I. **Wetting, prewetting and surface freezing transitions in fluid Ga-based alloys: A surface light scattering study.** *Journal of Physics: Condensed Matter* (2003), 15(1), S151-7.
- [62] Briggs, D.; Seah, M. P. (eds.) **Practical surface analysis (second edition). Vol. 1: Auger and X-ray Photoelectron Spectroscopy**, Chapters 3-5, John Wiley & Sons Ltd. (1990).
- [63] J.F.Watts, J.Wolstenholme **An Introduction to Surface Analysis by XPS and AES**, John Wiley & Sons Ltd, (2003).
- [64] Grassenbauer, M.; Dudek, H.; Ebel, M. F. **Angewante Oberflächenanalyse**, Springer, (1985).
- [65] O'Connor, D.J.; Sexton, B.A.; Smart R.St.C. (eds.) **Surface Analysis Methods in Material Science**, 2nd Edition, Springer, Berlin, (2003).
- [66] Binnig, G.; Rohrer, H. **Scanning tunneling microscopy.** *Helvetica Physica Acta* (1982), 55(6), 726-35.
- [67] Bardeen, J. **Tunneling from a many-particle point of view.** *Physical Review Letters* (1961), 6 57-9.
- [68] Tersoff, J.; Hamann, D. R. **Theory and application for the scanning tunneling microscope.** *Physical Review Letters* (1983), 50(25), 1998-2001.

- [69] Wiesendanger, R.; Guentherodt, H. J.; Editors. **Scanning Tunneling Microscopy III. Theory of STM and Related Scanning Probe Methods**. [In: Springer Surf. Sci., 1993; 29]. (1993)
- [70] Drakova, D. **Theoretical modeling of scanning tunneling microscopy, scanning tunneling spectroscopy, and atomic force microscopy**. Reports on Progress in Physics (2001), 64(2), 205-90.
- [71] Bonnel D., **Scanning Probe Microscopy and spectroscopy**. 2nd Edition, Wiley-VCH, New York, 2001.
- [72] Indlekofer, G.; Oelhafen, P.; Guentherodt, H. J. **New preparation method for liquid alloy surfaces and their characterization by electron spectroscopy**. Materials Research Society Symposium Proceedings (1987), 83(Phys. Chem. Prop. Thin Met. Overlayers Alloy Surf.), 75-82.
- [73] Tanuma, S.; Powell, C. J.; Penn, D. R. **Calculations of electron inelastic mean free paths. II. Data for 27 elements over the 50-2000 eV range**. Surface and Interface Analysis (1991), 17(13), 911-26.
- [74] Landa, A.; Wynblatt, P. **Roughening of the Pb (110) surface: combined Monte Carlo and molecular-dynamics study**. Computational Materials Science (1997), 7(3), 257-70.
- [75] Penfold J. **The structure of the surface in pure liquids**. Rep. Prog. Phys 64 (2001) 777-814.
- [76] Bartelt M. C.; Evans J. W.; **Temperature dependence of kinetic roughening during metal (100) homoepitaxy: transition between mounding and smooth growth**. Surface Science 423 (1999) 189-207.
- [77] Fang, K.; Yang, H.-N.; Wang, G.-C. **Modification of surface structures and roughening phase transition in lead(110) by impurities**. Surface Science (1993), 284(1-2), L399-404.
- [78] Kinnersley, W. **Exact large amplitude capillary waves on sheets of liquid**. Journal of Fluid Mechanics (1976), 77, 229-41.
- [79] Issanin, A.; Turchanin, A.; Freyland, W. **Electron spectroscopy and scanning tunneling microscopy study of quasi-two-dimensional freezing at the liquid/vapor interface of Ga-Bi alloys**. Journal of Chemical Physics (2004), 121(23), 12005-9
- [80] Schon, G. **Auger and direct electron spectra in X-ray photoelectron studies of zinc, zinc oxide, gallium, and gallium oxide**. Journal of Electron Spectroscopy and Related Phenomena (1973), 2(1), 75-86.
- [81] Scrocco, M. **X-ray and electron-energy-loss spectra of bismuth, antimony, tellurium and bismuth telluride (Bi₂Te₃) antimony telluride (Sb₂Te₃) chalcogenides**. Journal of Electron Spectroscopy and Related Phenomena (1990), 50(3), 171-84.
- [82] Kerber, S. J.; Barr, T. L.; Mann, G. P.; Brantley, W. A.; Papazoglou, E.; Mitchell, J. C. **The complementary nature of X-ray photoelectron spectroscopy and angle-resolved X-ray diffraction. Part II: analysis of oxides on dental alloys**. Journal of Materials Engineering and Performance (1998), 7(3), 334-42.
- [83] Tostmann, H.; DiMasi, E.; Pershan, P. S.; Ocko, B. M.; Shpyrko, O. G.; Deutsch, M. **Wetting phase transition at the surface of liquid Ga -Bi alloys. An X-ray reflectivity study**. Los Alamos National Laboratory, Preprint Archive, Condensed Matter (2004), 1-5
- [84] Issanin, A.; Turchanin, A.; Freyland, W. **Quasi-two-dimensional freezing and melting at the liquid/vapour interface of a Ga-Pb alloy**. Chemical Physics Letters (2004), 394(1-3), 220-24.

- [85] Oelhafen, P.; Indlekofer, G.; Guentherodt, H. J. **Valence electron structure of the heavy polyvalent liquid metals from mercury to bismuth**. Zeitschrift fuer Physikalische Chemie (Muenchen, Germany) (1988), 157(2), 483-8
- [86] Kuipers, L.; Frenken, J. W. M. **Jump to contact , neck formation, and surface melting in the scanning tunneling microscope**. Physical Review Letters (1993), 70(25), 3907-10.
- [87] Nagao, T.; Doi, T.; Sekiguchi, T.; Hasegawa, S. **Epitaxial growth of single-crystal ultrathin films of bismuth on Si(111)**. Japanese Journal of Applied Physics, Part 1: Regular Papers, Short Notes & Review Papers (2000), 39(7B), 4567-70.
- [88] Edelman, V. S.; Sharvin, D. Yu.; Khlyustikov, I. N.; Troyanovskii, A. M. **STM revealing of twin microlayers with quantized width on cleaved bismuth surface**. Europhysics Letters (1996), 34(2), 115-20.
- [89] Speller, S.; Heiland, W.; Biedermann, A.; Platzgummer, E.; Nagl, C.; Schmid, M.; Varga, P. **An STM study of the step structure of Pb (110) and Pb (111)**. Surface Science (1995), 331-3
- [90] Turchanin, A.; Freyland, W. **Nanostructuring of Bi(0001) surfaces with the scanning tunneling microscope. Writing of periodic Bi structures by bias voltage pulsing**. Applied Physics Letters (2005), 87(17), 173103/1-3.
- [91] Fuchs, H.; Schimmel, T.; Akari, S.; Eng, L. M.; Anders, M.; Lux-Steiner, M.; Dransfeld, K. **Layered semiconductors as materials for (sub)nanometer scale surface modification with the STM**. NATO ASI Series, Series E: Applied Sciences (1993), 235(Nanosources and Manipulation of Atoms under High Fields and Temperatures: Applications), 293-309.
- [92] Huang, D. H.; Aono, M. **STM atom manipulation with different material tips**. Journal of Surface Analysis (1998), 4(2), 264-7.
- [93] Li Y.Z.; Vazquez L.; Piner R.; Andres P.; Reifengerger R. **Writing nanometer-scale symbols in gold using the scanning tunneling microscope**. Appl. Phys. Lett. 54 (1989) 54 1424-6.
- [94] Kornilov, V. M.; Lachinov, A. N. **STM surface modification of the Si-SiO₂-polymer system**. Microelectronic Engineering (2003), 69(2-4), 399-404.
- [95] Tsekov R.; Freyland W. **Model calculations of surface phase transitions in Ga-Bi alloys: adsorption, wetting, surface freezing and melting**. Journal of Physics: Condensed Matter (2003), 15(36), 6155-65.
- [96] CRC book of chemistry and physics. Chemical Rubber Company. Lide D. R. 2003.
- [97] Kolb, D. M.; Ullmann, R.; Will, T. **Nanofabrication of small copper clusters on gold (111) electrodes by a scanning tunneling microscope**. Science (Washington, DC) (1997), 275(5303), 1097-9.
- [98] Garcia, N.; Ocal, C.; Flores, F. **Model theory for scanning tunneling microscopy: application to gold(110)(1 × 2)**. Physical Review Letters (1983), 50(25), 2002-5.
- [99] Gadzuk, J. W.; Plummer, E. W. **Field emission energy distribution (FEED)**. Reviews of Modern Physics (1973), 45(3), 487-548.
- [100] Huang D. H.; Nakayama T; Aono M. **Platinum nanodot formation by atomic point contact with scanning tunneling microscope platinum tip**. Applied Physics Letters 73, (1998), 3360-2.

Acknowledgements

I would like to express my appreciation to various people for the assistance in the completion of this thesis:

Prof. Dr. W. Freyland for his excellent guidance, providing me with a great opportunity for doing research and valuable discussions at all stages of this work.

Priv.-Doz. Dr. P. Weiss, the co-referee of this work.

Priv.-Doz. Dr. D. Nattland for very useful advises and talks, concerning fundamental scientific aspects as well as practical ones, which help to solve almost all daily problems, especially in the beginning of the work in Karlsruhe.

Dr. V. Halka for the assistance in operation with Omicron setup.

J. Dubielzig for good organisation of parties, barbeque and other holiday activities.

D. Walz and P. Buchenberger for competent and quick solution of the hardware problems.

H. Ernesti for availability of the mineral water, which was consumed in large amounts.

F. Imhoff and J. Szepessy for the help with computers and software.

All PhD students and technical staff of the “Condensed Matter” division for friendly atmosphere.

My wife Svitlana for the support and motivation all the time, when I was outside my office and lab.

Curriculum Vitae

PERSONAL DATA

Name: Alexander N. Issanin
Date of birth: 18.10.1977
Place of birth: St. Petersburg, Russian Federation
Nationality: Russian
Marital status: married, 1 child

EDUCATION AND WORK HISTORY

Aug 2002 – Present PhD student at the University of Karlsruhe in the group of Prof. W. Freyland (Department of Physical chemistry, Condensed Matter Division). Title of the dissertation: “*Wetting and Surface Freezing Transitions at the Liquid-Vapour Interface of Ga-based Alloys: STM, XPS and AES Study*”

Aug 1999 – Jul 2002 Research assistant at Ernst-Moritz-Arndt University of Greifswald. Work on project “*Molecular Dynamic Study of DNA interaction with cisplatin*”.

Sep 1994 – Jun 1999 St.Petersburg State University, Department of Chemistry. Graduated with Diploma in Chemistry. Diploma thesis with title: “*Study of Solvent Effects on the Conformations of (β 1,4)mannobiose with Molecular Dynamics*”
Training abroad: University of Kaiserslautern, Germany, 1998, 2 months and Kon-Kuk University, Seoul, South Korea 1998-1999, 6 months

Sep 1992 – Jun 1994 High school: Academic Gymnasium, Peterhof, St. Petersburg. Class with extended program in chemistry and biology

Sep 1984 – Jun 1992 Elementary and junior high school St. Petersburg